

## ABSTRACT

Title of Document:                   EXCITON   ENGINEERING   THROUGH  
  TUNABLE FLUORESCENT QUANTUM  
  DEFECTS

Hyejin Kwon, Doctor of Philosophy, 2016

Directed By:                         Professor YuHuang Wang  
  Department of Chemistry and Biochemistry

This thesis demonstrates exciton engineering in semiconducting single-walled carbon nanotubes through tunable fluorescent quantum defects. By introducing different functional moieties on the  $sp^2$  lattice of carbon nanotubes, the nanotube photoluminescence is systematically tuned over 68 meV in the second near-infrared window. This new class of quantum emitters is enabled by a new chemistry that allows covalent attachment of alkyl/aryl functional groups from their iodide precursors in aqueous solution. Using aminoaryl quantum defects, we show that the pH and temperature of complex fluids can be optically measured through defect photoluminescence that encodes the local environment information. Furthermore, defect-bound trions, which are electron-hole-electron tri-carrier quasi-particles, are observed in alkylated single-walled carbon nanotubes at room temperature with surprisingly high photoluminescence brightness. Collectively, the emission from defect-bound excitons and trions in (6,5)-single walled carbon nanotubes is 18-fold

brighter than that of the native exciton. These findings pave the way to chemical tailoring of the electronic and optical properties of carbon nanostructures with fluorescent quantum defects and may find applications in optoelectronics and bioimaging.

EXCITON ENGINEERING THROUGH TUNABLE FLUORESCENT  
QUANTUM DEFECTS

By

Hyejin Kwon

Dissertation submitted to the Faculty of the Graduate School of the  
University of Maryland, College Park, in partial fulfillment  
of the requirements for the degree of  
Doctor of Philosophy  
2016

Advisory Committee:

Professor YuHuang Wang, Committee Chair  
Professor Sang Bok Lee  
Professor Zhihong Nie  
Professor Janice Reutt-Robey  
Dean's Representative: Professor Min Ouyang

© Copyright by  
Hyejin Kwon  
2016

To my family

## Acknowledgements

I thank my advisor Prof. YuHuang Wang for his continuous encouragement and support throughout my graduate studies. He has helped me think beyond technical problems and led me to focus on our exciting research on fluorescent quantum defects. I would like to thank Prof. Janice Reutt-Robey, Prof. Sang Bok Lee, Prof. Zhihong Nie, and Prof. Min Ouyang for serving on my committee.

I thank Mijin Kim who has collaborated with me for the projects presented in this thesis. I thank Brendan Meany for providing high purity carbon nanotube samples that have facilitated many of the experiments, Dr. Yanmei Piao for discussions about optical properties of excitons, Allen Ng and Dr. Chienfu Chen for collaboration on the tube-in-a-tube project, and Lyndsey Powell for helpful suggestions and critical reviews on manuscripts and proposals. I would like to thank Prof. George C. Schatz and Dr. Al'ona Furmanchuk at the Northwestern University for their theoretical calculations of tunable fluorescent quantum defects. I thank Dr. Karen Gaskell and David Ramsdell for assistance with XPS measurements and Dr. Yiu-fai Lam for NMR. I also thank all the other Wang group members and alumni for their support and help.

This research was supported in part by the National Science Foundation (CHE-1507974, CAREER CHE-1055514), the Office of Naval Research (N000141110465), the National Institutes of Health (1R01GM114167), and the University of Maryland.

Lastly, I would like to thank my family including my husband, Taek Il Oh, lovely daughters, Yoona and Suah, and parents and parents-in-law Youngdon Kwon,

Eunsook Lee, Chaesoek Oh, and Youngsoon Kwak for their continued belief in me. I couldn't have done it without their supports.

# Table of Contents

Acknowledgements.....	iii
Table of Contents.....	v
List of Tables.....	vii
List of Figures.....	viii
List of Abbreviations.....	xvii
Chapter 1 . Introduction and Overview.....	1
1.1. Excitons in nanomaterials.....	1
1.1.1. Excitons: definitions and models.....	1
1.1.2. Quantum confinement effects in nanomaterials.....	6
1.2. Carbon nanotube excitons.....	9
1.2.1. Structures of carbon nanotubes.....	9
1.2.2. Optical properties of single walled carbon nanotubes.....	12
1.2.3. Carbon nanotube excitons.....	14
1.2.4. Defect induced photoluminescence.....	17
1.3. Charged excitons in semiconducting materials.....	20
1.3.1. Formation of charged excitons in nanomaterials.....	20
1.3.2. Optical properties of trions in semiconductors.....	21
1.3.3. Trions in carbon nanotubes.....	22
1.4. Preparation of high purity semiconducting carbon nanotubes.....	24
1.5. Overview of thesis work.....	25
Chapter 2 . Molecularly Tunable Fluorescent Quantum Defects.....	27
2.1. Introduction.....	27
2.2. Experimental and theoretical calculation methods.....	30
2.2.1. Aqueous dispersions of individual SWCNT crystals.....	30
2.2.2. Synthetic creation of fluorescent quantum defects in SWCNTs.....	31
2.2.3. <i>In situ</i> UV-Vis-NIR absorption and photoluminescence spectroscopy.....	31
2.2.4. Resonant Raman scattering and X-ray photoelectron spectroscopy.....	32
2.2.5. Theoretical calculation methods of fluorescent quantum defects.....	32
2.3. Results and discussion.....	33
2.3.1. Creation of alkylated fluorescent quantum defects.....	33
2.3.2. Tunable fluorescent quantum defects with alkylation.....	43
2.3.3. Inductive effects of alkyl defects.....	47
2.3.4. Creation of extended fluorescent quantum defects: aryl and divalent defects.....	50
2.3.5. Tunable fluorescent quantum defects through aryl and divalent groups..	52
2.3.6. DFT calculation of fluorescent quantum defects.....	58
2.4. Conclusions.....	67

Chapter 3 . Optical Probing of Local pH and Temperature in Complex Fluid through Semiconducting Carbon Nanotubes.....	68
3.1. Introduction.....	68
3.2. Experimental methods .....	71
3.2.1. Creation of $sp^3$ defect sites on SWCNTs with diazonium chemistry .....	71
3.2.2. pH-dependent defect photoluminescence .....	72
3.2.3. Temperature-dependent defect photoluminescence.....	72
3.2.4. Defect photoluminescence as a pH sensor in biological medium.....	73
3.3. Results and discussion .....	73
3.3.1. The results of pH-sensitive defect photoluminescence.....	73
3.3.2. Temperature-sensitive defect photoluminescence .....	82
3.3.3. Properties of defect photoluminescence toward biological applications..	84
3.4. Conclusions.....	88
Chapter 4 . Brightening of Carbon Nanotube Trion through Fluorescent Quantum Defects .....	89
4.1. Introduction.....	89
4.2. Experimental methods .....	91
4.2.1. Preparation of SWCNT solutions for trion photoluminescence .....	91
4.2.2. Optical probing of pH- and temperature-response in trion PL .....	92
4.2.3. Calculation of defect photoluminescence brightening.....	92
4.3. Results and discussion .....	93
4.3.1. Trion photoluminescence through alkyl defects .....	93
4.3.2. Temperature response of trion PL.....	103
4.3.3. pH-dependence of trion photoluminescence.....	104
4.4. Conclusions.....	105
Chapter 5. Summary and Outlook .....	107
5.1. Summary .....	107
5.2. Outlook .....	108
Bibliography .....	110

## List of Tables

<b>Table 2-1.</b> Control reactions with different reagent conditions. ....	36
<b>Table 2-2.</b> Spectral characteristics of alkyl fluorescent quantum defects in (6,5)-SWCNTs and calculated inductive constants of the covalently bonded alkyl groups.....	45
<b>Table 2-3.</b> PL spectral characteristics of (6,5)-SWCNTs covalently functionalized with different monovalent and divalent groups. ....	53
<b>Table 2-4.</b> Alkyl/aryl halides used in this study and their defect PL. ....	56
<b>Table 2-5.</b> Orbital energies of simulated structures. Note that all conformations of (6,5)-SWCNT-(CF <sub>3</sub> ) <sub>n</sub> (n = 1, 2) produce larger shifts in emission energy (E <sub>11</sub> - E <sub>11</sub> <sup>-</sup> ) compared to their respective -CH <sub>3</sub> defects. ....	63
<b>Table 3-1.</b> Defect photoluminescence of (6,5)-SWCNTs with various functional groups -ArX at different pH. The pH dependence is observed only in the aminobenzene functionalized (6,5)-SWCNTs. ....	79
<b>Table 3-2.</b> Chirality-dependent pH response of SWCNT-C <sub>6</sub> H <sub>4</sub> N(CH <sub>2</sub> CH <sub>3</sub> ) <sub>2</sub> . ....	81
<b>Table 4-1.</b> PL results of trions from chirality-enriched SWCNTs, functionalized with C <sub>6</sub> H <sub>13</sub> I. Both E <sub>11</sub> <sup>-</sup> and E <sub>T</sub> energy shifts are clearly resolved in each PL peak.....	101
<b>Table 4-2.</b> PL results of (6,5)-SWCNT-trions with various functional groups.....	102

## List of Figures

<b>Figure 1-1.</b> Schematic illustration of an exciton in a semiconductor. <b>a</b> , an electron is promoted from the valence band to the conduction band by absorption of a photon ( $h\nu$ ) leaving behind a hole. <b>b</b> , the electron and the hole are correlated by coulombic attraction screened by the medium to form an exciton.....	2
<b>Figure 1-2.</b> Schematic exciton models. <b>a</b> , the hydrogen atom as an analogy of exciton. Schematic illustration of <b>b</b> , Wannier-Mott (left) model and <b>c</b> , Frenkel model (right) and their electronic structures (bottom). Note: Figure not drawn to scale. ....	4
<b>Figure 1-3.</b> Schematic representation of controlling energy level structure of semiconducting nanocrystals arising from quantum confinement effects. ....	7
<b>Figure 1-4.</b> Schematic illustration of density of state (DOS) as a function of energy for 3D bulk, 2D, 1D and 0D.....	9
<b>Figure 1-5.</b> Structure of SWCNT, DWCNT, and MWCNT. ....	10
<b>Figure 1-6.</b> Structure of SWCNTs. The $(n, m)$ nanotube naming scheme as a vector ( $C_h = na_1 + ma_2$ ) in an infinite graphene sheet (top). The three different types of SWCNTs by chiral angle ( $\Theta$ ) (bottom).....	11
<b>Figure 1-7.</b> Electronic structure and optical properties of SWCNTs. <b>a</b> , Electronic energy level of a semiconducting SWCNT as a function of DOS. <b>b</b> , Absorption spectra and <b>c</b> , excitation-emission 3D map of HiPco SWCNTs individually dispersed in 1 % SDS-water.....	13
<b>Figure 1-8.</b> Excitonic states of SWCNTs. 16 different exciton states of SWCNT including 4 singlets and 12 triplets where only the exciton from bright singlet state can radioactively recombine. ....	16

**Figure 1-9.** Schematic view of an exciton and a trion. **a**, An electron (blue)-hole (red) pair, exciton, in a undoped SWCNT. **b**, A negatively charged exciton – the bound state of a hole and two electrons in a SWCNT..... 20

**Figure 2-1.** The fluorescent quantum defect approach to material engineering. **a**, In a quantum confinement system, the exciton wavefunction is confined as the particle size reaches the Bohr radius of the quasi-particle, lending the capability to control optical properties by size engineering. **b**, In the proposed quantum defect systems, the mobile excitons can be trapped and their optical properties can be controlled by molecular engineering of the trap. **c**, The creation of a fluorescent quantum defect by reacting a SWCNT semiconductor with different types of alkyl iodides (R-I). ..... 29

**Figure 2-2.** Chemical creation of fluorescent (6,5)-SWCNT-CF<sub>2</sub>(CF<sub>2</sub>)<sub>4</sub>CF<sub>3</sub>. **a**, Defect photoluminescence arises farther in the near-infrared, 190 meV to the red of the parent nanotube excitonic emission. **b**, Correlated visible near-infrared absorption (black line) and PL (red line) spectra for (6,5)-SWCNT-CF<sub>2</sub>(CF<sub>2</sub>)<sub>4</sub>CF<sub>3</sub>. The SWCNTs are excited at the E<sub>22</sub> transition (565 nm). **c**, Evolution of E<sub>11</sub> and E<sub>11</sub><sup>-</sup> emission..... 34

**Figure 2-3.** Control reactions with different reagent conditions. Emission spectra are monitored with 565 nm excitation at 0 h, 2 h, 24 h, 3 days and 7 days. Only the reaction condition (a) shows the strong defect PL (E<sub>11</sub><sup>-</sup>). .. 35

**Figure 2-4.** Emission energy of defect photoluminescence is dependent on the nanotube diameter. All chirality enriched carbon nanotube are used and functionalized with -C<sub>6</sub>F<sub>13</sub> groups..... 37

**Figure 2-5.** Nanotube structure-dependent defect photoluminescence. The excitation-emission maps of **a**, (6,5)-SWCNT; **b**, (8,3)- and (8,4)-SWCNT; **c**, (7,6)- and (8,4)-enriched SWCNTs; and **d**, the mixed chirality of HiPco. Controlled sidewall alkylation induces new PL peaks in **e**, (6,5)-SWCNT-CF<sub>2</sub>(CF<sub>2</sub>)<sub>4</sub>CF<sub>3</sub>; **f**, (8,3)/(8,4)-SWCNT-CF<sub>2</sub>(CF<sub>2</sub>)<sub>4</sub>CF<sub>3</sub>; **g**, (7,6)/(8,4)-SWCNT-CF<sub>2</sub>(CF<sub>2</sub>)<sub>4</sub>CF<sub>3</sub>; and **h**, HiPco-SWCNT-CF<sub>2</sub>(CF<sub>2</sub>)<sub>4</sub>CF<sub>3</sub>. The nanotubes are stabilized in D<sub>2</sub>O by 1 wt.% SDS. .... 37

<b>Figure 2-6.</b> Emission spectra of (6,5)-pristine and (6,5)-SWCNT-(CF <sub>2</sub> ) <sub>5</sub> CF <sub>3</sub> that show the brightening PL by more than an order of magnitude.....	38
<b>Figure 2-7.</b> Correlated spectral characterization of functionalized SWCNTs at increasing molar reactant ratios of CF <sub>3</sub> (CF <sub>2</sub> ) <sub>4</sub> CF <sub>2</sub> I (RX) to the mixed chirality of HiPco SWCNT carbon. <b>a</b> , Raman scattering. The excitation line is 532 nm. <b>b</b> , XPS (taken at 25 °C). The O1s peak is marked with an asterisk (*). <b>c</b> , PL. <b>d</b> , The ratio of covalently attached function group to nanotube carbon, [R]/[C], as determined from XPS, increases linearly with the reactant ratio, [RX]/[C]. <b>e</b> , Raman D/G ratio of SWCNT-CF <sub>2</sub> (CF <sub>2</sub> ) <sub>4</sub> CF <sub>3</sub> at increasing [RX]/[C].....	39
<b>Figure 2-8.</b> High resolution XPS of C 1s at 175 °C for SWCNT-CF <sub>2</sub> (CF <sub>2</sub> ) <sub>4</sub> CF <sub>3</sub> . <b>a</b> , Non-functionalized control. <b>b</b> , [C]:[RX] = 1:50. <b>c</b> , 1:500. <b>d</b> , 1:2500. The nanotubes used here are a sample of mixed chirality HiPco SWCNTs. ....	40
<b>Figure 2-9.</b> High resolution XPS of F 1s at 175 °C for SWCNT-CF <sub>2</sub> (CF <sub>2</sub> ) <sub>4</sub> CF <sub>3</sub> . <b>a</b> , Non-functionalized control. <b>b</b> , [C]:[RX] = 1:50, <b>c</b> , 1:500, and <b>d</b> , 1:2500. ....	41
<b>Figure 2-10.</b> High resolution XPS of full spectra at 175 °C for SWCNT-CF <sub>2</sub> (CF <sub>2</sub> ) <sub>4</sub> CF <sub>3</sub> . <b>a</b> , Non-functionalized control. <b>b</b> , [C]:[RX] = 1:50, <b>c</b> , 1:500, and <b>d</b> , 1:2500. ....	41
<b>Figure 2-11.</b> Correlated spectral characterization of <i>f</i> -CoMoCAT SWCNTs at increasing ratio of -C <sub>6</sub> F <sub>13</sub> groups. <b>a</b> , PL, <b>b</b> , absorption, and <b>c</b> , Raman D/G ratio as a function of [RX]/[C] molar ratio. Raman spectra with <b>d</b> , 632.8 nm and <b>e</b> , 532 nm excitation laser, respectively. ....	42
<b>Figure 2-12.</b> Tunable near-infrared PL from quantum defect-tailored (6,5)-SWCNTs with six-carbon alkyl chains with increasing numbers of fluorine substituents. ....	44
<b>Figure 2-13.</b> Correlated UV-Vis-NIR absorption and PL of (6,5)-SWCNTs with different functional groups.....	46

<b>Figure 2-14.</b> Emission spectra of (6,5)-SWCNTs with six carbon alkyl chains before peakfitting. Note that the additional satellite peaks are observed and marked as asterisk (*) arising from a charged exciton (trion).....	46
<b>Figure 2-15.</b> PL energy shifts versus calculated inductive constant ( $\sigma^*$ ). <b>a</b> , $C_6H_{13-n}F_n$ ( $n = 0, 3, 5, 9,$ and $13$ ). <b>b</b> , $-(CH_2)_nCF_3$ ( $n = 0 - 5$ ). <b>c</b> , The combined graph of <b>a</b> and <b>b</b> .....	47
<b>Figure 2-16.</b> Energy shift Vs calculated inductive constant with non-, partially-, and per-fluorinated alkyl groups.....	49
<b>Figure 2-17.</b> (6,5)-SWCNT $>CF_2$ . <b>a</b> , PL maps of pristine SWCNTs (left) and divalent alkyl-functionalized SWCNTs (right). <b>b</b> , 565 nm excitation emission spectra, <b>c</b> , UV-Vis-NIR Absorption spectra, <b>d</b> , Raman spectra with 532 nm laser and <b>e</b> , Raman spectra with 632.8 nm laser. The pristine is black solid and the <i>f</i> -SWCNTs are red solid line.....	50
<b>Figure 2-18.</b> Creation of <b>a</b> , monovalent and <b>b</b> , divalent aryl defects of aminobenzene-(6,5)-SWCNTs. The aryl defect is created by excitation light (300-800 nm) without sodium dithionite. Single emission spectra are obtained with 565 nm excitation light and normalized by $E_{11}$ .....	51
<b>Figure 2-19.</b> Comparison of monovalent and divalent fluorescent quantum defects. The nanotubes are excited at 565 nm. The parent exciton PL occurs at 979 nm while emission from the quantum defects are systematically tunable by changing the functional group including - $CH_3$ , $>CH_2$ , $-C_6H_5$ , and $>C_6H_4$ . The spectra are fitted with Voigt functions.....	53
<b>Figure 2-20.</b> Excitation-emission maps of (6,5)-SWCNTs with chemically tailored fluorescent quantum defects.....	54
<b>Figure 2-21.</b> Schematic illustration of four classes of quantum defects.....	55
<b>Figure 2-22.</b> pH-responsive defect photoluminescence. <b>a</b> , monovalent and <b>b</b> , divalent aminobenzene-functionalized (6,5)-SWCNTs.....	57
<b>Figure 2-23.</b> Mulliken charge distribution in a pristine (6,5)-SWCNT and single functional group attached SWCNTs (side view). Charges are shown in	

color gradient scheme, where red, black, and green colors are negative, zero, and positive charges, correspondingly. ....	59
<b>Figure 2-24.</b> Distribution of Mulliken charges in (6,5)-SWCNTs with a single monovalent defect (left) and the relative energy diagrams when double monovalent defects are attached (right). <b>a</b> , -CH <sub>3</sub> . <b>b</b> , -CF <sub>3</sub> . Note that the most thermodynamically stable structure of methyl functionalized (6,5)-SWCNT is 1,4-para position (m), where the Mulliken charges are highly negative. ....	61
<b>Figure 2-25.</b> Distribution of Mulliken charges in (6,5)-SWCNTs with a single divalent defect (left) and the relative energy diagrams of (6,5)-SWCNTs with two divalent defects (right). <b>a</b> , >CH <sub>2</sub> . <b>b</b> , >CF <sub>2</sub> . ....	62
<b>Figure 2-26.</b> Bond lengths of (6,5)-SWCNT>CH <sub>2</sub> . C-C bond length around the >CH <sub>2</sub> defect is slightly longer than that in the pristine SWCNT (1.42 Å). The circumferential C-C bond at the defect site is increased to 2.17 Å and thus is broken to adopt an opened three-membered ring.....	63
<b>Figure 2-27.</b> Localization of charges and frontier orbital wavefunction around a fluorescent quantum defect. <b>a</b> , HOMO and <b>b</b> , charge distribution in a pristine (6,5)-SWCNT. The nanotube is free of defects other than its ends, which are terminated with hydrogen atoms to preserve the <i>sp</i> <sup>2</sup> hybridization. <b>c</b> , HOMO of a (6,5)-SWCNT-CF <sub>3</sub> . Inset shows the HOMO for -CF <sub>3</sub> functionalization on a cut perpendicular to the tube. The orbital is plotted at its iso-surface equal to 0.003. <b>d</b> , Positive (green) and negative (red) charges. ....	65
<b>Figure 2-28.</b> The HOMO and LUMO of pristine-SWCNTs and (6,5)-SWCNTs with >CH <sub>2</sub> , -CH <sub>3</sub> , >CF <sub>2</sub> , and -CF <sub>3</sub> . ....	66
<b>Figure 3-1.</b> Sketch of optical probing of pH through defect photoluminescence in a SWCNT.....	69
<b>Figure 3-2.</b> Defect photoluminescence arises from <i>sp</i> <sup>3</sup> defects. Excitation-emission PL maps of <b>a</b> , pristine and <b>b</b> , <i>N,N</i> -diethylaminobenzene functionalized (6,5)-SWCNTs. <b>c</b> , Emission spectra at 565 nm excitation of pristine (6,5)-SWCNTs (black) and (6,5)-SWCNT-C <sub>6</sub> H <sub>4</sub> N(CH <sub>2</sub> CH <sub>3</sub> ) <sub>2</sub>	

when the  $E_{11}/E_{11}^-$  intensity ratio is 1:1 (blue) and 1:2 (red), respectively. The functionalized SWCNTs show 1.3 - 2.4-fold enhancement of the PL. **d**, UV-Vis-NIR absorption spectra of pristine (black) and (6,5)-SWCNT- $C_6H_4N(CH_2CH_3)_2$  with an  $E_{11}/E_{11}^-$  intensity ratio of 1:2 (red). .. 74

**Figure 3-3.** Schematic illustration of NIR-II pH sensor based on carbon nanotube antenna-amplified defect photoluminescence. Protonation of an aminobenzene functional group covalently attached on a (6,5)-SWCNT modifies the energy level of the  $sp^3$  defect state from which a new photoluminescence arises. The nanotube acts as an optical antenna that efficiently harvests light and channels the generated excitons to the defect site, where the excitons recombine to produce near-infrared photoluminescence encoding the chemical information at the functional groups (red arrow)..... 75

**Figure 3-4.** Defect photoluminescence of (6,5)-SWCNT- $C_6H_4N(CH_2CH_3)_2$  is strongly dependent on pH. **a**, The  $E_{11}^-$  emission of the *N,N*-diethyl-4-aminobenzene functionalized (6,5)-SWCNTs redshifts from 1117 nm to 1136 nm, as the pH changes from 9.02 to 3.97. The  $E_{11}$  and  $E_{11}^-$  emission curves (solid lines) are fitted and plotted on top of the original data (dotted lines). The difference is due to (6,4)-impurity in the solution, marked with an asterisk (\*). **b**, The  $E_{11}^-$  emission responds sensitively to the pH change whereas  $E_{11}$  remains unchanged. **c**, The first derivative of the relative PL energy shift of  $E_{11}$  and  $E_{11}^-$  as a function of pH determines the  $pK_a$  for the nanoprobe. .... 75

**Figure 3-5.** Defect PL of (6,5)-SWCNT- $C_6H_4N(CH_2CH_3)_2$  at different pH is a convolution of two states: protonated state (red) and deprotonated state (blue). The solid lines are fitted peaks and the dotted lines are the original data..... 78

**Figure 3-6.** Chirality dependent pH response of *N,N*-diethylaminobenzene functionalized SWCNTs. **a**, The energy shifts between pH 9.0 and pH 4.0 ( $\Delta E$ ) vary from 18 to 33 meV depending on the nanotube chirality. Defect photoluminescence of **b**, (6,5)/(6,4)-SWCNT- $C_6H_4N(CH_2CH_3)_2$  and **c**, (8,3)/(8,4)-SWCNT- $C_6H_4N(CH_2CH_3)_2$ . .... 80

- Figure 3-7.** Chirality dependent pH response of *N,N*-diethylaminobenzene functionalized SWCNTs at E<sub>22</sub> excitation..... 81
- Figure 3-8.** Temperature-dependent defect photoluminescence of (6,5)-SWCNT-C<sub>6</sub>H<sub>4</sub>N(CH<sub>2</sub>CH<sub>3</sub>)<sub>2</sub>. **a**, Evolution of E<sub>11</sub> and E<sub>11</sub><sup>-</sup> PL from protonated (6,5)-SWCNT-C<sub>6</sub>H<sub>4</sub>N(CH<sub>2</sub>CH<sub>3</sub>)<sub>2</sub> with increasing temperature at pH 3.77. **b**, Schematic illustration of thermal promotion of an exciton from the defect state (E<sub>11</sub><sup>-</sup>) to the higher E<sub>11</sub> state. The relative exciton population is correlated with the relative energy of the defect states. **c**, The van't Hoff plots (the E<sub>11</sub>/E<sub>11</sub><sup>-</sup> integrated intensity ratios as a function of temperature) at pH 3.77 (red) and pH 9.01 (blue). The slope of linear regression is used to determine the relative E<sub>11</sub><sup>-</sup> energy between the protonated and de-protonated states of the aminobenzene substituents. **d**, Simplified energy diagram of (6,5)-SWCNT-C<sub>6</sub>H<sub>4</sub>N(CH<sub>2</sub>CH<sub>3</sub>)<sub>2</sub> at pH 3.77 and pH 9.01. .... 83
- Figure 3-9.** pH measurement in biological media through defect photoluminescence. **a**, The relative PL energy shift of E<sub>11</sub> and E<sub>11</sub><sup>-</sup> as a function of pH. **b**, The pH of 10% v/v fetal bovine serum in DMEM is measured optically with (6,5)-SWCNT-C<sub>6</sub>H<sub>4</sub>N(CH<sub>2</sub>CH<sub>3</sub>)<sub>2</sub>. The PL shift between pH 3.7 (blue) and 9.0 (red) in the biological media is identical to that obtained from aqueous solutions. The excitation wavelength is 565 nm..... 85
- Figure 3-10.** The PL intensity of (6,5)-SWCNT-C<sub>6</sub>H<sub>4</sub>N(CH<sub>2</sub>CH<sub>3</sub>)<sub>2</sub> as a function of pH. All emission spectra were taken at 565 nm under identical spectral conditions. Integrated area is the sum of both E<sub>11</sub> and E<sub>11</sub><sup>-</sup>. The full width at half maximum barely changed across the pH 3-9 range, with a FWHM of 40.6 ± 3 nm for E<sub>11</sub> and 82.9 ± 3 nm for E<sub>11</sub><sup>-</sup>, respectively. .... 86
- Figure 3-11.** Salt effects on pH response of defect photoluminescence with (6,5)-SWCNT-C<sub>6</sub>H<sub>4</sub>N(CH<sub>2</sub>CH<sub>3</sub>)<sub>2</sub>. All emission spectra were taken at 565 nm under identical spectral conditions..... 87
- Figure 4-1.** Defect-bound triions developed by the new alkylation method. The 3D PL maps of **a**, pristine (6,5)-SWCNTs and **b**, the hexyl functionalized

(6,5)-SWCNTs. The new PL features at 1095 nm and 1225 nm are assigned to  $E_{11}^-$  and  $E_T$ , respectively. The defect PL shows a collective quantum yield 18-fold higher than that of the un-functionalized SWCNTs. .... 94

**Figure 4-2.** Schematic energy diagram of exciton and trions in a semiconducting SWCNT. **a**, An exciton diffuses along a unfunctionalized SWCNT followed by non-radiative (dark) and radiative ( $E_{11}$ ) or trion ( $E_T$ ) pathway. **b**, In a functionalized SWCNT, the  $sp^3$  defect centers act as an exciton trap to harvest dark excitons resulting in brightening of both  $E_{11}^-$  and  $E_T$ . .... 95

**Figure 4-3.** Evolution of defect PL monitored with *in situ* photoluminescence spectroscopy. **a**, The PL intensity of  $E_{11}$ ,  $E_{11}^-$  and  $E_T$  as a function of reaction time. The emission spectra of (6,5)-SWCNT are obtained with 565 nm single excitation. The intensity of trion photoluminescence increases with the relative RX concentration while the intensity of  $E_{11}^-$  PL reached the maxima at  $[C]:[C_6H_{13}I] = 1:0.10$ . **b**, The  $E_{11}$ ,  $E_{11}^-$  and  $E_T$  emission wavelength as a function of reaction time. **c**, The emission spectra when excited at 565 nm and **d**, 3D PL maps after 2 hours. The concentration of  $[C]:[C_6H_{13}I]$  is 0.06, 0.07, 0.10, 0.70, and 4.00 from left to right. .... 97

**Figure 4-4.** Covalent functionalization of (6,5)-SWCNTs- $C_6H_{13}$  produce controlled defect photoluminescence. **a**, 565 nm emission spectra, **b**, 3D excitation-emission contour maps **c**, UV-Vis-NIR absorption spectra, and **d**, Raman spectra at 532 nm excitation laser of (6,5)-enriched SWCNTs functionalized with  $C_6H_{13}I$  at different concentrations, where  $[C]:[RX]$  is 1, 2, 4, 12, 24, and 48. .... 98

**Figure 4-5.** Trion formation in (6,5)-SWCNT- $C_6H_{13}$  strongly depends on defect density. **a**, Raman  $I_D/I_G$  ratio as a function of molar ratio of  $[RX]/[C]$ . As the concentration of reagents increase, the D mode in Raman is enhanced for both 2.33 eV and 1.96 eV excitation laser. **b**, Relative PL intensity over Raman  $I_D/I_G$  ratio. .... 99

**Figure 4-6.** Chirality dependence of  $E_{11}^-$  and  $E_T$  with hexyl-functionalized SWCNTs. **a**, Both  $E_{11}^-$  (blue triangle) and  $E_T$  (red circle) energy shifts show a strong chirality dependence with respect to dark exciton brightening. **b**,  $E_T$  energy shift as a function of diameter. This further supports  $(2n + m)$  family pattern which is consistent with previously reported trions in unfunctionalized SWCNTs..... 100

**Figure 4-7.** Functional group dependence of  $E_{11}^-$  and  $E_T$  in (6,5)-SWCNTs. **a**, PL maps of (6,5)-SWCNTs with non- ( $-C_6H_{13}$ ), partially- ( $-C_2H_4C_4F_9$ ), and perfluorinated hexyl ( $-C_6F_{13}$ ) groups. **b**,  $E_{11}^-$  and  $E_T$  energy shifts Vs Taft constant( $\sigma^*$ ). Both defect PLs are clearly related to the Taft constants while  $E_T$  shows less dependence on electronic effects compared to  $E_{11}^-$ ..... 102

**Figure 4-8.** Temperature-dependence of  $E_{11}^-$  and  $E_T$  for (6,5)-SWCNTs- $C_6H_{13}$ . **a**, Integrated PL intensity and **b**, 565 nm emission spectra as a function of temperature. The van't Hoff plots are constructed from integrated PL intensity of **c**,  $E_{11}/E_{11}^-$  and **d**,  $E_{11}^-/E_T$ . ..... 104

**Figure 4-9.** Trion intensity of (6,5)-SWCNT- $C_6H_{13}$  strongly depends on solution pH. **a**, Integrated PL intensity as a function of pH. **b**, 565nm emission spectra under different pH. pH dependence is reproducible and reversible from acidic to basic, or vice versa. .... 105

## List of Abbreviations

**Abs:** Absorbance

**Ar:** Aryl

**ATP:** Aqueous Two Phase

$a_0^*$ : Exciton Bohr Radius

**CB:** Conduction Band

**CNT:** Carbon Nanotube

**CoMoCAT:** Cobalt–Molybdenum Catalyst

**D/G:** Raman intensity ratio of Disorder mode and G band

**DFT:** Density Functional Theory

**DOS:** Density of State

**DWCNT:** Double Walled Carbon Nanotube

**Dz:** Diazonium

**E<sub>g</sub>:** Band Gap, Energy difference between the top of conduction band and the bottom of valence band

**E<sub>11</sub>:** Excitonic SCWNT energy transition between the first valence and conduction

**E<sub>11</sub>':** Defect induced SWCNT intra-bandgap transition

**E<sub>22</sub>:** Excitonic SWCNT energy transition between the second valence and conduction band van Hove singularities

**E<sub>T</sub>:** Intra-bandgap SWCNT trion transition

**EL:** Electroluminescence

**FWHM:** Full Width at Half Maximum

***f*-SWCNT:** Functionalized Single-Walled Carbon Nanotube

**HiPco:** High-Pressure Carbon Monoxide

**HOMO:** Highest energy Occupied Molecular Orbital

**I<sub>11</sub>:** Integrated intensity of E<sub>11</sub>

**I<sub>11</sub><sup>\*</sup>:** Integrated intensity of E<sub>11</sub><sup>\*</sup>

**I<sub>T</sub>:** Integrated intensity of E<sub>T</sub>

**LUMO:** Lowest energy Unoccupied Molecular Orbital

**MWCNT:** Multi Walled Carbon Nanotube

**NIR-I:** First Near-infrared

**NIR-II:** Second Near-infrared

**pKa:** Acid dissociation constant

**PL:** Photoluminescence

**QD:** Quantum Dot

**QW:** Quantum Well

**QY:** Quantum Yield

**RBM:** Radial Breathing Mode

**R<sub>y</sub>:** Rydberg Energy

**R<sub>y</sub><sup>\*</sup>:** Rydberg Exciton Energy

**RX:** Alkyl Halide

**SEM:** Scanning Electron Microscopy

**SDS:** Sodium Dodecyl sulfonate

**SWCNT:** Single Walled Carbon Nanotube

**TGA:** Thermogravimetric analysis

**UV-Vis-NIR:** Ultraviolet-Visible-Near-Infrared

**VB:** Valence Band

**VHS:** Van Hove Singularities

**Wt.:** Weight

**X<sup>+</sup>:** Positive Trion

**X<sup>-</sup>:** Negative Trion

**XPS:** X-ray Photoelectron Spectroscopy

# Chapter 1 . Introduction and Overview

In this chapter, the definitions, models of excitons, and their effects on the electronic and optical properties of semiconductors will be discussed. We will focus on low-dimensional nanomaterials, particularly carbon nanotubes, and influence of defects and charges on their optical and electronic properties.

## 1.1. Excitons in nanomaterials

### 1.1.1. Excitons: definitions and models

Semiconductors have a band-gap ( $E_g$ ) between the valence band maximum (VB) and the conduction band minimum (CB) (Fig. 1-1). Optical excitation of semiconductors causes an electron (e) transition from the valence band to the conduction band, leaving behind a “hole (h)” in the VB. The excited electron can strongly interact with the hole due to electrostatic coulombic attraction by forming a bound state of the e-h pair, defined as an exciton. In a perfect semiconductor, the number of electrons remains constant in the case of optical excitation with photon energies in an electronvolt (eV) or band gap region while it brings the system of electrons from the ground state to excited states. Excitons are stabilized due to the overlap of the electron and hole wave functions, resulting in an extended lifetime (typically  $10^{-9}$  s in semiconductors)<sup>1</sup>. The excited electron can hop back into the VB by releasing their excess energy, defined as recombination. Excitons can be described with various concepts such as hydrogen analogy, Frenkel model and Wannier model.

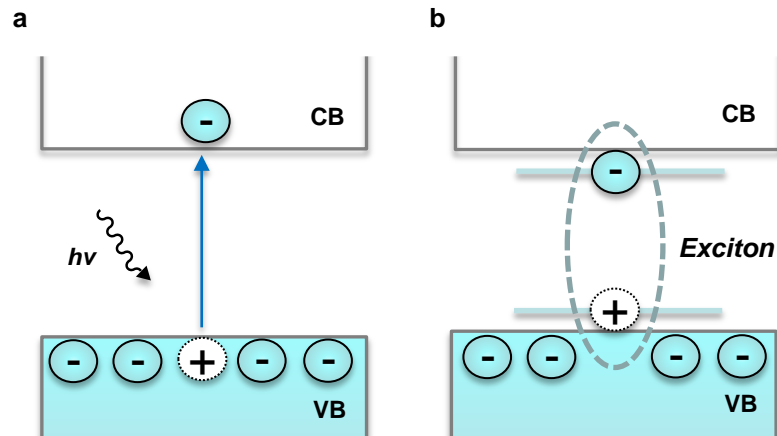


**Figure 1-1.** Schematic illustration of an exciton in a semiconductor. **a**, an electron is promoted from the valence band to the conduction band by absorption of a photon ( $h\nu$ ) leaving behind a hole. **b**, the electron and the hole are correlated by coulombic attraction screened by the medium to form an exciton.

First, an exciton is understood as analogous to a hydrogen atom (Fig. 1-2a)<sup>1</sup>,  
<sup>2</sup>. The energy required for an electron to be dissociated from the nucleus of a hydrogen atom is called hydrogen ionization energy or Rydberg energy ( $R_y$ ,  $\sim 13.6$  eV). Likewise, the exciton binding energy is called Rydberg Exciton Energy ( $R_y^*$ ) and the exciton radius is defined as a distance between an electron and a hole, called exciton Bohr Radius ( $a_0^*$ ). The exciton binding energy and radius can be calculated,

$$R_y^* = \frac{1}{\epsilon_r^2} \frac{\mu}{m_e} R_y \quad \text{Exciton Rydberg Energy} \quad \text{eq (1)}$$

$$a_0^* = a_0 \epsilon_r \frac{m_e}{\mu} \quad \text{Excitonic Bohr Radius} \quad \text{eq (2)}$$

where  $\epsilon_r$  is the relative permittivity,  $m_e$  is the mass of an electron,  $\mu$  is reduced exciton mass, and  $a_0$  is Bohr Radius. Using the material parameters for typical semiconductors, we find<sup>2</sup>

$$1 \text{ meV} \leq R_y^* \leq 200 \text{ meV} \ll E_g \quad \text{eq (3)}$$

and

$$50 \text{ nm} \geq a_0^* \geq 1 \text{ nm} \quad \text{eq (4)}$$

This estimation shows that the exciton binding energy in semiconductors is typically in the range of a few to hundreds of meV, which is much smaller than that of hydrogen. It is explained by smaller effective electron and hole masses than the free electron and proton masses in hydrogen nucleus. For example, in GaAs, the electron effective mass is  $m_e = 0.067m_0$  and the-hole mass is  $m_h = 0.45m_0$  where  $m_0$  is the free electron mass in vacuum. Also, the screening of the Coulomb force by other electrons in the semiconductor reduces the exciton binding energy by roughly an order of magnitude less than that of hydrogen.

The interesting point is in eq (4), which shows the larger orbits of electron and hole around their common center of mass average over many unit cells. This type of exciton is called Wannier-Mott excitons, introduced by the Swiss physicist Gregory Wannier and English theorist Nevil Francis Mott in 1937 (Fig. 1-2b)<sup>3</sup>. The concept of Wannier-Mott excitons fits well with semiconducting inorganic crystals with small energy gaps and high dielectric constants such as Ge, GaAs, and CdS. This model describes electrons and holes as free particles having a parabolic dispersion, which can be characterized by effective mass approximation. It allows neglecting the periodic crystal potential and the effective masses of carriers are

lighter than the free electron mass in vacuum  $m_0$ . The Wannier-Mott excitons move like free particles and the exciton size can extend over many unit cells and its binding energy is only few millielectronvolts.

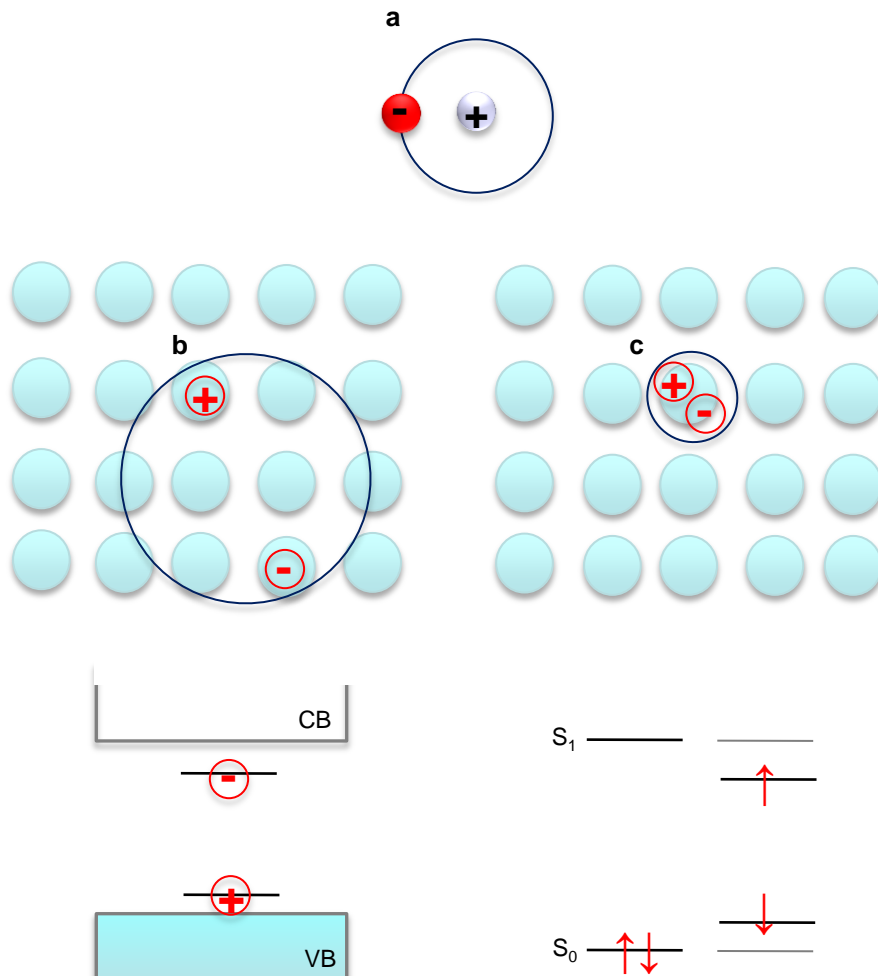


**Figure 1-2.** Schematic exciton models. **a**, the hydrogen atom as an analogy of exciton. Schematic illustration of **b**, Wannier-Mott (left) model and **c**, Frenkel model (right) and their electronic structures (bottom). Note: Figure not drawn to scale.

It should be mentioned that the first concept of excitons was introduced by Russian theorist Yakov Frenkel in 1931<sup>4</sup> before the Wannier-Mott model. He treated the crystal potential as a perturbation to the Coulomb interaction between an electron and a hole which exist in one unit cell (Fig. 1-2c). Unlike the Wannier model, this model is most effect in insulators such as salts (*e.g.* NaCl) and organic crystals (*e.g.* anthracene), but not valid for semiconducting materials and effective mass approximation. The binding energy of Frenkel excitons can be relatively large, up to several hundred meVs and the motion of Frenkel excitons can be describe as hopping from one site to another. It is useful to illustrate molecular pictures of excitons such as singlet and triplet states from a localized exciton<sup>5</sup>.

The simple exciton pictures have given a basic understanding of excitons in nanomaterials although there is controversy concerning these early models introduced in the 1930s, and some appropriate corrections to the simple exciton model have been determined<sup>2</sup>. Excitons in semiconducting carbon nanotubes (CNTs) are believed to have both Frenkel and Wannier-Mott exciton characteristics. Due to strong coulombic interaction in reduced dimensional nanostructures, carbon nanotube excitons have relatively strong binding energies, ranging from a few hundred meV to 1 eV similar to Frenkel exciton<sup>6</sup>. On the other hand, the exciton radius extends over several nanometers like the Wannier-Mott model from semiconducting crystals because the exciton wavefunction delocalizes along the circumference due to reduced dimensionality and high dielectric constant.

### 1.1.2. Quantum confinement effects in nanomaterials

Nano-size semiconducting materials have different electronic and optical properties from bulk materials that should be taken into account for complete understanding of fundamental exciton properties. When the nanomaterial size is smaller than an exciton Bohr radius ( $a_0^*$ ), the exciton wavefunction is confined and the energy levels of the material can split, resulting in very different electronic and optical properties from bulk materials. This is defined as the “confinement effect”<sup>7</sup>. This phenomenon can be explained by using the classical particle-in-a-box model. In the absence of a defect, a particle or an excitation is described in terms of Bloch waves and the crystal is finite by two fixed barriers, separated by a distance  $L$ . The Bloch waves are then said to be spatially confined along the  $z$  direction.

$$\lambda = 2L/n, \quad n = 1, 2, 3, \dots \quad \text{eq (5)}$$

where  $\lambda$  is a wavelength and  $L$  is distance between two barriers. A wavevector  $k_z$  of Bloch waves in a confined crystal is given by

$$k_z = 2\pi/\lambda_n = n\pi/L, \quad n = 1, 2, 3, \dots \quad \text{eq (6)}$$

The ground state of energy is increased by the amount of energy, referred to as the confinement energy of the particle ( $\Delta E_{\text{confinement}}$ )

$$\Delta E_{\text{confinement}} = \frac{\hbar^2 k_z^2}{2m^*} = \left( \frac{\hbar^2}{2m^*} \right) \left( \frac{\pi^2}{L^2} \right), \quad \text{eq (7)}$$

where the  $m^*$  is effective mass of the free particle and  $\hbar$  is the reduced Planck's constant. Here, we can see the confinement energy is inversely proportional to the square of the particle size,  $L$ , or exciton Bohr radius ( $a_0$ ). In addition to  $\Delta E_{\text{confinement}}$ , the exciton binding energy ( $\Delta E_{\text{exciton}}$ ) also need to be considered to understand the electronic properties of excitons in semiconductors (eq (4)) because this attraction

provides stabilizing energy resulting in a slightly lower energy gap compared to the unbounded electron and hole. It is described as a negative energy in eq (8) from eq (1)

$$\Delta E_{\text{exciton}} = -\frac{1}{\epsilon_r^2} \frac{\mu}{m_e} R_y = -R_y^* \quad \text{eq (8)}$$

This energy also strongly depends on size (see size related term,  $\epsilon_r$ ). Therefore, the energy in confined nanostructures can be explained as eq (9) in a nanocrystal.

$$\begin{aligned} E &= \Delta E_{\text{bandgap}} + \Delta E_{\text{confinement}} + \Delta E_{\text{exciton}} \\ &= \Delta E_g + \left(\frac{\hbar^2}{2m^*}\right)\left(\frac{\pi^2}{a_0^2}\right) - R_y^* \end{aligned} \quad \text{eq (9)}$$

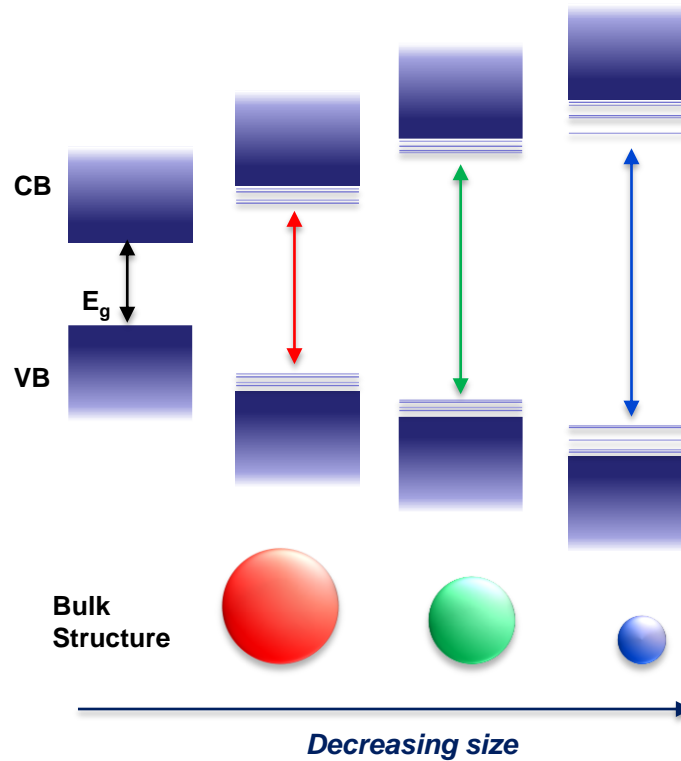


**Figure 1-3.** Schematic representation of controlling energy level structure of semiconducting nanocrystals arising from quantum confinement effects.

As we can see in eq (9), the energy in a confined system is substantially influenced by the size of the particle and thus its excited state energies become quantized resulting in photon emission at a size-dependent wavelength. Larger size nanocrystals possess smaller band gaps than bulk materials, whereas highly confined smaller nanocrystals have large band gaps (Fig. 1-3)<sup>8</sup>. Size engineering through quantum confinement effects has been the central idea of material nanomaterial engineering and motivated advance synthetic approaches to control electronic properties.

Beside size effects, shapes and dimensionality are also critical factors for confinement effects. Confined structures are classified by their dimensionality: three, two-, one-, and zero-dimensional structure (3D, 2D, 1D and 0D) as shown in Fig. 1-4. The dimensionality is closely related to energy states and excitonic properties. In bulk 3D semiconductors, they have continuous density of states (DOS) and their excitons can move freely in all directions. However, in QDs as a 0D structure, excitons are confined in all three dimensions, which makes them exhibit discrete atom-like energy spectrum. For 1D semiconductors such as quantum wires (QWs) and carbon nanotubes (CNTs), excitons are confined in two dimensions by moving in only one direction changing the of energy levels from continuous to discrete. Highly confined 1D materials have very well defined and quantized energy levels. They have a higher density of electronic states near the edges of the conduction and valence bands, giving sharp discontinuous spikes in their DOS. This is known as the Van Hove singularity (VHS), which presents the

optical properties and provides a highly useful tool for structure assignment that will be discussed in Chapter 1.2.

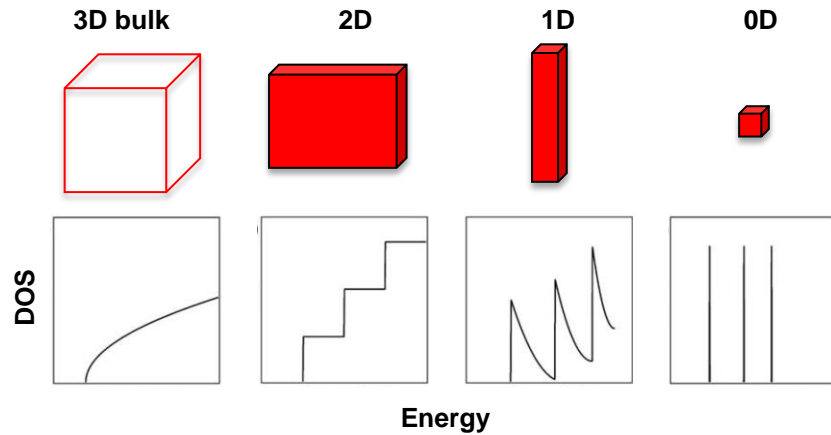


**Figure 1-4.** Schematic illustration of density of state (DOS) as a function of energy for 3D bulk, 2D, 1D and 0D.

## **1.2. Carbon nanotube excitons**

### 1.2.1. Structures of carbon nanotubes

Carbon nanotubes (CNTs) are tube-shaped nanomaterials with only carbon atoms in a hexagonal structure like honeycomb, having a nanometer scale diameter with a several hundred nanometer (or up to millimeters, depending on synthetic process) length. Carbon nanotubes are classified by their structures: single-walled carbon nanotubes (SWCNTs), double-walled carbon nanotubes (DWCNTs), and multi-walled carbon nanotubes (MWCNTs) (Fig. 1-5). DWCNTs are coaxial nanostructures of only two SWCNTs, one nested in another, and MWCNTs are

multiple nested SWCNTs. Carbon nanotubes have many excellent properties including high electrical conductivity ( $4 \times 10^9 \text{ Acm}^{-2}$  for single-walled metallic tube, 1000 times higher than copper), thermal conductivity ( $> 3000 \text{ W}^{-1}\text{K}^{-1}$  for CNTs produced by arc discharge method, comparable with diamond) and mechanical strength (0.2 - 1.8 TPa Young's modulus, ~50 times higher than steel)<sup>9</sup>. DWCNTs and MWCNTs are usually zero-gap metals and have continuous electronic density of states due to strong interlayer interactions. Semiconducting SWCNTs exhibit typical sharp Van Hove singularities (VHSs), a characteristic property of 1D materials<sup>10, 11</sup>. Therefore, semiconducting SWCNTs have been considered as an ideal platform for exciton study.

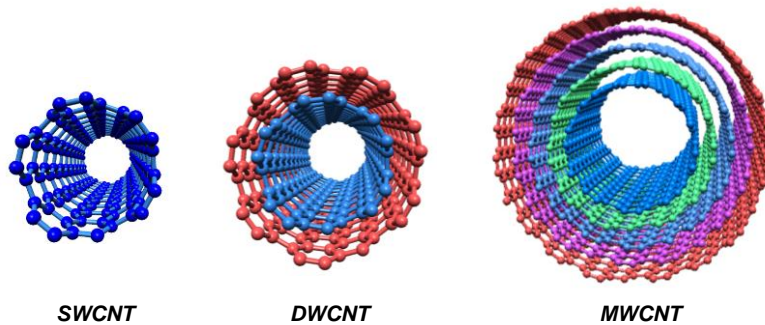


**Figure 1-5.** Structure of SWCNT, DWCNT, and MWCNT.

The structure of SWCNTs is classified by the number of wrapping vectors  $C_h = n a_1 + m a_2$  (Fig. 1.6) and denoted with certain  $(n, m)$  indices. Tubes having  $n = m$  are called "armchair" (chiral angle =  $30^\circ$ ) and if  $m = \text{zero}$ , nanotubes are called "zigzag"(chiral angle =  $0^\circ$ ). Those tubes having chiral angles ( $\theta$ ) between  $0 - 30^\circ$  are called "chiral" (Fig. 1-6)<sup>12</sup>. The electronic properties of SWCNTs strongly

follow their chiral angles. When  $|n - m| = 3j$  ( $j = 1, 2, 3 \dots$ ), metallic properties are found otherwise semiconducting properties are found for  $|n - m| \neq 3j$ . The armchair is metallic, whereas zigzag and chiral can be either semiconducting or metallic. The current synthetic methods provide a mixture of different SWCNT chiralities, rather than a single chirality. There are several techniques that have been developed to separate highly enriched single chirality tubes from the synthetic mixtures that will be discussed in Chapter 1.4.

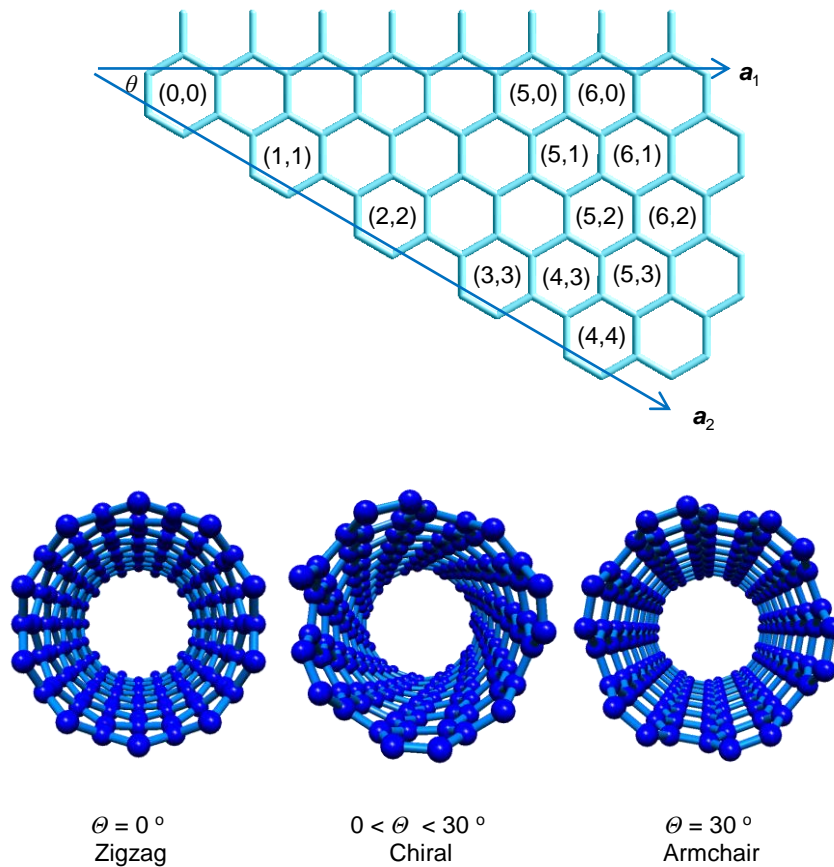


**Figure 1-6.** Structure of SWCNTs. The  $(n, m)$  nanotube naming scheme as a vector ( $C_n = na_1 + ma_2$ ) in an infinite graphene sheet (top). The three different types of SWCNTs by chiral angle ( $\theta$ ) (bottom).

### 1.2.2. Optical properties of single walled carbon nanotubes

The interesting optical properties of carbon nanotubes arise from reduced dimensionality on the nanoscale. The inherited characteristics of sharp VHSs allow selective excitation of a specific nanotube with a certain  $(n, m)$  index in an infinite graphene sheet (Fig 1-7a)<sup>13</sup>. Optical transitions between  $i$ -th valence ( $v_i$ ) and  $i$ -th conduction ( $c_i$ ) band are labeled as  $E_{ii}$ , where  $i$  is the van Hove singularity integer. Only transitions between same van Hove singularity integers (e.g.  $E_{11}$  or  $E_{22}$ , etc), are optically allowed, whereas crossover transitions (e.g.  $E_{12}$  or  $E_{21}$ , etc) are dipole-forbidden<sup>14</sup>. Electronic transitions from  $v_2$  to  $c_2$  ( $E_{22}$ ) or  $v_1$  to  $c_1$  ( $E_{11}$ ) are relatively sharp and are typically used for assigning nanotube types. For example, (6,5) and (7,6)-SWCNTs are distinguished by absorption features. The  $E_{22}$  and the  $E_{11}$  transition of (6,5)-SWCNTs occurs at 565 nm and 980 nm, respectively, while (7,6)-SWCNTs absorb at 585 nm and 1110 nm, respectively, resulting in correspondingly sharp absorption bands (Fig. 1-7b). In the case of ensemble SWCNTs, similar  $E_{22}$  or  $E_{11}$  absorption peaks from different chiralities bring spectral overlapping and broadening of peaks, which make it difficult to observe optical properties from a single chirality.

The other interesting optical properties of semiconducting CNTs emerge from light absorption at photon energy  $E_{22}$  or  $E_{33}$  followed by fluorescence emission at  $E_{11}$ . The  $E_{22}/E_{33}$  excitation and the following  $E_{11}$  emission are plotted as a photoluminescence (PL) map (Fig. 1-7c). This PL map can also be used to assign the chirality of a carbon nanotube. For example, the emission PL peak arising from excitation at 565 nm followed by emission at 980 nm, corresponds to (6,5)-

SWCNTs, while PL peak arising from excitation at 590 nm and emission at 1110 nm is (8,4)-SWCNTs (Fig 1-7c). The emission intensity reaches the maximum when the excitation wavelength resonates with  $E_{22}$  excitation energy. The fluorescence intensity is highly sensitive to interactions occurring from impurities and other chiralities. The energy transfer from semiconducting to metallic or smaller gap semiconducting tubes in bundles can substantially reduce radiative relaxation of the photoexcited exciton. Therefore, isolating a single chirality is one of the critical steps to investigate exciton states using optical spectroscopy.

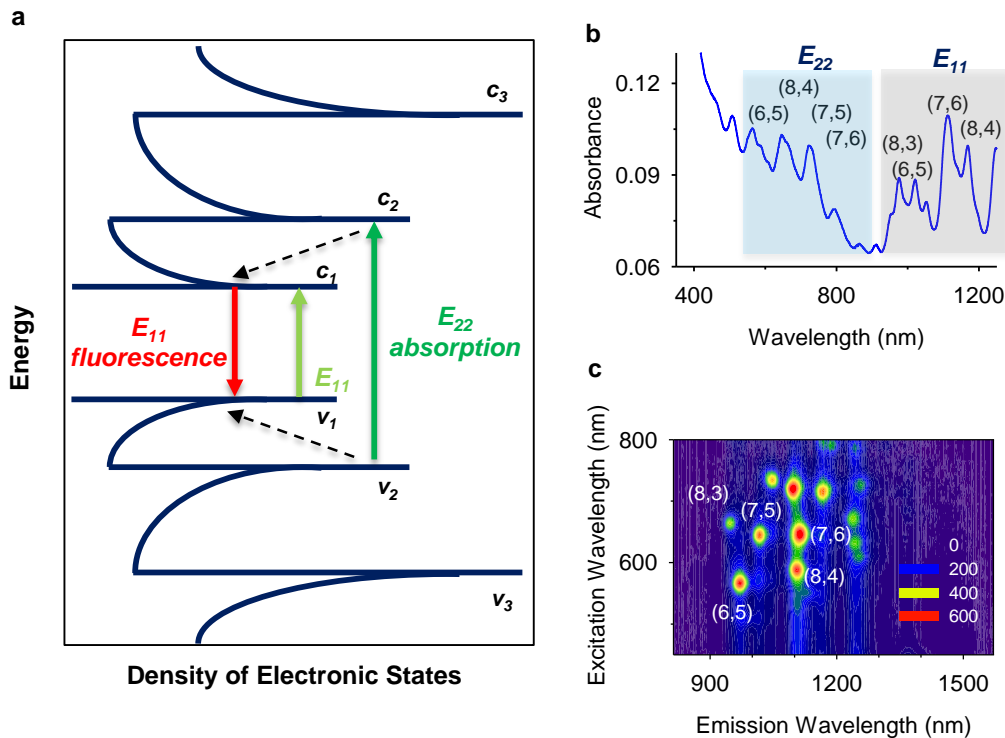


**Figure 1-7.** Electronic structure and optical properties of SWCNTs. **a**, Electronic energy level of a semiconducting SWCNT as a function of DOS. **b**, Absorption spectra and **c**, excitation-emission 3D map of HiPco SWCNTs individually dispersed in 1 % SDS-water.

### 1.2.3. Carbon nanotube excitons

The VHSs of SWCNTs provide a connection between optical transitions and molecular structures with a single particle excitation model<sup>13, 15</sup>. However, their optical properties cannot be fully explained by the one electron-excitation approximation model because of all influence of electron-electron (e-e) interaction and exciton properties<sup>14</sup>. In reality, the spectral PL properties should be determined by the population with  $N$  interacting pairs to one with  $N-1$  pairs, including the e-e interaction or many-body system rather than recombination of a single e-h pair. This issue was brought into the great attention due to the experimentally observed “ratio problem”<sup>15, 16</sup>. The theoretical calculations neglecting electron-electron interaction expect that the ratio of  $E_{22}/E_{11}$  equals 2 within the simplest tight binding model. In the single particle model, diameter dependent curvature effects can cause this ratio to deviate from 2, while large diameters should eliminate such distortion and restore the ratio to 2. However, in experimental results, the ratio approaches 1.7 - 1.8<sup>13, 15</sup>. Kane *et al.* explained the ratio problem with the electron-hole states and subband electronic transitions in carbon nanotubes<sup>16</sup>. The experimental results using two photo excitation spectroscopy by Wang *et al.*<sup>6</sup> unambiguously explained the existence of subbands and the excitonic nature of the low energy transitions below optically active states.

The excitonic states of semiconducting SWNTs are complicated because of the existence of subband structures, indicating “dark” excitonic states (optically forbidden states) below the “bright” excitons, (optically allowed states)<sup>17, 18</sup>. A number of subbands arise from two degenerate valleys ( $K$  and  $K'$ ) in momentum

space with electron and hole spins<sup>14, 19</sup>. Intervalley mixing and singlet-triplet splitting are caused by short-range Columbic interaction, resulting in 16 different states including four singlet and twelve triplet states (Fig. 1-8). Only one of four singlet states is predicted to be an optically active bright state, whereas all others are optically forbidden dark states.

Dark excitonic states have been studied and their energetic positions calculated at low temperatures or under strong magnetic fields. Low temperatures, such as 4 – 6 K, enhance direct monitoring of dark states due to the increased radiative lifetime for a single 1D exciton with a parabolic dispersion. The radiative lifetime ( $\tau_r$ ) in a defect-free 1D system is known to vary as  $1/T^2$ <sup>17, 20</sup>. A strong magnetic field can induce the splitting of bright and dark excitonic levels to enhance the effect from dark states. The combination of magnetic and temperature studies can provide more information of energy splitting patterns on nanomaterials<sup>17, 19</sup>. For instance, two degenerate dark singlets have been studied at low temperatures. They are known to be located about 36 meV above the bright singlet for (6,5)-SWCNTs<sup>19</sup> and are referred as  $K$ -momentum singlet dark excitons ( $E_K$ ) because they have center-of-mass momenta near the graphite  $K$  and  $K'$  symmetry points. They are experimentally observed as phonon sidebands at lower emission energy than  $E_{11}$  in photoluminescence and interpreted as strong coupling between excitons and  $K$ -point phonons<sup>21</sup>. In the lowest spin singlet dark states, sidebands appears only a few meV below the bright singlet for SWCNTs ( $d = 1 - 1.3$  nm)<sup>17, 22</sup>. This state cannot be detected in the absence of a high magnetic field to split the energy levels, or at ambient temperatures<sup>22</sup>. For the triplet dark excitons, energetic states

are generally believed to be lower than that of bright exciton. It is difficult to directly measure triplet states because of optically forbidden pathways except if the enhanced spin orbit coupling induces spin flipping before recombination of electron-hole<sup>23,24</sup>. There are two reported experimental observations of triplet states including the triplet-involved photocurrent with Eu-S coated SWCNTs<sup>23</sup> or the pump-probe and spin-sensitive photoluminescence<sup>24</sup>.

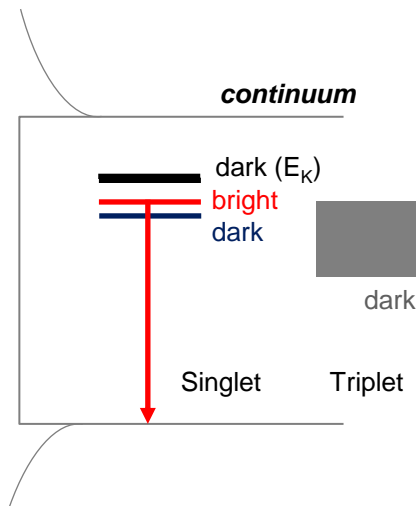


**Figure 1-8.** Excitonic states of SWCNTs. 16 different exciton states of SWCNT including 4 singlets and 12 triplets where only the exciton from bright singlet state can radioactively recombine.

Dark states are one of the crucial factors limiting the quantum yield (QY) to 0.1 %–7 % of photoluminescence QY for single isolated CNTs<sup>15, 26, 27</sup>. The SWCNT fluorescence QY is extremely low compared to other nanomaterials, such as quantum dots or organic dyes<sup>28</sup>. In SWCNTs, many excitons created by light

absorption undergo scattering into dark states as the exciton population approaches thermal equilibrium. Additional extrinsic factors also decrease and quench photoluminescence, such as the presence of metallic tubes, exciton-exciton transfer between mixed chiralities ( $< 0.05\%$  of QY)<sup>29</sup>, bundling of tubes, solvent effects or defects. Recent studies involving higher quality sorted samples, in which undesired species are removed, have reduced extrinsic factors for low QY. Intrinsic factors still limit the optical study of SWCNTs. Therefore, understanding and controlling exciton states including dark states are important to enhance fluorescence QY toward advanced applications in carbon nanotube-based material engineering.

#### 1.2.4. Defect induced photoluminescence

Photoexcited exciton dynamics are strongly affected by defects, either intrinsic or intentionally introduced<sup>30</sup>. Wang *et al.* found that defects are the most important factors affecting fluorescence QY, rather than inherent weakness of non-radiative decay channels<sup>30</sup>. The radiative lifetime of excitons in SWCNTs is 110 ns, which is relatively rapid compared to optically forbidden non-radiative decay. However, this transition time exceeds the lifetime of many other molecules, indicating a large portion of carbon nanotube excitons can be localized and subsequently quenched to non-radiative pathway at a defect site. For this reason, defects in SWCNTs are generally considered undesirable and are responsible for low quantum yield. Lee *et al.* reported the transient passivation of defects to increase QY through the addition of reducing agents to DNA-wrapped pristine SWNTs in aqueous solutions, supporting existing defect sites as an exciton

quencher<sup>31</sup>. Surprisingly, the presence of defects can bring a number of benefits, including introduction of anchor points for chemical functional groups, charge injection, and symmetry breaking effects, thus facilitating spectroscopic characterization in semiconducting materials<sup>25, 32-34</sup>. The controlled utilization of defects opens possible new directions toward optimization and modulation of optical and electronic properties.

Defects induced by intentional dopants lead to a new satellite PL peak in SWCNTs<sup>33</sup>. The new satellite PL peak appears at 10 – 15 % longer wavelengths in oxygen doped SWCNTs, and are distinct from phonon-sidebands<sup>33</sup>. This was explained by exciton diffusion along carbon nanotubes, followed by recombination at oxygen-doped sites. The structure of oxygen-doped SWCNTs are suggested to coexist in two forms, ether and epoxide<sup>35</sup>, where the ether form is thermodynamically favorable, and 20 kcal/mol more stable than the epoxide structure on the basis of PM3 calculations<sup>33</sup>. Oxygen-doped SWCNTs have been proposed for *in vivo* bioimaging due to their emission in the second near-infrared (NIR-II) window, where deep-tissue penetration is possible and autoscattering from tissues is minimized.

This new feature is further elucidated by Zhang *et al.*<sup>34</sup> in the Wang Lab through alkyl functionalized SWCNTs by Billups Birch Reduction<sup>36</sup>. Individually dispersed SWCNTs react with alkyl halide precursors to yield alkylated SWCNTs in Na-NH<sub>3</sub> solution at -78 °C and then the solid *f*-SWCNTs as a product are dispersed in sodium dodecyl sulfate (SDS)-water for optical measurements. The *f*-SWCNTs show the propagative mode of alkylation around an initial defective spot

that promotes subsequent addition next to the first functional group. The  $sp^3$  functional band structure is identified by scanning electron microscopy (SEM) operated by low electron beam of 1 kV, clearly showing contrast between intact regions and functional bands due to increased yield of secondary electrons at the functional band region<sup>37</sup>. However, the sidewall reaction with the Billups Birch alkylation is limited in only alkyl groups excluding aryl groups and other alkyl groups like perfluorinated groups because of low reactivity for  $S_N2$  type reactions. The harsh conditions in liquid ammonia at low temperature require extra steps including filtration and re-dispersion, which makes it impossible to monitor the reaction *in situ*.

Piao *et al.* reported the new, bright photoluminescence through  $sp^3$  defects with aryl diazonium salts<sup>25</sup>. This method induces extremely bright photoluminescence up to 8-fold for (6,5)-SWCNTs and 28-fold for (6,4)-SWCNTs through dark exciton brightening. The attachment of strong electron-withdrawing substituents (e.g. nitro group,  $-NO_2$ ) to carbon nanotubes further pushes down the energy levels at a defect, creating the first path to harness low-lying dark excitons. However, the reaction rate of this diazonium chemistry is low and typically takes 240 h to complete the defect planting reaction. Furthermore, the process is limited to aryl groups and cannot be extended to alkyl diazoniums and activated aryl diazoniums due to instability of reagents and high reduction potentials. A more versatile defect chemistry that allows incorporation of various aryl/alkyl groups and even divalent groups at aqueous phase will significantly broaden exciton engineering by defects.

### 1.3. Charged excitons in semiconducting materials

#### 1.3.1. Formation of charged excitons in nanomaterials

Charge carriers are of considerable interest to explore optical and electronic properties in semiconductors<sup>38, 39</sup>. In intrinsic un-doped semiconductors, the concentration of both carriers including electron and hole are ideally the same. In carrier-doped semiconducting materials, excess charge carriers can lead to stable bound states of exciton-carriers, called “trions”, with noticeable consolidation of three particles clamped together<sup>40</sup>. For hole-doped systems, positive trions form, consisting of two holes and an electron ( $h$ - $e$ - $h$ ,  $X^+$ ), whereas in negatively doped systems, negative trions form, consisting of two electrons and a hole ( $e$ - $h$ - $e$ ,  $X^-$ ) (Fig. 1-9).

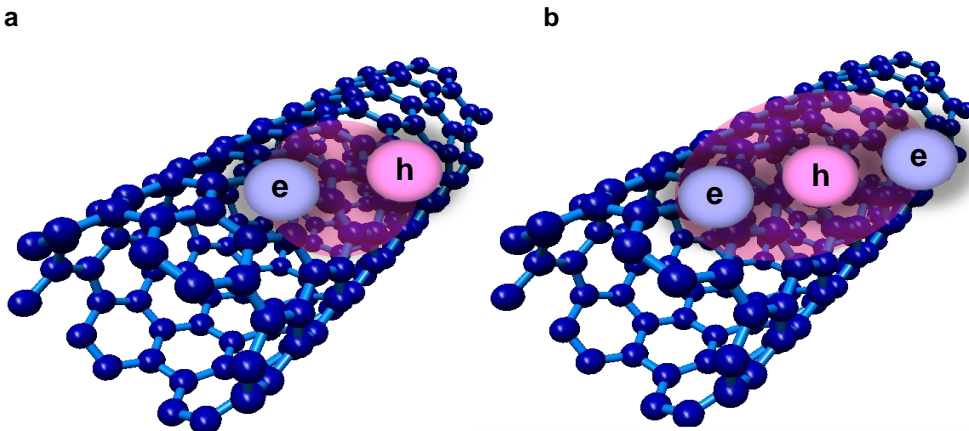


**Figure 1-9.** Schematic view of an exciton and a trion. **a**, An electron (blue)-hole (red) pair, exciton, in a undoped SWCNT. **b**, A negatively charged exciton – the bound state of a hole and two electrons in a SWCNT.

Like an exciton, the semiconductor analog of atomic hydrogen, trions have further analogs with hydrogen ions namely  $H^-$  and  $H_2^+$ . The concept of trion was first introduced by Lampert in 1958<sup>42</sup>, but had not been identified in bulk materials because of the negligible binding energy of three particles in 3D materials. After several decades, - trion were first experimentally observed in low-dimensional materials such as quantum wells (QWs)<sup>38, 40, 43</sup>, quantum dots (QDs)<sup>39</sup> and carbon nanotubes (CNTs)<sup>44-46</sup>. Control of carrier density in low-dimensional materials is one of the most effective methods to modulate an extensive range of interesting optical properties through a many-body bound state. Therefore, trions in low-dimensional materials are attracting increasing attention for fundamental photophysics of spin manipulation and device applications such as single-spin devices in the area of quantum information, single-dopant transistors, and bioapplications<sup>47, 48</sup>.

### 1.3.2. Optical properties of trions in semiconductors

Trions in various semiconductors have been investigated under magnetic fields, and different carrier densities, excitation energy densities or temperatures to understand their dynamics<sup>49-54</sup>. Research reveals that trions and excessive charges are localized at defect traps<sup>53</sup>. Trions also interact strongly with triplet states, exhibiting quantum behavior. For examples, *p*-doped CdTe/Cd<sub>1-x</sub>yMg<sub>x</sub>Zn<sub>y</sub>Te QWs shows the localized trions ( $X^+$ ) in the near-field PL at low temperature, 5 K<sup>53</sup>. Strongly reduced scattering efficiency of quasiparticles, compared to free excitons, account for this behavior. Cox *et al.* develops the trion in organic semiconductors<sup>54</sup>,

created by high photo-carrier density. This organic semiconducting trion is localized at deep trap sites and is formed by mixing spin states from triplet exciton-polaron effects<sup>54</sup>. The increased trion life time with magnetic fields further supports the spin-dependent formation of triplet excitons at trap sites and their subsequent spin selective assembly into metastable trions. Trion formation will provide new insights to excitonic states, spin states, and defect-incorporated effects.

### 1.3.3. Trions in carbon nanotubes

In semiconducting carbon nanotubes, trions are detectable even at room temperature without external high magnetic fields due to limited screening and highly enhanced binding energy of excitons in quasi 1D structures<sup>44-46, 55</sup>. Several methods are reported for experimental observation of carbon nanotube trions: hole doping<sup>44, 52, 55</sup>, high power density<sup>45</sup>, and electrical methods<sup>46, 56</sup>. The hole doping methods reported the first experimentally observed positive trions in SWCNTs, using 2,3,5,6-tetrafluoro-7,7,8,8-tetracyanoquinodimethane (N<sub>4</sub>TCNQ) as a hole dopant. The *p*-type trion of SWCNTs shows a large energy separation (100 – 200 meV) from a bright exciton state. The electron-hole exchange interaction originates from the short-range Coulomb interaction<sup>44, 52</sup>. All-optical method involving high power densities (> 1 kW/cm<sup>2</sup>) were also used to generate trions<sup>45</sup>. Santos *et al.* suggested that electrons and holes are localized to avoid their spatial overlap, followed by exciton annihilation process to generate dissociated carriers<sup>45</sup>. A subsequent photon absorption event and the dissociated charge carrier caused the formation of either a positive or a negative trion. Lastly, Park *et al.*

electrochemically generated both positive and negative trions with isolated SWCNT-indium tin oxide (ITO) films<sup>46</sup>. A common binding energy for the negative and the positive trions was attributed to identical effective masses of holes and electrons. Although all methods illustrate the creation of trions, the PL intensity is far below those of excitons.

Recently, Brozena *et al.* in the Wang Lab reported defect-bound trion PL ( $E_T$ ) in functionalized SWCNTs<sup>57</sup>. In these systems, trion PL is nearly as bright as that of pristine excitons ( $E_{11}$ ). The separation energy is 260 meV for 5-carboxylic hexyl group functionalized (6,5)-SWCNTs, which is 80 meV larger than trions in pristine (6,5)-SWCNT due to the localization at defects. The defects and charges are created by Billups Birch alkylation with doping from excessive amount of sodium metal in liquid ammonia or by arylation using *in situ* diazonium reaction in sulfuric acid for hole-doping. The doped *f*-SWCNTs are re-dispersed in surfactant-solutions for optical measurement of trion PL.

Further studies are required to illuminate the properties of defect bound trions, such as *in situ* profiles of defect photoluminescence evolution with high concentration of trions, trion response as a function of controlled defect density, and comparison of defect-trapped trion PL ( $E_T$ ) to defect-trapped exciton PL ( $E_{11}^-$ ). Moreover, the bright (optically allowed) trion with the lowest energy is suggested as a bound state of a dark (optically forbidden) exciton with spin 3/2 and an extra electron or hole by means of the exact diagonalization of the realistic Hamiltonian and the screened Hartree-Fock approximation. This indicates triplet-dark exciton associated trions<sup>58</sup>. Experimental evidence of such predicted triplet trions is still

lacking. Defect-bound trions in carbon nanotubes can thus further reveal complicated triplet dark states and many-body correlations in low-dimensional structures.

#### **1.4. Preparation of high purity semiconducting carbon nanotubes**

Samples with population of identical chirality tubes is the essential requirement for comprehensible study on excitons. Pure single chirality hasn't been achieved by current synthetic methods until now, while several purification methods have developed to provide high purity of single chirality-enriched samples<sup>59-61</sup>. Zheng *et al.* demonstrated high purity SWCNTs separation with aid of short DNA sequences that recognize particular nanotube species<sup>59</sup>. More than 12 semiconducting carbon nanotubes were isolated from the synthetic mixture of SWCNTs.

Despite such powerful separation methods, SWCNT separation still suffers from problems such as low yields and high cost. Liu *et al.* developed a scalable separation with gel chromatography, which is efficient and more affordable<sup>60</sup>. Chirality-selective interactions with agarose gels successfully isolate 13 single chiralities of semiconducting tubes providing unique optical spectra and solution colors, depending on their electronic structure. Most of the metallic tubes and remaining catalysts from nanotube synthesis are removed by gel chromatography. This method provides a high purity of (6,5)-SWCNTs as a major product, while a few other chiralities also are isolated with relatively high purities.

Recently, Ao *et al.* developed an advanced separation technique by using aqueous two phases (ATP) formed by the addition of polyethylene glycol (PEG) and polyacrylamide (PAM)<sup>61, 62</sup>. A proper DNA sequence with polymers in aqueous two-phase system effectively modulates the partition to separate as many as 15 single-chirality nanotube species from a synthetic mixture, resulting in a highly simple, fast and scalable method with resulting high purity. While the gel chromatography method is mainly used for isolating single chirality tubes in this thesis work, the ATP method is also used to rule out effects or potential impurities coming from purification methods.

### **1.5. Overview of thesis work**

Excitons and defects in nanomaterials have received great attention because they not only influence optical and electrical properties, but also play an important role in nano-devices. The controlled utilization of defects unexpectedly brings many benefits including symmetry breaking effects, exciton engineering, and charge carrier localization. Therefore, developing new strategies to control excitonic states and defects is highly desirable. In this thesis, fluorescent quantum defects in carbon nanotubes will be introduced and discussed in depth. Chapter 2 explores the understanding of exciton engineering in semiconducting carbon nanotubes through new defect chemistry based on alkyl/aryl halides. These well-controlled versatile functional groups and their electronic effects at defects will be revealed. Chapter 3 presents optical probing of pH and temperature in complex fluids through defect photoluminescence in SWCNTs. In Chapter 4, brightening of

carbon nanotube trions through fluorescent quantum defects will be illustrated. Lastly, Chapter 5 summarizes the tunable fluorescence quantum defects and discusses current challenges and possible research directions.

## Chapter 2 . Molecularly Tunable Fluorescent Quantum Defects

*Adapted from H. Kwon, A. Furmanchuk, M. Kim, B. Meany, Y. Guo, G. C. Schatz, Y. H. Wang. 2016. (submitted). Y.H.W. and H.K. conceived and designed the experiments. H.K., M.K., and B.M. performed experiments. A.F and G.C.S performed DFT calculations. Y.H.W. and H.K. wrote the manuscript with inputs from all co-authors.*

### 2.1. Introduction

The excited states of many semiconducting nanocrystals and polymers are characterized by excitons, electron-hole pairs bound by Coulomb interactions<sup>3</sup>. Excitons are hydrogen-atom-like quasi-particles, each carrying a quantum of electronic excitation energy. An exciton can return to the ground state by emitting a photon, producing photoluminescence (PL), or by falling into a “dark” state from which the energy is lost as heat. The ability to control the fate of excitons and their energy is crucial to imaging<sup>63, 64</sup>, sensing<sup>65</sup>, photovoltaics<sup>66</sup>, lighting and display<sup>67</sup>, and many other important electronic functions.

Over the last few decades, two major classes of approaches, quantum confinement and doping, have been developed to tailor the exciton properties within a nanocrystal. This quantum confinement effect has motivated the development of many innovative synthetic approaches that control the size and shape of nanocrystals, and consequently their electronic and optical properties<sup>68-70</sup>. Examples include nitrogen-vacancy in diamond<sup>71</sup> and metal ion-doped nanocrystals<sup>72</sup>.

In the case of single-walled carbon nanotubes (SWCNTs), the excitonic

properties depend on both the diameter and chiral angle of each nanotube crystal, collectively known as chirality, which can be denoted by a pair of integers  $(n,m)$ <sup>13</sup>. Recent work by us<sup>25</sup> and others<sup>33</sup> has demonstrated that the optical properties of SWCNTs can also be modified by doping with oxygen<sup>33</sup> or incorporation of  $sp^3$  defects<sup>25</sup> through diazonium chemistry. These defects can induce a new near-infrared emission<sup>33</sup>, brighten dark excitons<sup>25</sup>, facilitate up conversion(anti-stoke shift)<sup>73</sup>, and stabilize trions at room temperature<sup>57</sup>, making them particularly interesting for emergent photonic application. However, both methods for defect creations have thus far bound by the extremely limited chemical and optical tunability. Particularly, oxygen doping leads to mixed ether and epoxide structures, and diazonium chemistry works only for specific aryl groups and monovalent bonding, and has low reaction rates. For these reasons, examples of this type of defects are pale in comparison with the large number of quantum dots that have been synthesized based on the quantum confinement effect. Although it has been suggested, the prospect of using defects for materials engineering has not been demonstrated.

In this chapter, we describe a new synthetic approach for tailoring excitons within a single material through molecular engineering of covalently attached surface functional groups (Fig. 2-1). We illustrate this new approach through the synthesis of more than 30 new fluorescent nanostructures from SWCNTs of the same crystal structure by creating molecularly tunable fluorescent quantum defects in the  $sp^2$  carbon lattice. Each of the new synthetic nanostructures may be viewed as a diamond-in-graphene structure reminiscent of an island in an electron sea.

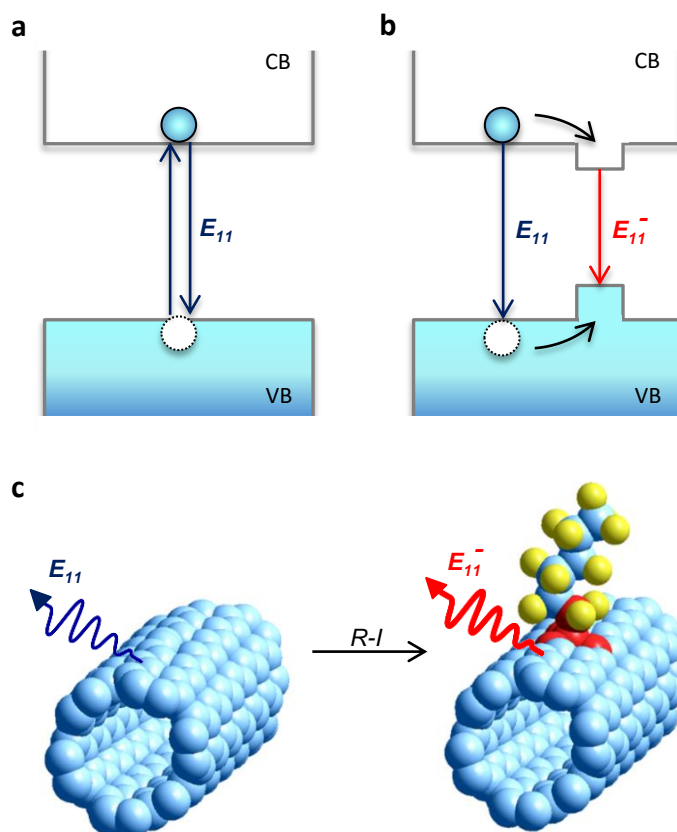


**Figure 2-1.** The fluorescent quantum defect approach to material engineering. **a**, In a quantum confinement system, the exciton wavefunction is confined as the particle size reaches the Bohr radius of the quasi-particle, lending the capability to control optical properties by size engineering. **b**, In the proposed quantum defect systems, the mobile excitons can be trapped and their optical properties can be controlled by molecular engineering of the trap. **c**, The creation of a fluorescent quantum defect by reacting a SWCNT semiconductor with different types of alkyl iodides (R-I).

More specifically, in the case of semiconducting nanotubes, these structures can be viewed as hybrid quantum systems that allow excitation energy (carried by the exciton) to be channeled along a one-dimensional (1D) antenna and then harvested using a zero-dimensional (0D) funnel. Compared with quantum confinement,

which controls the optical and electronic gap by size engineering, these fluorescent defects in SWCNTs create local potential wells that can be chemically tailored with molecular-control as shown herein. To recognize their molecular nature and the fact that the local potential well is a result of defect-induced splitting of frontier orbitals, we propose to call these fluorescent quantum defects. Furthermore, unlike atomic color-center dopants, our defect-inducing surface functional groups are themselves non-emitting and readily accessible chemically, thereby affording unprecedented molecular control and engineering flexibility.

## **2.2. Experimental and theoretical calculation methods**

### 2.2.1. Aqueous dispersions of individual SWCNT crystals

SWCNTs (HiPco batch # 194.3 (Rice University; or CoMoCAT SG65i Lot # 000-0036, SouthWest NanoTechnologies, Inc.) were stabilized by 1 wt.% sodium dodecyl sulfate (Sigma Aldrich,  $\geq 98.5\%$ ) in deuterium oxide ( $D_2O$ , Cambridge Isotope Laboratories, Inc., 99.8%) by tip ultrasonication (Misonix) at 35 W, 10 °C in a stainless steel beaker for 2 hours, followed by ultracentrifugation with an Optima LE-80K Ultracentrifuge (Beckman Coulter) at 170,499g for 2 hours to remove bundled nanotubes and residual catalysts. The individually dispersed SWCNTs were sorted for high purity (6,5)-SWCNTs using gel chromatography<sup>60</sup>. The samples were diluted to an optical density of 0.1 at the  $E_{11}$  absorption peak of (6,5)-SWCNTs in 1 wt.% SDS in  $D_2O$ . The concentrations of HiPco and CoMoCAT were determined with a calibration curve from correlated optical density and thermogravimetric analysis. The concentration of chirality-enriched

solutions was calculated based on the extinction coefficient previously determined by Zheng *et al.*<sup>74</sup>

### 2.2.2. Synthetic creation of fluorescent quantum defects in SWCNTs

Sodium bicarbonate (EMP Chemicals, ACS grade), acetonitrile (Signal Aldrich, 99.9%) and alkyl halides were added sequentially to each SWCNT solution, which was kept in a capped glass vial covered by aluminum foil. Acetonitrile was used as a co-solvent for the alkyl halide. Sodium dithionite (Sigma Aldrich, 85%) was then added to the mixture and stirred with a magnetic stir bar at room temperature. For aryl defects, only aryl-containing iodides are required and the reaction was triggered by optically exciting the E<sub>22</sub> transition of the nanotubes for single valent groups. For the divalent aryl groups, 300-800 nm excitation was required to develop a defect PL. The degree of functionalization was controlled by adjusting the relative amounts of reagents. The reaction was monitored at various times by UV-Vis-NIR absorption and fluorescence spectroscopy.

### 2.2.3. *In situ* UV-Vis-NIR absorption and photoluminescence spectroscopy

The reactions were monitored *in situ* using a Lambda 1050 UV-Vis-NIR spectrophotometer (Perkin Elmer), which is equipped with both a PMT detector and an extended InGaAs detector, and a NanoLog spectrofluorometer (Horiba Jobin Yvon). For fluorescence spectroscopy, the samples were excited with a 450 W Xenon source dispersed by a double-grating monochromator. Excitation-emission

maps and fluorescence spectra were collected using a liquid-N<sub>2</sub> cooled linear InGaAs array detector on a 320 mm imaging spectrometer. The spectrofluorometer was calibrated against NIR emission lines of a pencil-style neon spectral calibration lamp (Newport).

#### 2.2.4. Resonant Raman scattering and X-ray photoelectron spectroscopy

The SWCNTs were precipitated out from solutions and deposited on glass slides for Raman scattering or gold-coated silicon substrates for XPS measurement. XPS was taken with Kratos Axis 165 at 25 °C and 175 °C under an ultrahigh vacuum ( $< 1 \times 10^{-8}$  Torr). Raman spectra were measured on a LabRAM ARAMIS Raman microscope (Horiba Scientific). The samples were excited with a He-Ne (632.8 nm) laser or a 532 nm laser at a power density of 0.014-0.14 mW  $\mu\text{m}^{-2}$ . Each spectrum was obtained by averaging the data collected from three different spots. Absorption and PL spectra were fitted with Voigt functions using PeakFit software v4.12. No baseline correction was applied during the fitting for PL while a linear background correction was used for the E<sub>22</sub> absorption.

#### 2.2.5. Theoretical calculation methods of fluorescent quantum defects

The inductive constant was calculated using equations described by Cherkasov *et al.*<sup>75</sup>. The structure of alkyl functionalized (6,5)-SWCNTs was constructed using Nanotube Modeler (JCrystalSoft) and HyperChem 8.0 (Hypercube, Inc). The distance between two atoms and the covalent radius (half of

the bond length) was obtained from molecular structures optimized by Molecular Mechanics.

For the density functional theory calculations, the geometries of an 8 nm (2 unit cells) long (6,5)-SWCNT with various quantum defects were optimized using the B3LYP functional in Q-Chem 4. The nanotube ends are terminated with hydrogen atoms to minimize end-effects and to avoid introduction of edge states into the band gap of the nanotube. Most calculations considered two alkyl groups (to avoid radical character) covalently attached near the center of the 8 nm nanotube, although single, triple and higher functionalization were also considered. The DFT level of theory with a 6-31G\* basis set was used for minimization. A Mulliken analysis was performed to reveal the charge distribution around the created defects.

### **2.3. Results and discussion**

#### 2.3.1. Creation of alkylated fluorescent quantum defects

Our starting material is (6,5)-SWCNTs that are approximately 0.75 nm in diameter and 500 nm in length (or 125 unit cells) on average. The nanotubes are sorted using gel chromatography<sup>60</sup> to a high level of optical purity and stabilized as individual particles in water or deuterium oxide (D<sub>2</sub>O) by 1 wt.% sodium dodecyl sulfate (SDS). Note that our chemistry readily extends to other nanotube chiralities; (6,5)-SWCNT is chosen for this study due to its synthetic abundance and better established literature.

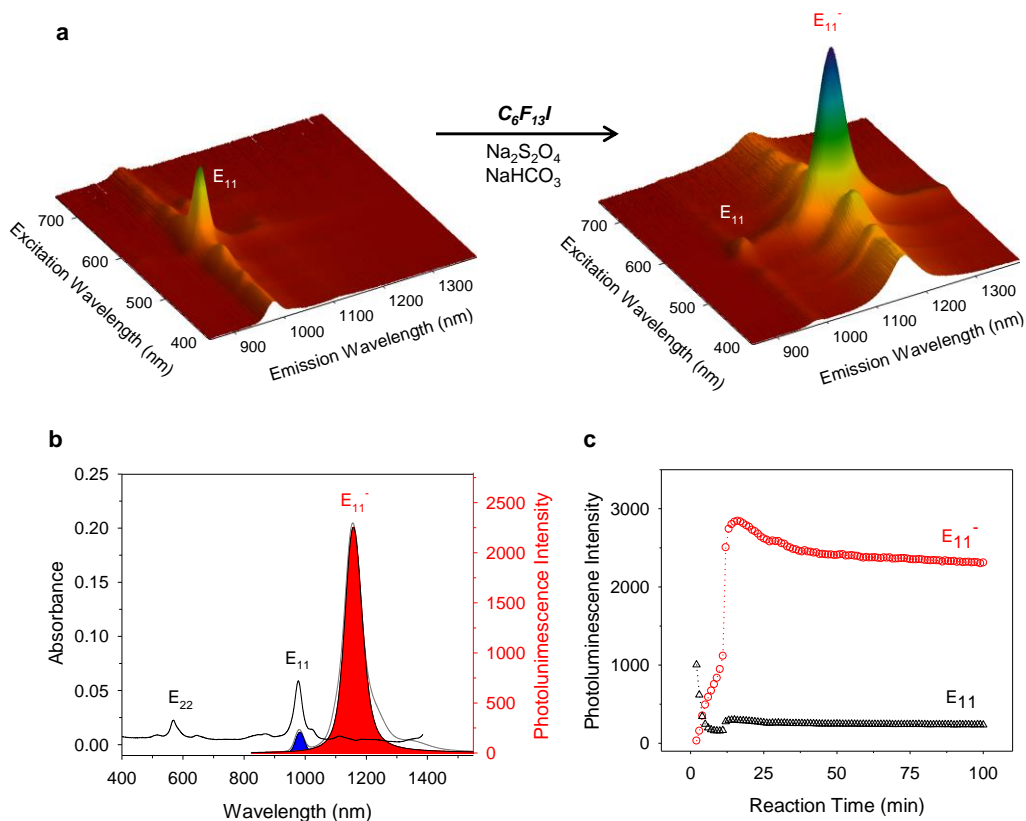


**Figure 2-2.** Chemical creation of fluorescent (6,5)-SWCNT-CF<sub>2</sub>(CF<sub>2</sub>)<sub>4</sub>CF<sub>3</sub>. **a**, Defect photoluminescence arises farther in the near-infrared, 190 meV to the red of the parent nanotube excitonic emission. **b**, Correlated visible near-infrared absorption (black line) and PL (red line) spectra for (6,5)-SWCNT-CF<sub>2</sub>(CF<sub>2</sub>)<sub>4</sub>CF<sub>3</sub>. The SWCNTs are excited at the E<sub>22</sub> transition (565 nm). **c**, Evolution of E<sub>11</sub> and E<sub>11</sub><sup>-</sup> emission.

The (6,5)-SWCNTs have intrinsic absorption and photoluminescence peaks at 979 nm (E<sub>11</sub>) and 568 nm (E<sub>22</sub>), which arise from their excitonic transitions (Fig. 2-2)<sup>15</sup>. Covalent attachment of perfluorinated hexyl groups to the nanotubes produces a bright defect PL peak (E<sub>11</sub><sup>-</sup>) at 1155 nm. The observed peak is redshifted from the parent nanotube PL (E<sub>11</sub>) by 177 nm ( $\Delta E = 190$  meV), and the full width at half-maximum (FWHM) of the peak increases from 37 meV to 69 meV. This

new feature arises within minutes of the start of the reaction, and reaches the maximum after 12 minutes and then plateaus in 25 minutes. The bright feature remains stable over at least nine months under ambient conditions (Fig. 2-2c).

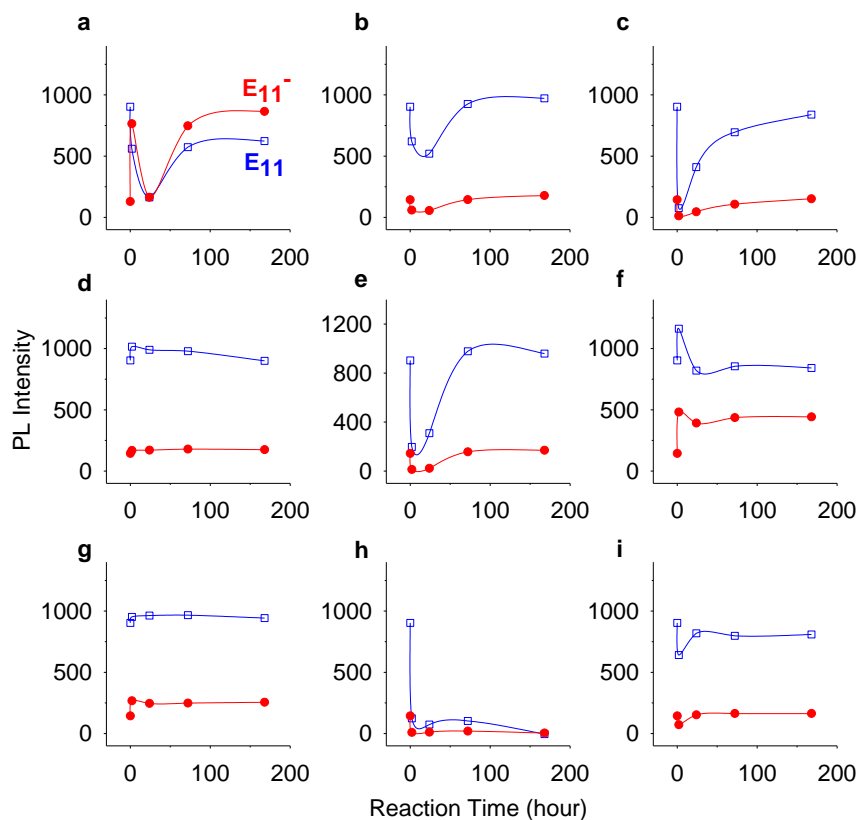


**Figure 2-3.** Control reactions with different reagent conditions. Emission spectra are monitored with 565 nm excitation at 0 h, 2 h, 24 h, 3 days and 7 days. Only the reaction condition (a) shows the strong defect PL ( $E_{11}^-$ ).

**Table 2-1.** Control reactions with different reagent conditions.

Reaction	SWCNT	CH <sub>3</sub> CN	C <sub>6</sub> F <sub>13</sub> I	NaHCO <sub>3</sub>	Na <sub>2</sub> S <sub>2</sub> O <sub>4</sub>	E <sub>11</sub> <sup>-</sup>
a	1	0.2	10	20	10	strong
b	1	0.2	-	-	-	-
c	1	-	10	-	-	-
d	1	-	-	20	-	-
e	1	-	-	-	10	-
f	1	-	10	20	10	Weak
g	1	0.2	-	20	10	-
h	1	0.2	10	-	10	-
i	1	0.2	10	20	-	-

We have developed the new exciton-tailoring reaction that occurs in aqueous solution upon mixing an alkyl halide with nanotubes in the presence of the mild reductant sodium dithionite for the first time (Fig. 2-3). Alkyl halides alone cannot generate alkyl radicals that covalently attach to the carbon lattice (Fig. 2-3c and 2-3i). Control experiments suggest that the reaction is facilitated by acetonitrile, which acts as a co-solvent for the alkyl halides, not required to generate defect photoluminescence (Fig. 2-3b and 2-3f). Sodium bicarbonate serves as a base to balance acidic byproducts of sodium dithionite (Fig. 2-3d and 2-h) as explained with organic small molecules<sup>76, 77</sup>.

The PL of the alkylated carbon nanotubes shows a strong dependence on nanotube diameter,  $d$ , by  $\Delta E = A/d^2$  with  $A = 18.7 \text{ meV nm}^2$ , suggesting that the new emission peak arises from brightening of dark excitons (Fig. 2-4 and 2-5)<sup>25, 78</sup>. Notably, the (6,5)-SWCNT-(CF<sub>2</sub>)<sub>5</sub>CF<sub>3</sub> exhibits PL that is brighter than that of the parent nanotube by more than an order of magnitude (Fig. 2-6).

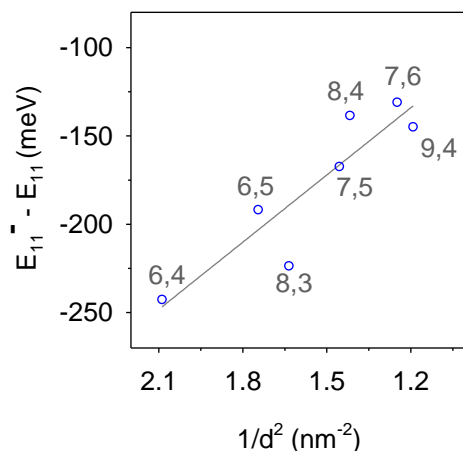


**Figure 2-4.** Emission energy of defect photoluminescence is dependent on the nanotube diameter. All chirality enriched carbon nanotube are used and functionalized with  $-C_6F_{13}$  groups.

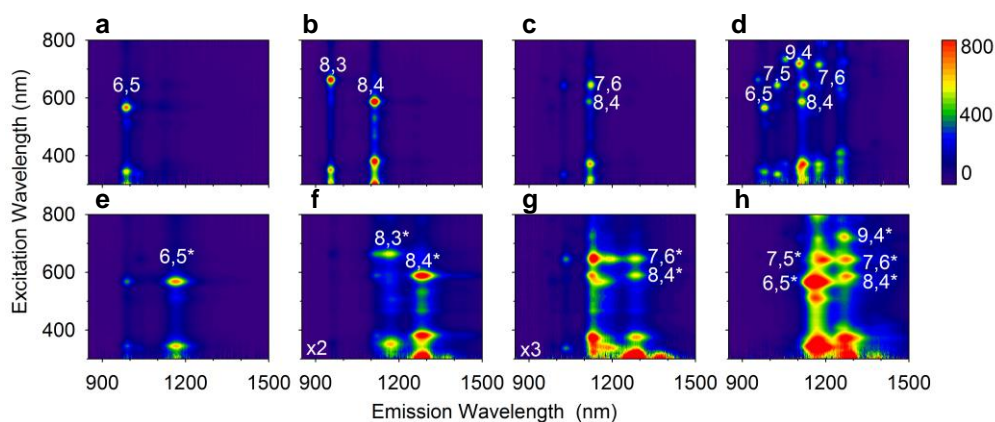


**Figure 2-5.** Nanotube structure-dependent defect photoluminescence. The excitation-emission maps of **a**, (6,5)-SWCNT; **b**, (8,3)- and (8,4)-SWCNT; **c**, (7,6)- and (8,4)-enriched SWCNTs; and **d**, the mixed chirality of HiPco. Controlled sidewall alkylation induces new PL peaks in **e**, (6,5)-SWCNT- $CF_2(CF_2)_4CF_3$ ; **f**, (8,3)/(8,4)-SWCNT- $CF_2(CF_2)_4CF_3$ ; **g**, (7,6)/(8,4)-SWCNT- $CF_2(CF_2)_4CF_3$ ; and **h**, HiPco-SWCNT- $CF_2(CF_2)_4CF_3$ . The nanotubes are stabilized in  $D_2O$  by 1 wt.% SDS.

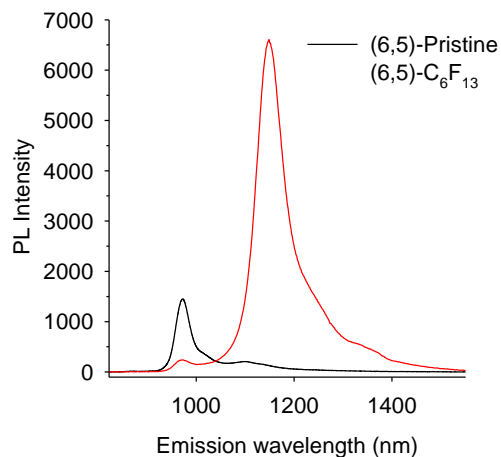


**Figure 2-6.** Emission spectra of (6,5)-pristine and (6,5)-SWCNT- $(\text{CF}_2)_5\text{CF}_3$  that show the brightening PL by more than an order of magnitude.

Correlated measurement of PL, Raman scattering, and X-ray photoelectron spectroscopy (XPS) unambiguously confirm that the new PL originates from  $sp^3$  quantum defects due to the covalent attachment of a small number of the alkyl groups to the  $sp^2$  carbon lattice (Fig. 2-7). The formation of a covalent C-C bond between the alkyl group and the carbon nanotube is evidenced by the rise of the symmetry-breaking, defect-induced Raman scattering of the D phonon ( $\sim 1,300 \text{ cm}^{-1}$ )<sup>79</sup>. The intensity of this Raman band with respect to the in-plane stretching mode ( $E_{2g}$ ) of the  $sp^2$  bonded carbon lattice (G band,  $\sim 1590 \text{ cm}^{-1}$ ) increases from 0.10 to 0.98 in highly functionalized nanotubes (Fig. 2-7a). Both the Raman D/G ratio and the XPS intensity of the perfluoroalkyl group increase in proportion to the relative concentration of alkyl halide (Fig. 2-7a, 2-7b and Fig. 2-9). High resolution

XPS of SWCNT-(CF<sub>2</sub>)<sub>5</sub>CF<sub>3</sub> shows the growth of the *sp*<sup>3</sup> C1s peak at 285 eV as a shoulder to the *sp*<sup>2</sup> C1s peak (284.7 eV), resulting in substantial peak broadening of the C1s peak (FWHM of 1.46 eV versus 0.83 eV for the starting nanotubes) (Fig. 2-8). The fluorine (F1s) signal of the functional group remains constant at high temperature (175 °C) in ultrahigh vacuum (< 1 × 10<sup>-8</sup> torr), in which there are no physisorbed molecules (Fig. 2-10).

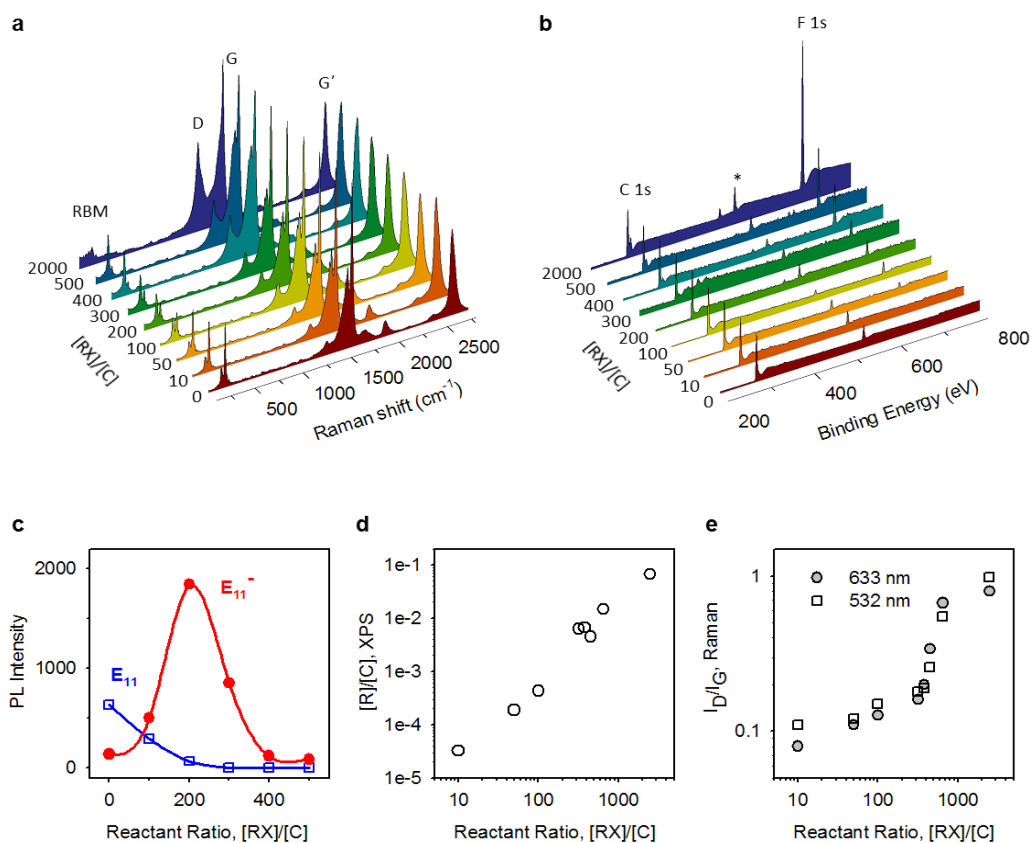


**Figure 2-7.** Correlated spectral characterization of functionalized SWCNTs at increasing molar reactant ratios of CF<sub>3</sub>(CF<sub>2</sub>)<sub>4</sub>CF<sub>2</sub>I (RX) to the mixed chirality of HiPco SWCNT carbon. **a**, Raman scattering. The excitation line is 532 nm. **b**, XPS (taken at 25 °C). The O1s peak is marked with an asterisk (\*). **c**, PL. **d**, The ratio of covalently attached function group to nanotube carbon, [R]/[C], as determined from XPS,

increases linearly with the reactant ratio,  $[RX]/[C]$ . **e**, Raman D/G ratio of SWCNT- $CF_2(CF_2)_4CF_3$  at increasing  $[RX]/[C]$ .

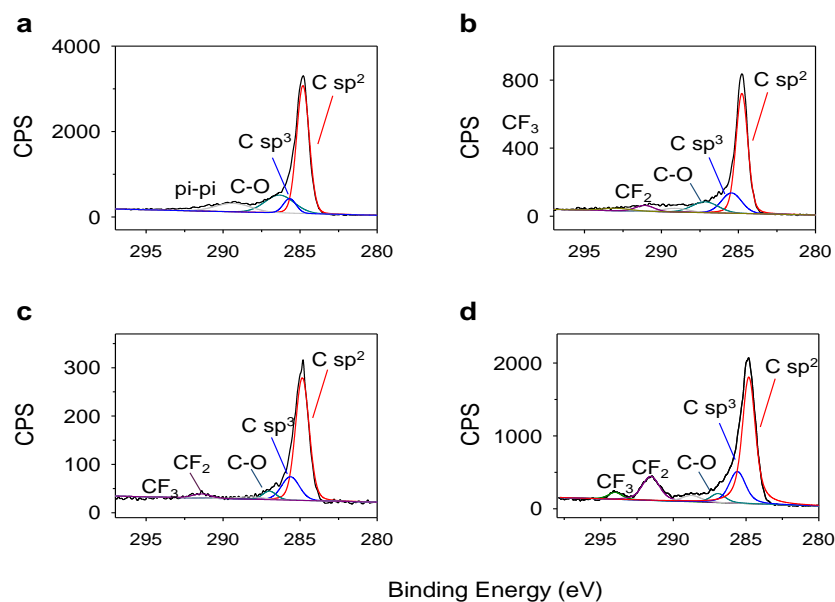


**Figure 2-8.** High resolution XPS of C 1s at 175 °C for SWCNT- $CF_2(CF_2)_4CF_3$ . **a**, Non-functionalized control. **b**,  $[C]:[RX] = 1:50$ . **c**, 1:500. **d**, 1:2500. The nanotubes used here are a sample of mixed chirality HiPco SWCNTs.

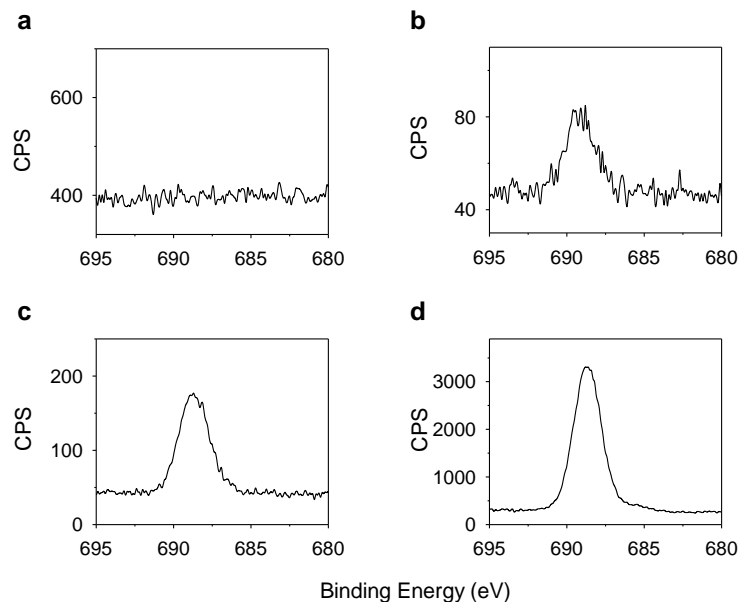


**Figure 2-9.** High resolution XPS of F 1s at 175 °C for SWCNT- $\text{CF}_2(\text{CF}_2)_4\text{CF}_3$ . **a**, Non-functionalized control. **b**, [C]:[RX] = 1:50, **c**, 1:500, and **d**, 1:2500.

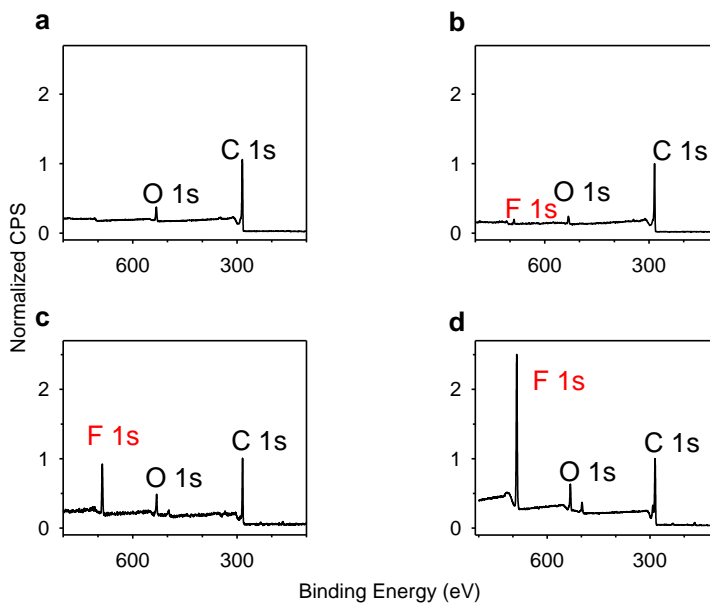


**Figure 2-10.** High resolution XPS of full spectra at 175 °C for SWCNT- $\text{CF}_2(\text{CF}_2)_4\text{CF}_3$ . **a**, Non-functionalized control. **b**, [C]:[RX] = 1:50, **c**, 1:500, and **d**, 1:2500.

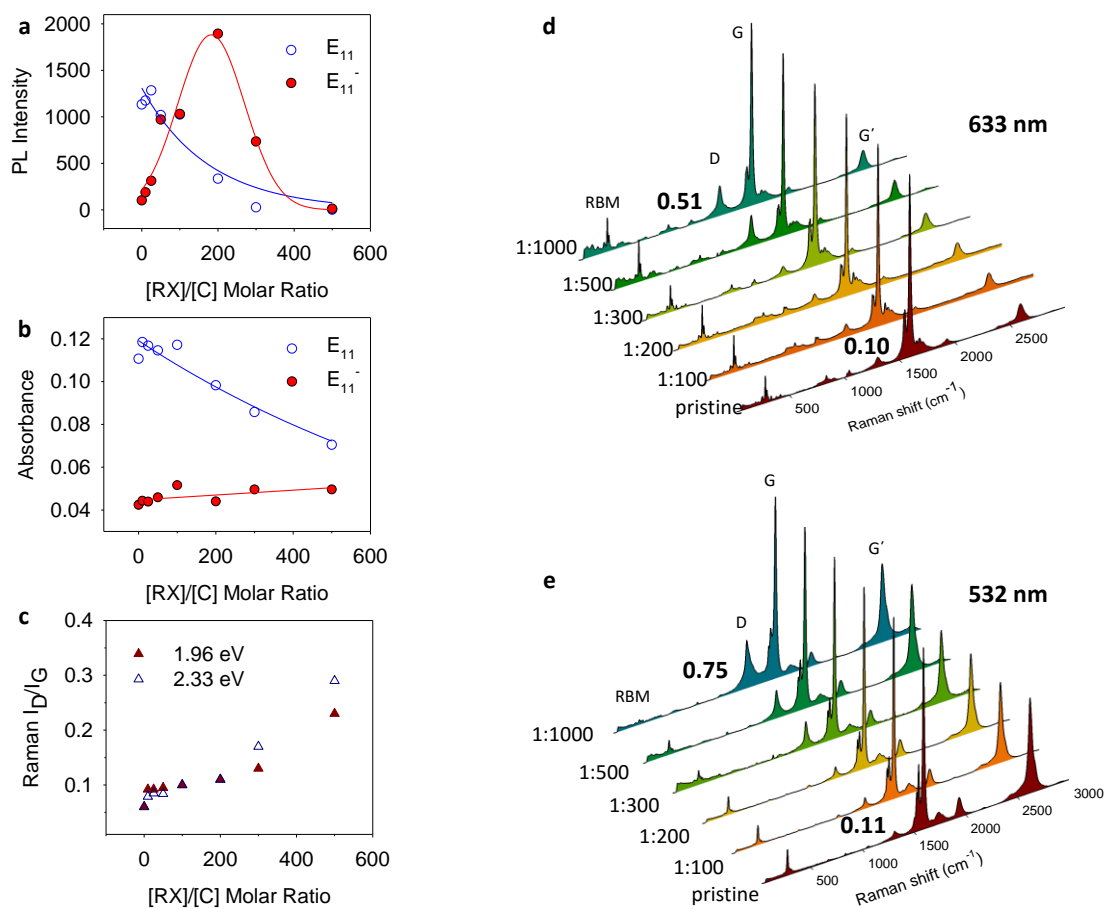


**Figure 2-11.** Correlated spectral characterization of *f*-CoMoCAT SWCNTs at increasing ratio of -C<sub>6</sub>F<sub>13</sub> groups. **a**, PL, **b**, absorption, and **c**, Raman D/G ratio as a function of [RX]/[C] molar ratio. Raman spectra with **d**, 632.8 nm and **e**, 532 nm excitation laser, respectively.

We further investigated the new defect PL with different SWCNT samples such as HiPco ensemble, CoMoCAT ensemble, the column-purified SWCNTs, and the aqueous two phase-assisted SWCNTs<sup>61</sup> to rule out the possibility of impurity effects (Fig. 2-5). They all show the consistent positions of defect PL for the (6,5) chirality tubes for all tested samples. Furthermore, the correlated emission,

absorption and Raman with (6,5)-CoMoCAT-(CF<sub>2</sub>)<sub>5</sub>CF<sub>3</sub> shows identical results of close relationship between covalent attachment and defect PL brightening (Fig. 2-11).

By changing the concentrations of the reagents, we are able to control the intensity of the defect PL. The E<sub>11</sub>' intensity of (6,5)-SWCNT-(CF<sub>2</sub>)<sub>5</sub>CF<sub>3</sub> peaks at a carbon-to-alkyl halide reactant molar ratio of 1 to 0.4 (Fig. 2-2). Correspondingly, the Raman D/G ratio increased from 0.10 to 0.18, indicating that a small amount of alkyl groups are covalently attached on the nanotubes. Consistent with Raman scattering, the visible near-infrared absorption barely decreased. Based on XPS (Fig. 2.7), we estimate that the attached -(CF<sub>2</sub>)<sub>5</sub>CF<sub>3</sub> groups are at a density of one group per 166 carbons or 1.8 nm of nanotube length on average. This density is much higher than that produced by diazonium salts<sup>25</sup> and may suggest distinct reaction propagation<sup>34</sup>.

### 2.3.2. Tunable fluorescent quantum defects with alkylation

This synthetic quantum system provides exceptional chemical tunability of the near-infrared PL energy (Fig. 2-12 and Fig. 2-14). We can continuously red-shift the E<sub>11</sub>' emission simply by increasing the number of fluorine atoms along a six-carbon alkyl backbone (Fig. 2-12b and Table 2-1). The energy shift goes from 133 meV for -(CH<sub>2</sub>)<sub>5</sub>CH<sub>3</sub> to 190 meV for -(CF<sub>2</sub>)<sub>5</sub>CF<sub>3</sub>. A consistent trend is observed in a series of partially fluorinated groups in which the distance between the electron withdrawing moiety (-CF<sub>3</sub>) and the defect site is varied by the chain length, -(CH<sub>2</sub>)<sub>n</sub>CF<sub>3</sub> (n = 0 - 5) (Table 2-1), resulting in the energy shift from 137 meV to

194 meV. When the first carbon of alkyl chains that is directly attached to a SWCNT is fluorinated, it significantly affects the energy separation indicating strong distance effect.

The optical properties of tunable fluorescent quantum defects with alkyl groups are strikingly different from those of nanocrystals. The size engineering of nanoparticles result in significant change in band gaps and thus both absorption and emission to be size-dependent. However, our alkylation on same size nanotube at low defect density can modulate emissions that are created at defect center while retaining similar absorption featuring through chemical engineering of the surface (Fig. 2-13). Using this technique, the absorption of *f*-SWCNTs are comparable with that of pristine while their emissions can be efficiently tuned by changing functionality.

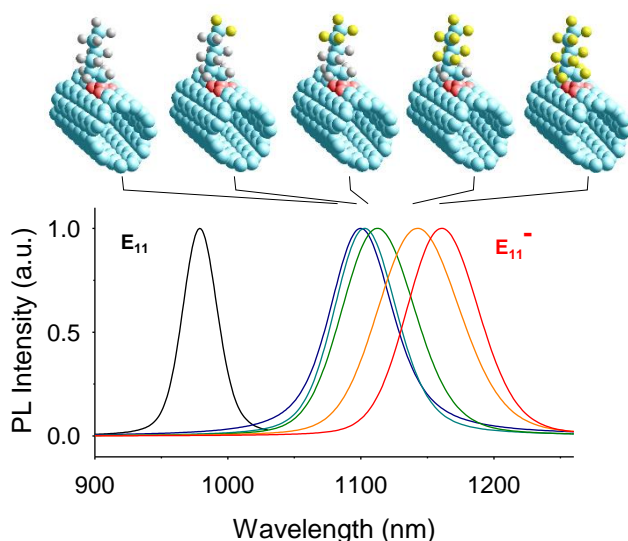


**Figure 2-12.** Tunable near-infrared PL from quantum defect-tailored (6,5)-SWCNTs with six-carbon alkyl chains with increasing numbers of fluorine substituents.

**Table 2-2.** Spectral characteristics of alkyl fluorescent quantum defects in (6,5)-SWCNTs and calculated inductive constants of the covalently bonded alkyl groups.

(6,5)-SWCNT-R	$E_{11}$ (nm)	$E_{11}$ FWHM (meV)	$E_{11}^-$ (nm)	$E_{11}^-$ FWHM (meV)	$\Delta E$ (meV)	$\sigma^*$ (calc)
Non-functionalized	979	37	-	-	0	-
-CH <sub>2</sub> CH <sub>2</sub> CH <sub>2</sub> CH <sub>2</sub> CH <sub>2</sub> CH <sub>3</sub>	981	45	1096	56	133	-0.774
-CH <sub>2</sub> CH <sub>2</sub> CH <sub>2</sub> CH <sub>2</sub> CH <sub>2</sub> CF <sub>3</sub>	980	45	1099	56	137	-0.462
-CH <sub>2</sub> CH <sub>2</sub> CH <sub>2</sub> CH <sub>2</sub> CF <sub>2</sub> CF <sub>3</sub>	980	38	1107	59	146	-0.127
-CH <sub>2</sub> CH <sub>2</sub> CF <sub>2</sub> CF <sub>2</sub> CF <sub>2</sub> CF <sub>3</sub>	983	40	1137	76	170	1.086
-CF <sub>2</sub> CF <sub>2</sub> CF <sub>2</sub> CF <sub>2</sub> CF <sub>2</sub> CF <sub>3</sub>	981	42	1155	69	190	4.867
-CH <sub>2</sub> CH <sub>2</sub> CH <sub>2</sub> CH <sub>2</sub> CH <sub>2</sub> CF <sub>3</sub>	980	45	1099	56	137	-0.462
-CH <sub>2</sub> CH <sub>2</sub> CH <sub>2</sub> CH <sub>2</sub> CF <sub>3</sub>	979	40	1104	59	143	-0.287
-CH <sub>2</sub> CH <sub>2</sub> CH <sub>2</sub> CF <sub>3</sub>	980	42	1101	55	140	-0.034
-CH <sub>2</sub> CH <sub>2</sub> CF <sub>3</sub>	980	42	1110	59	147	0.310
-CH <sub>2</sub> CF <sub>3</sub>	982	42	1114	67	150	1.244
-CF <sub>3</sub>	980	45	1158	63	194	3.961

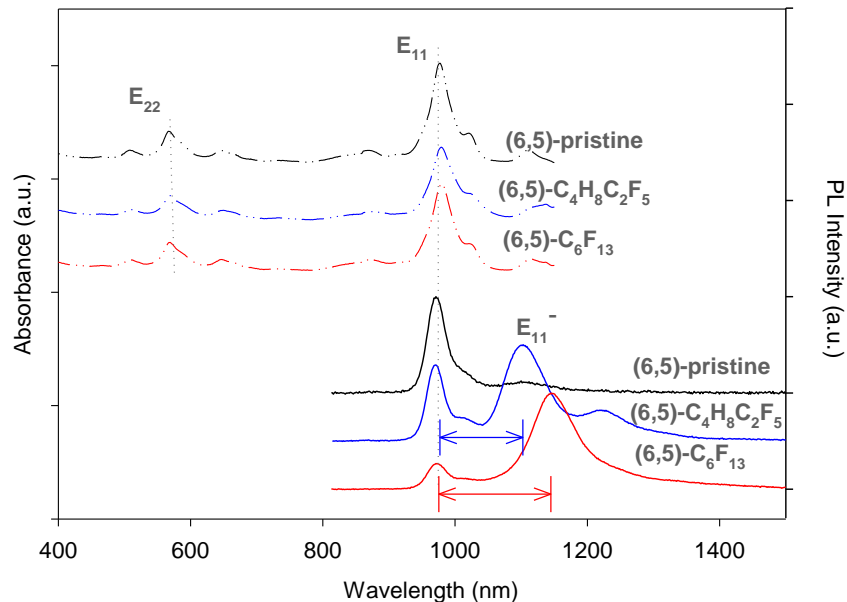


**Figure 2-13.** Correlated UV-Vis-NIR absorption and PL of (6,5)-SWCNTs with different functional groups.

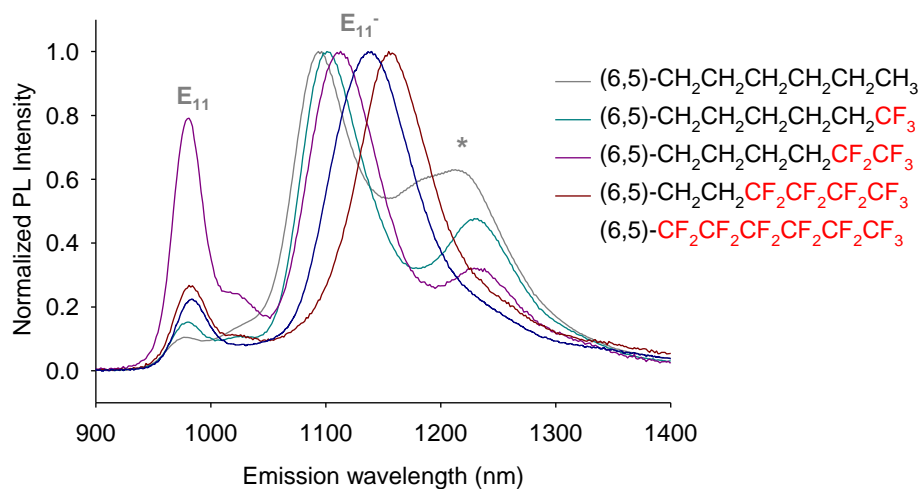


**Figure 2-14.** Emission spectra of (6,5)-SWCNTs with six carbon alkyl chains before peakfitting. Note that the additional satellite peaks are observed and marked as asterisk (\*) arising from a charged exciton (trion).

### 2.3.3. Inductive effects of alkyl defects

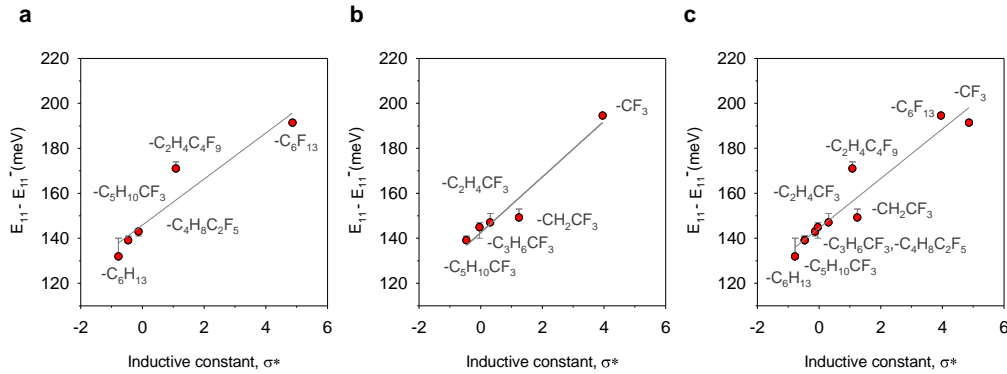


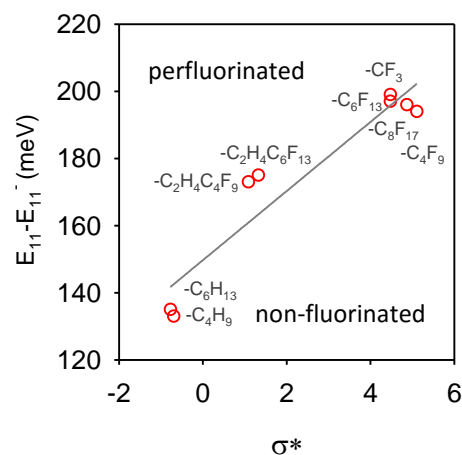
**Figure 2-15.** PL energy shifts versus calculated inductive constant ( $\sigma^*$ ). **a**,  $C_6H_{13-n}F_n$  (n = 0, 3, 5, 9, and 13). **b**,  $-(CH_2)_nCF_3$  (n = 0 - 5). **c**, The combined graph of **a** and **b**.

Our experimental results and quantum chemical theory consistently suggest that this tunability originates from inductive electronic effects associated with the covalently attached functional group (Fig. 2-15). These inductive electronic effects can be described by the empirical Taft constant or inductive constant ( $\sigma^*$ ), which quantifies the electronic influence of a substituent through sigma bonding in alkyl chains, excluding resonance effects that also occur in conjugated moieties<sup>75, 80</sup>. Consistent with this inductive picture, all perfluorinated alkyl defects in (6,5)-SWCNTs, including  $-CF_3$ ,  $-(CF_2)_3CF_3$ ,  $-(CF_2)_5CF_3$ , and  $-(CF_2)_7CF_3$ , produce similarly redshifted  $E_{11^-}$  peaks (by 190 - 194 meV), indicating comparable inductive constants regardless of the carbon chain length (Fig. 2-16). For  $CF_3$ -terminated alkyl defects, the defect PL energy decreases exponentially with chain length (or approximately, the distance from the defect site) (Table 2-1).

Quantitatively, the inductive constants can be calculated from the equation proposed by Cherkasov *et al.*<sup>75</sup>,

$$\sigma^* = 7.840 \sum_i \Delta\chi_i R_i^2 / r_i^2$$

where  $\Delta\chi_i$  is the difference between the electronegativities of  $i$ -th atom in the substituent and the reaction center,  $R_i$  is the covalent radius of the  $i$ -th atom, and  $r_i$  is the distance from this atom to the defect site on a SWCNT. We find that the PL energy shifts are linearly correlated with the calculated inductive constants ( $\sigma^*_{\text{calc}}$ ) (Fig. 2-15). This linear correlation confirms that the inductive effects associated with the alkyl groups on the fluorescent quantum defects are responsible for the observed energy shifts. It is a note that more than 20 different types of scales exist for inductive constants reported. They correlate well with one another. We found the reported inductive constants from literature for few alkyl groups used in this study that matches with our calculated results.



R-(6,5)-SWCNT	$E_{11}$ (nm)	$E_{11}^-$ (nm)	$E_{11}^- - E_{11}^+$ (meV)	$\sigma^*$ (ref)	$\sigma^*$ (calc)
I- $\text{CF}_3$	981	1158	193	0.44	4.4766
I- $\text{CF}_2\text{CF}_2\text{CF}_2\text{CF}_3$	983	1158	191	0.44	4.4766
I- $\text{CF}_2\text{CF}_2\text{CF}_2\text{CF}_2\text{CF}_2\text{CF}_3$	982	1158	192	-	4.8668
I- $\text{CF}_2\text{CF}_2\text{CF}_2\text{CF}_2\text{CF}_2\text{CF}_2\text{CF}_2\text{CF}_3$	982	1156	190	-	5.1057
I- $\text{CH}_2\text{CH}_2\text{CF}_2\text{CF}_2\text{CF}_2\text{CF}_2\text{CF}_3$	982	1133	168	-	1.0858
I- $\text{CH}_2\text{CH}_2\text{CF}_2\text{CF}_2\text{CF}_2\text{CF}_2\text{CF}_2\text{CF}_2\text{CF}_3$	983	1137	171	-	1.3264
I- $\text{CH}_2\text{CH}_2\text{CH}_2\text{CH}_3$	980	1093	131	0.01	-0.6952
I- $\text{CH}_2\text{CH}_2\text{CH}_2\text{CH}_2\text{CH}_2\text{CH}_3$	981	1096	133	0.03	-0.7745

**Figure 2-16.** Energy shift Vs calculated inductive constant with non-, partially-, and per-fluorinated alkyl groups.

### 2.3.4. Creation of extended fluorescent quantum defects: aryl and divalent defects

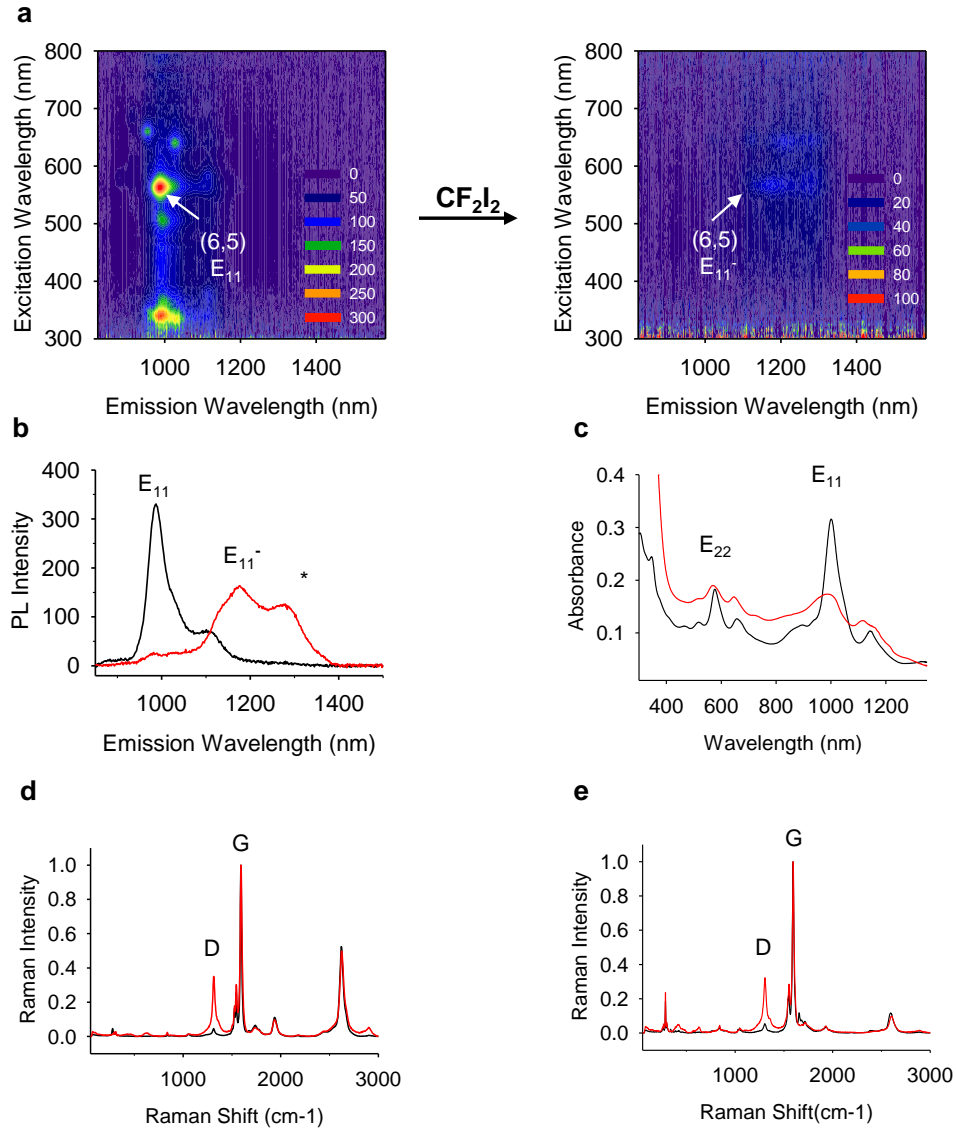


**Figure 2-17.** (6,5)-SWCNT $\rightarrow$ CF<sub>2</sub>. **a**, PL maps of pristine SWCNTs (left) and divalent alkyl-functionalized SWCNTs (right). **b**, 565 nm excitation emission spectra, **c**, UV-Vis-NIR Absorption spectra, **d**, Raman spectra with 532 nm laser and **e**, Raman spectra with 632.8 nm laser. The pristine is black solid and the f-SWCNTs are red solid line.

We found that this sidewall chemistry is not limited to creation of monovalent alkyl defects (-R), but is extended to alkyl divalent defects (>R) with di-iodide precursors (Fig. 2-17). The diiodo reactions does not typically occur in organic molecular systems<sup>76</sup> while only few conjugated structures with highly substituted  $\pi$ -bonds are reported to yield carbene-like products<sup>81</sup>. Divalent alkyl defects are characterized by PL, UV-Vis-NIR absorption and Raman spectra showing distinct different optical properties from monovalent defects including further redshifted defect PL at 1164 nm.

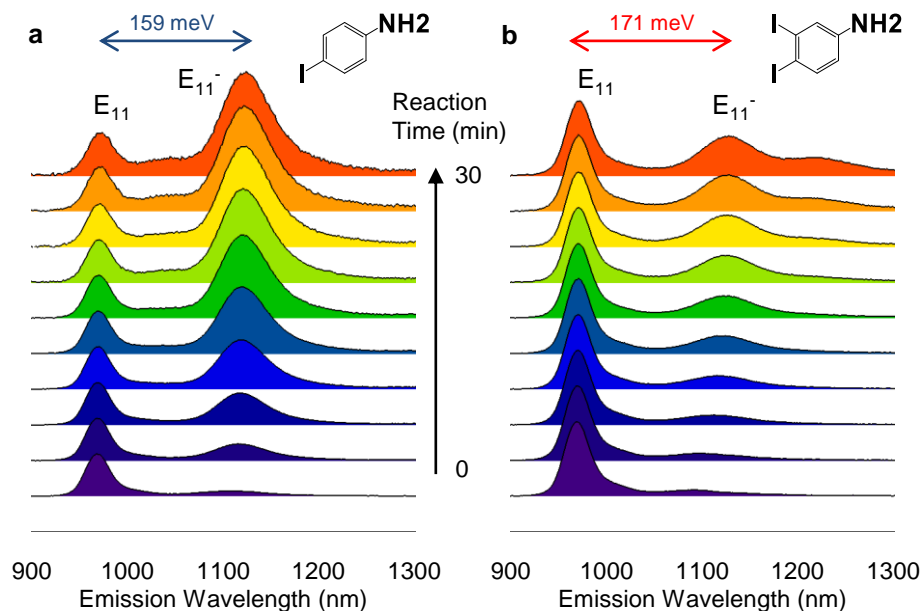


**Figure 2-18.** Creation of **a**, monovalent and **b**, divalent aryl defects of aminobenzene-(6,5)-SWCNTs. The aryl defect is created by excitation light (300-800 nm) without sodium dithionite. Single emission spectra are obtained with 565 nm excitation light and normalized by  $E_{11}$ .

In contrast to alkyl iodides, which require activation by sodium dithionite, aryl iodides alone can react with SWCNTs by excitation light activation (Fig. 2-18). By shining excitation light from 300 nm to 800 nm with 5 nm increment, we observe the development of defect photoluminescence with 159 meV energy shift for mono-aminobenzene defect and 171 meV shift for divalent aminobenzene defects starting from with 4-iodoaniline and 3,4-diidoaniline, respectively. We suspect that high  $\pi$ - $\pi$  interaction between aryl groups and carbon nanotubes leads to physisorption of aryl groups as a first step followed by creating aryl radicals with incident light to form covalent bond. Once the first iodide on the benzene ring reacts, the second iodide at ortho-positions can have high possibility to interact with SWCNTs, leading subsequent reaction on an adjacent carbon of the defect center on rigid SWCNT structures.

### 2.3.5. Tunable fluorescent quantum defects through aryl and divalent groups

Larger optical tunability can be achieved by applying diiodo-containing precursors to produce cycloaddition adducts. The divalent quantum defects fluoresce even further into the infrared than do the monovalent defects (Fig. 2-19). For instance, PL of (6,5)-SWCNT $\triangleright$ CH<sub>2</sub> occurs at 1125 nm, which is red-shifted by 31 meV more than its monovalent counterpart, (6,5)-SWCNT-CH<sub>3</sub>. In (6,5)-SWCNT $\triangleright$ CF<sub>2</sub>, the defect PL is further shifted to 1164 nm, 200 meV to the red of the parent nanotube PL. Divalent aryl defects, created by reaction with *o*-diidoaniline and *o*-diiodobenzene for instance, also produce new PL peaks that

redshift farther from the parent nanotube, in comparison with their monovalent counterparts, by 171 meV and 190 meV, respectively (Fig. 2-19 and Table 2-2).

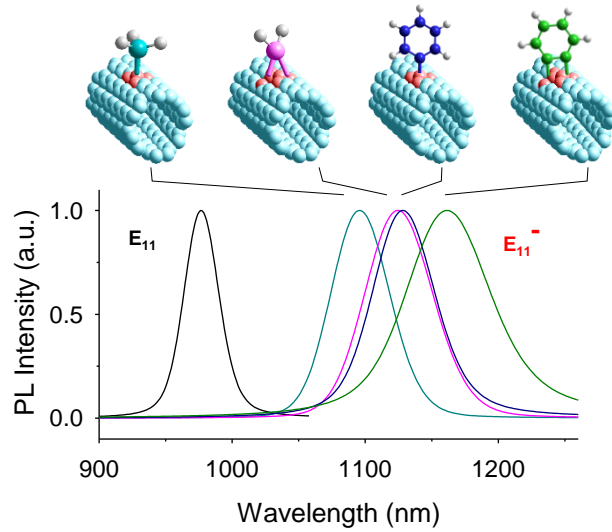


**Figure 2-19.** Comparison of monovalent and divalent fluorescent quantum defects. The nanotubes are excited at 565 nm. The parent exciton PL occurs at 979 nm while emission from the quantum defects are systematically tunable by changing the functional group including  $-\text{CH}_3$ ,  $>\text{CH}_2$ ,  $-\text{C}_6\text{H}_5$ , and  $>\text{C}_6\text{H}_4$ . The spectra are fitted with Voigt functions.

**Table 2-3.** PL spectral characteristics of (6,5)-SWCNTs covalently functionalized with different monovalent and divalent groups.

		monovalent			divalent				
(6,5)-SWCNT-R		$E_{11}$ (nm)	$E_{11}^-$ (nm)	$\Delta E$ (meV)	(6,5)-SWCNT-R	$E_{11}$ (nm)	$E_{11}^-$ (nm)	$\Delta E$ (meV)	
$-\text{CH}_3$		980	1094	132	$>\text{CH}_2$		980	1125	163
$-\text{CF}_3$		980	1158	194	$>\text{CF}_2$		980	1164	200
$-\text{C}_6\text{H}_5$		979	1129	168	$>\text{C}_6\text{H}_4$		986	1162	190
$-\text{C}_6\text{H}_4\text{NH}_2$		980	1121	159	$>\text{C}_6\text{H}_3\text{NH}_2$		980	1133	171

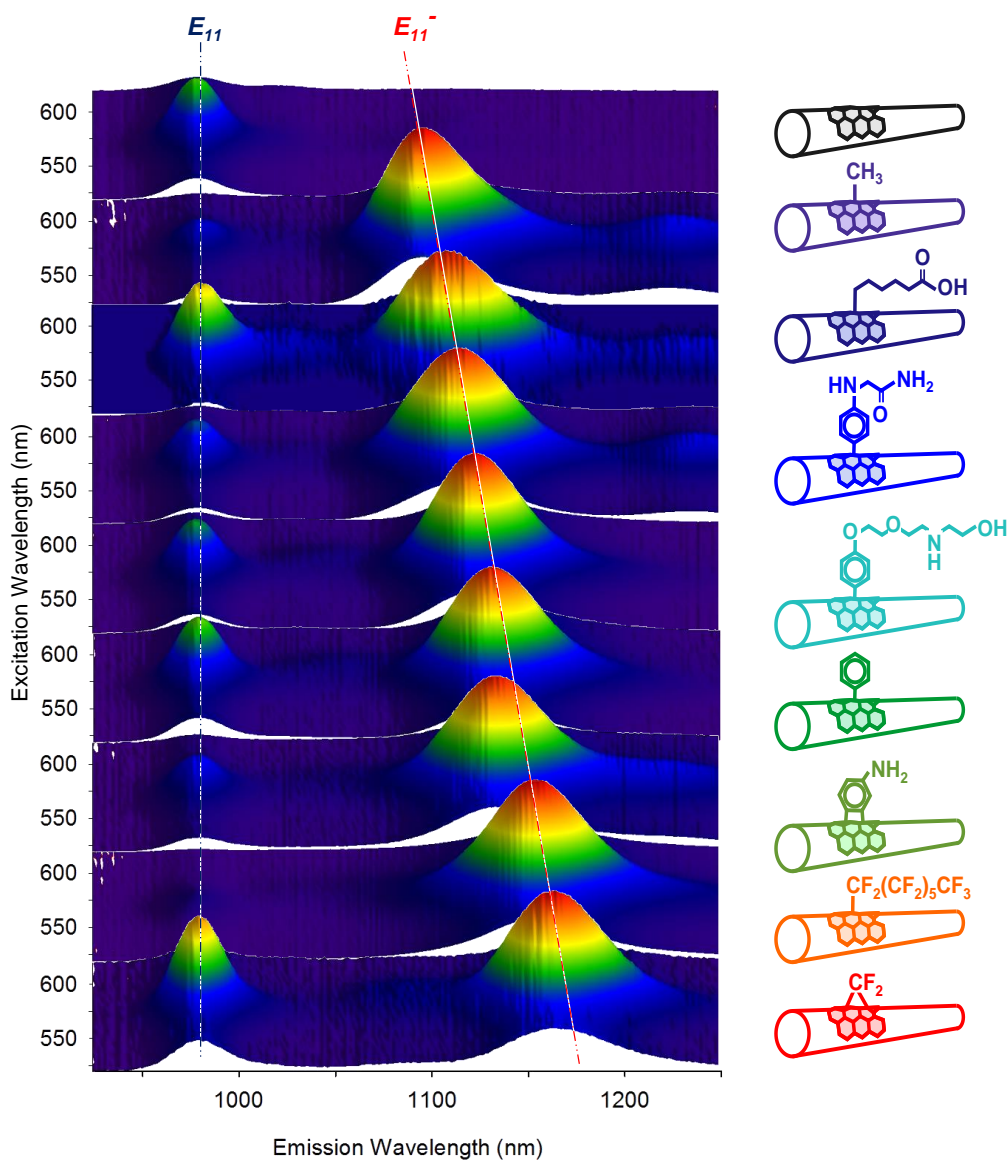


**Figure 2-20.** Excitation-emission maps of (6,5)-SWCNTs with chemically tailored fluorescent quantum defects.

This novel chemistry allows molecularly tunable fluorescent quantum defects to be created with highly predictable C-C bonding points from iodine-

containing hydrocarbon precursor (Fig 2-20 and 2-21). This highly controllable, tunable property was unattainable with previous exciton engineering techniques which are limited in specific types of functional groups and especially the exciton properties with well-defined divalent defects have not been investigated due to reactivity and stability of precursors<sup>25, 33, 34</sup>. In Fig. 2-20, we show nine fluorescent quantum defect systems with continuously tunable near-infrared PL and surface functionalities. Additional structures synthesized through these studies are listed in Table 2-3, demonstrating excellent chemical and optical tunability of this synthetic quantum system.

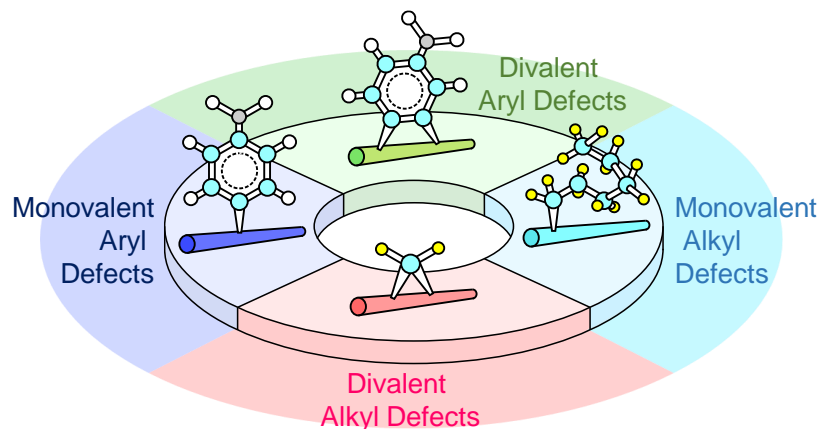
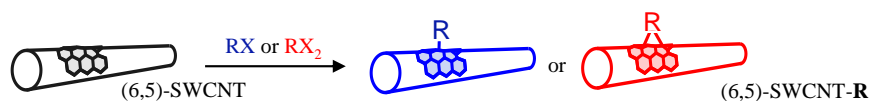


**Figure 2-21.** Schematic illustration of four classes of quantum defects.

**Table 2-4.** Alkyl/aryl halides used in this study and their defect PL.



(6,5)-SWCNT-R	$E_{11}$ (nm)	$E_{11}^-$ (nm)	$\Delta E$ (meV)	Source of Precursor	-X
Non -functionalized	979	-	-	-	
-CH <sub>3</sub>	980	1094	132	Sigma Aldrich	I
-CH <sub>2</sub> CH <sub>2</sub> CH <sub>2</sub> CH <sub>3</sub>	984	1099	132	Sigma Aldrich	I
-CH <sub>2</sub> CH <sub>2</sub> CH <sub>2</sub> CH <sub>2</sub> CH <sub>2</sub> CH <sub>3</sub>	981	1096	133	Sigma Aldrich	I
-CH <sub>2</sub> CH <sub>2</sub> CH <sub>2</sub> CH <sub>2</sub> CH <sub>2</sub> CH <sub>3</sub>	980	1097	135	Sigma Aldrich	Br
-CH <sub>2</sub> CH <sub>2</sub> CH <sub>2</sub> CH <sub>2</sub> CH <sub>2</sub> CF <sub>3</sub>	980	1099	137	Oakwood chemical	I
-CH <sub>2</sub> CH <sub>2</sub> CH <sub>2</sub> CH <sub>2</sub> CH <sub>2</sub> COOH	980	1102	140	Sigma Aldrich	Br
-CH <sub>2</sub> CH <sub>2</sub> CH <sub>2</sub> CF <sub>3</sub>	981	1101	140	Santa Cruz Biotech.	I
-CH <sub>2</sub> CH <sub>2</sub> CH <sub>2</sub> CH <sub>2</sub> CF <sub>3</sub>	979	1104	143	Aurum Pharmatech LLC.	I
-CH <sub>2</sub> CH <sub>2</sub> CF <sub>3</sub>	981	1110	147	Sigma Aldrich	I
-CH <sub>2</sub> CH <sub>2</sub> CH <sub>2</sub> CH <sub>2</sub> CF <sub>2</sub> CF <sub>3</sub>	980	1107	146	Matrix Scientific	I
-CH <sub>2</sub> CF <sub>3</sub>	982	1114	150	Sigma Aldrich	I
-CH <sub>2</sub> CF <sub>2</sub> CF <sub>2</sub> CF <sub>3</sub>	980	1114	152	Pfaltz and bauer	I
	980	1121	159	Sigma Aldrich	I
	984	1127	160	AstaTech, Inc.	I
	979	1121	160	Enamine LLC	I
>CH <sub>2</sub> ( <sup>12</sup> C)	979	1125	164	Sigma Aldrich	I <sub>2</sub>
>CH <sub>2</sub> ( <sup>13</sup> C)	980	1125	163	Cambridge Isotope	I <sub>2</sub>
	979	1125	164	Hit2lead	I
	979	1129	168	Sigma Aldrich	I
	980	1131	169	TCI	I
	980	1133	171	Spectra Group Limited Inc	I <sub>2</sub>
-CH <sub>2</sub> CH <sub>2</sub> CF <sub>2</sub> CF <sub>2</sub> CF <sub>3</sub>	983	1137	170	Sigma Aldrich	I
-CH <sub>2</sub> CH <sub>2</sub> CF <sub>2</sub> CF <sub>2</sub> CF <sub>2</sub> CF <sub>2</sub> CF <sub>3</sub>	983	1139	173	Sigma Aldrich	I
-CHF <sub>3</sub>	979	1138	177	Sigma Aldrich	I
	980	1145	182	Combiphos catalysts, INC	I
-CF <sub>2</sub> CF <sub>2</sub> CF <sub>2</sub> CF <sub>2</sub> CF <sub>2</sub> CF <sub>2</sub> CF <sub>3</sub>	979	1152	190	Sigma Aldrich	I
	986	1162	190	Sigma Aldrich	I <sub>2</sub>
-CF <sub>2</sub> CF <sub>2</sub> CF <sub>2</sub> CF <sub>2</sub> CF <sub>3</sub>	981	1155	190	Sigma Aldrich	I
-CF <sub>2</sub> CF <sub>2</sub> CF <sub>2</sub> CF <sub>3</sub>	979	1155	193	Sigma Aldrich	I
-CF <sub>3</sub>	980	1158	194	Sigma Aldrich	I
>CF <sub>2</sub>	980	1164	200	SynQuest Lab	I <sub>2</sub>

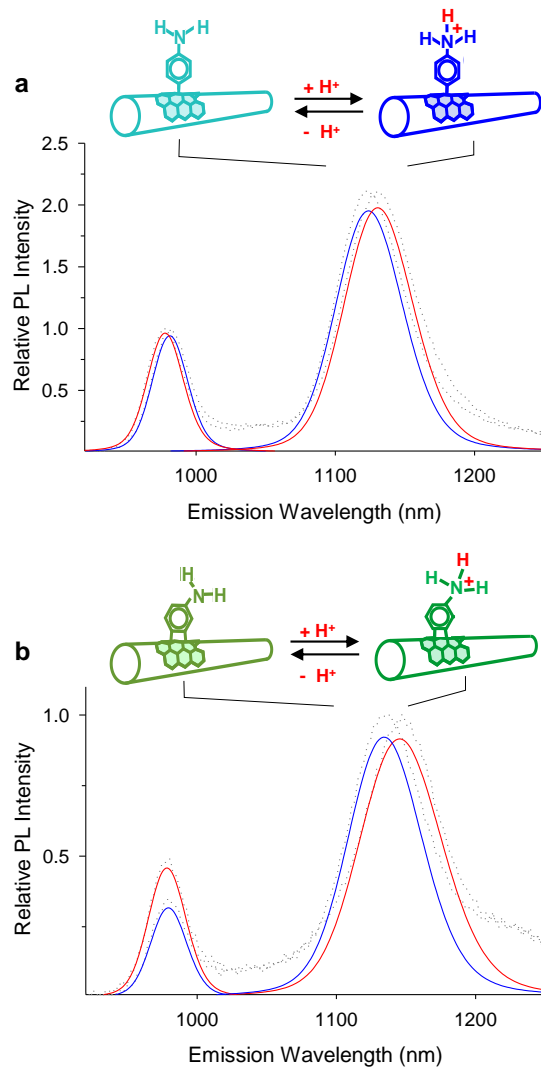


**Figure 2-22.** pH-responsive defect photoluminescence. **a**, monovalent and **b**, divalent aminobenzene-functionalized (6,5)-SWCNTs.

By trapping excitons at localized potential wells due to the quantum defects, we hypothesize that the exciton will respond sensitively to chemical events occurring at the defect site due to the amplification effects of the nanotube acting as an antenna (Fig. 2-22). The nanotube antenna harvests light efficiently and channels the generated excitons to the defect site, where the excitons recombine to

produce near-infrared PL encoding the chemical information at the functional groups. This picture is supported by titration experiments in which we detect  $H^+$  with both monovalent, (6,5)-SWCNT- $C_6H_4NH_2$ , and divalent, (6,5)-SWCNT- $C_6H_3NH_2$  defects. We find that as the amine moiety switches between the protonated and deprotonated states, the defect PL is shifted by  $\sim 13$  meV, which will be further explained in a great detail in next Chapter 3. This pH switching is not observed in defects that do not contain amines, including  $-C_6H_5$  and  $>C_6H_4$ , confirming the localized nature and the high chemical selectivity of the fluorescent quantum defects.

#### 2.3.6. DFT calculation of fluorescent quantum defects

In order to substantiate the fluorination effect on alkyl quantum defects, theoretical calculations based on density functional theory (DFT) are performed on an 8 nm (2 unit cells) long (6,5)-SWCNT using the B3LYP functional with a 6-31G\* basis set. The dangling bonds at the tube-ends are passivated with hydrogen atoms to avoid end-effects and introduction of edge states into the band gap of nanotubes. Four different types of groups including  $-CH_3$ ,  $-CF_3$ ,  $>CH_2$ , and  $>CF_2$  are used for covalent attachment on a nanotube. Single- and tri- methyl groups are treated as triple states while the rest of structures are minimized in single state. Edge effects on this system are negligible by using long tube length (8 nm) as we can see in the Mulliken charge distribution of pristine nanotubes at only edges while all other atoms are neutrally charged (Fig. 2-23).

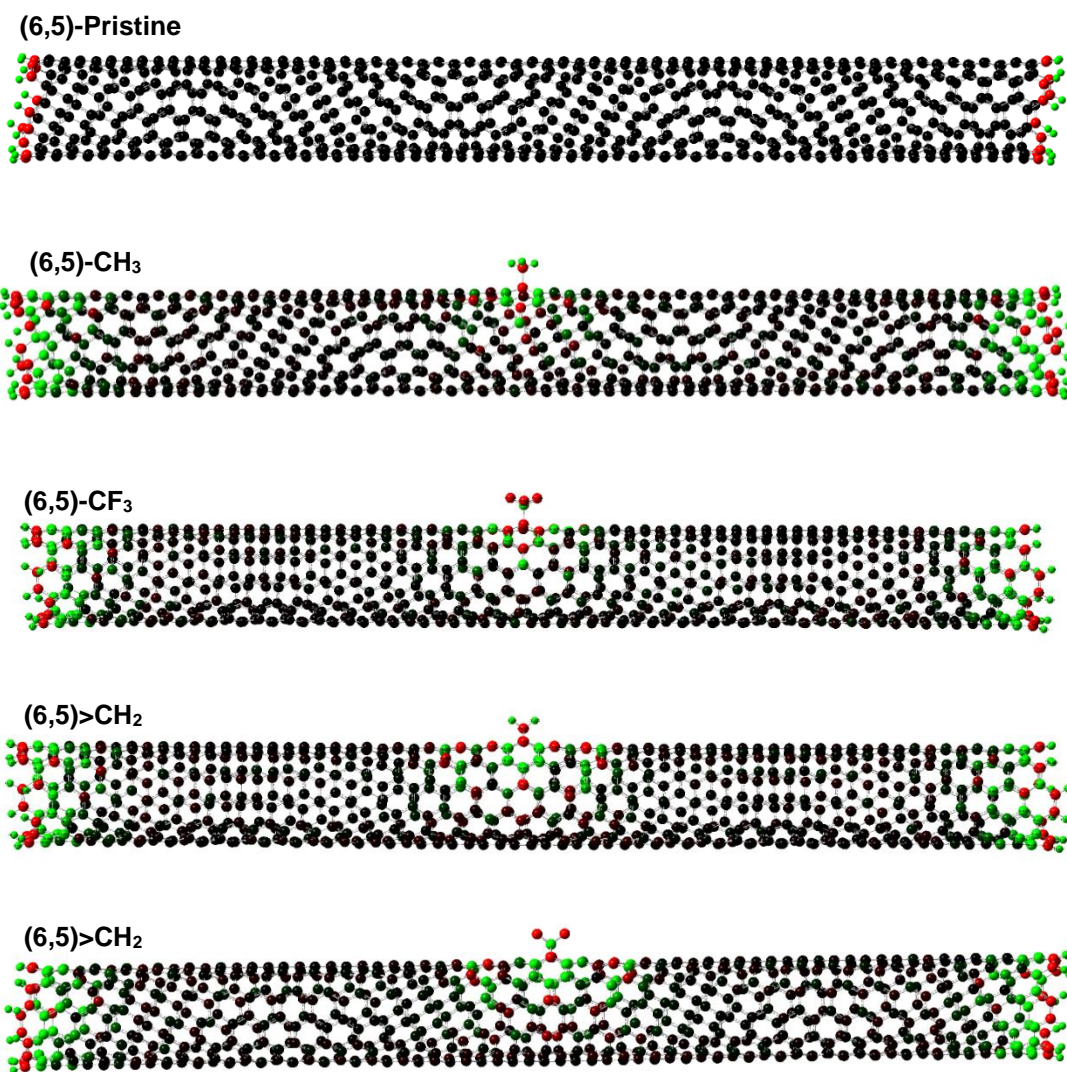


**Figure 2-23.** Mulliken charge distribution in a pristine (6,5)-SWCNT and single functional group attached SWCNTs (side view). Charges are shown in color gradient scheme, where red, black, and green colors are negative, zero, and positive charges, correspondingly.

A single functional group is introduced in the middle of tubes, which causes significant disruption of perfect conjugation of electrons only around a defect (Fig. 2-23). This charge distribution solely originates from a defect, not edge effects. It produces a specific distribution of charge depending on functional groups in CNTs.

For examples, methyl groups of  $-\text{CF}_3$  and  $-\text{CH}_3$  yield comparable charge distributions, which is the highest negative charge at para position (Fig. 2-24). In the case of  $>\text{CH}_2$  and  $>\text{CF}_2$ , the highest negative charge appears at orthogonal direction of carbon atoms to nanotube axis (Fig. 2-25). This highest charge guides us to predict the most thermodynamically favorable site for subsequent addition of functional groups. Due to huge number of permutations for third addition spots, we only demonstrated up to the attachment of two functional groups. The HOMO-LUMO gap due to the  $-\text{CF}_3$  defect is 43 meV smaller than that of  $-\text{CH}_3$ , which is in good agreement with the observed redshift (62 meV) in the defect PL (Table 2-4). This fluorine substitution effect is not limited to the most thermodynamically stable conformation (m in Fig. 2-24), but is also observed in all the other possible conformations. The theoretical calculation is corrugated the optical shift in terms of fluorination effect.

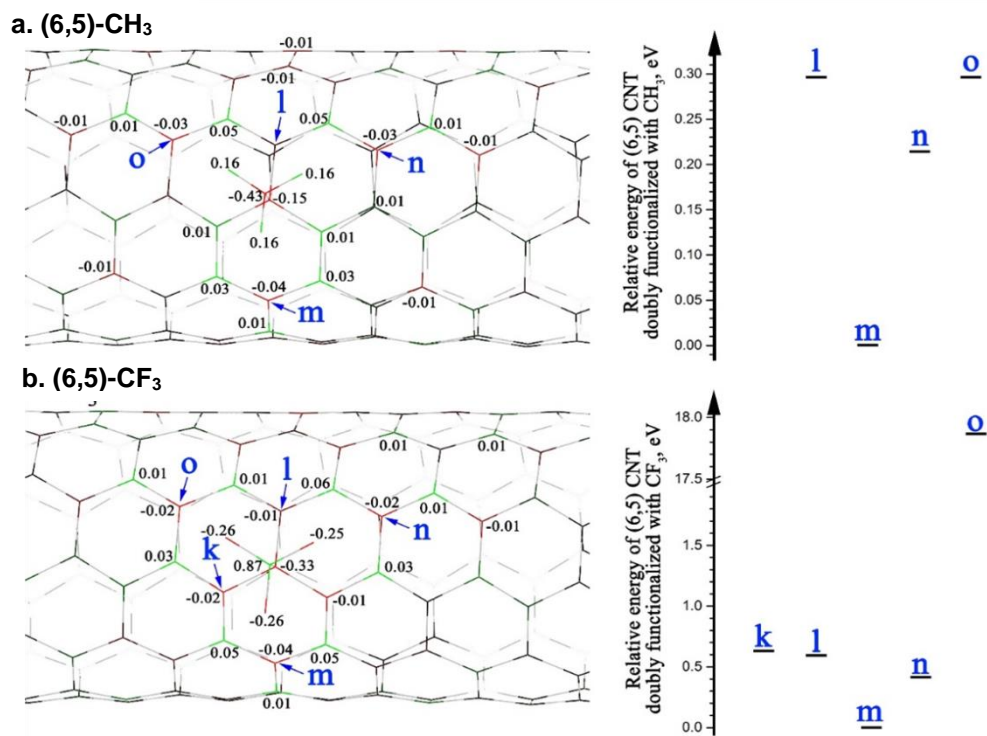


**Figure 2-24.** Distribution of Mulliken charges in (6,5)-SWCNTs with a single monovalent defect (left) and the relative energy diagrams when double monovalent defects are attached (right). **a**, -CH<sub>3</sub>. **b**, -CF<sub>3</sub>. Note that the most thermodynamically stable structure of methyl functionalized (6,5)-SWCNT is 1,4-para position (m), where the Mulliken charges are highly negative.

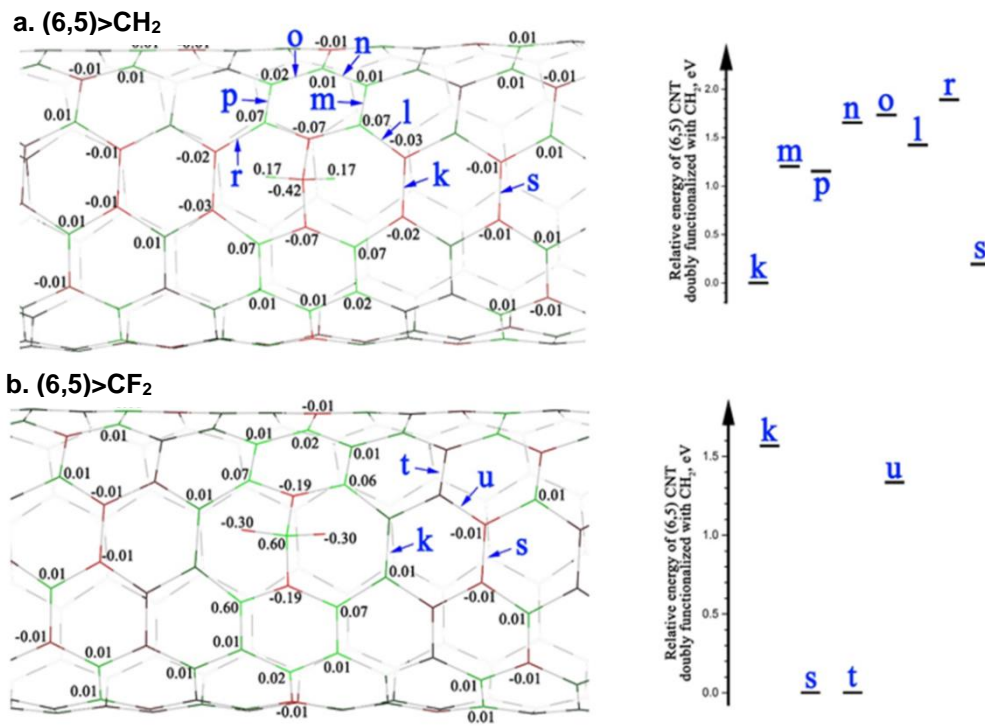


**Figure 2-25.** Distribution of Mulliken charges in (6,5)-SWCNTs with a single divalent defect (left) and the relative energy diagrams of (6,5)-SWCNTs with two divalent defects (right). **a**, >CH<sub>2</sub>. **b**, >CF<sub>2</sub>.

The similar theoretical study of charge localization has been done with the SIESTA method<sup>36</sup>. The (5,5)-SWCNTs with single addition of C<sub>5</sub>H<sub>10</sub>COOH group shows the high Mulliken charge density at three adjacent atoms of a defect carbon (1,2- or ortho position)<sup>36</sup>. Even though the slight difference of the second addition position between (6,5)-SWCNTs-CH<sub>3</sub> and (5,5)-SWCNTs-C<sub>5</sub>H<sub>10</sub>COOH might arise from the nature of functional groups, chirality or calculation methods, both calculation results clearly support the charge localization around defects.

**Table 2-5.** Orbital energies of simulated structures. Note that all conformations of (6,5)-SWCNT-(CF<sub>3</sub>)<sub>n</sub> (n = 1, 2) produce larger shifts in emission energy (E<sub>11</sub> - E<sub>11'</sub>) compared to their respective -CH<sub>3</sub> defects.

Model	E <sub>HOMO-1</sub> (eV)	E <sub>HOMO</sub> (eV)	E <sub>LUMO</sub> (eV)	E <sub>LUMO-1</sub> (eV)	E <sub>HOMO</sub> <sup>-</sup> E <sub>LUMO</sub> (eV)	E <sub>HOMO-1</sub> <sup>-</sup> E <sub>LUMO-1</sub> (eV)	E <sub>11</sub> -E <sub>11'</sub> (meV)
pristine	-4.603	-4.593	-3.001	-3.000	1.592	1.603	-
k_CH <sub>3</sub>	-4.599	-4.488	-3.196	-2.956	1.292	1.643	351
l_CH <sub>3</sub>	-4.599	-4.534	-3.032	-2.947	1.503	1.652	149
m_CH <sub>3</sub>	-4.614	-4.520	-3.103	-2.941	1.417	1.672	256
o_CH <sub>3</sub>	-4.598	-4.459	-3.176	-2.949	1.283	1.649	366
k_CF <sub>3</sub>	-4.634	-4.542	-3.308	-2.993	1.234	1.641	407
l_CF <sub>3</sub>	-4.633	-4.592	-3.118	-2.988	1.474	1.645	171
m_CF <sub>3</sub>	-4.644	-4.573	-3.207	-2.979	1.366	1.664	298
o_CF <sub>3</sub>	-4.607	-4.470	-3.192	-2.957	1.278	1.650	372

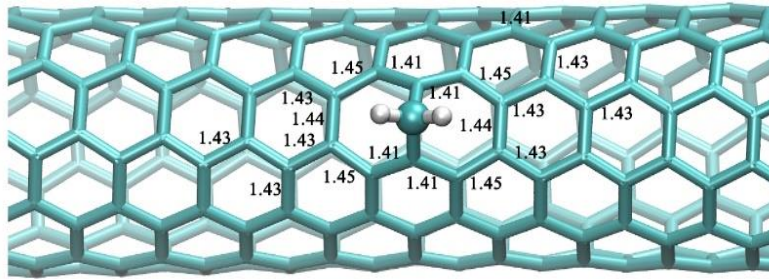


**Figure 2-26.** Bond lengths of (6,5)-SWCNT>CH<sub>2</sub>. C-C bond length around the >CH<sub>2</sub> defect is slightly longer than that in the pristine SWCNT (1.42 Å). The circumferential C-C bond at the defect site is increased to 2.17 Å and thus is broken to adopt an opened three-membered ring.

The calculations of (6,5)-SWCNT>CH<sub>2</sub> and (6,5)-SWCNT>CF<sub>2</sub> suggested the a ring-opened structure that preserves  $\pi$  conjugation of the nanotube (Fig. 2-26). The breaking of one circumferential C-C bond in the nanotube is ~1.3 eV more thermodynamically stable than the formation of three-membered-ring-like

(cyclopropyl) adducts along the chiral directions. Mulliken analysis shows, again, that the charges accumulate preferentially around the defect, driving the subsequent additions of  $\text{>CH}_2$  or  $\text{>CF}_2$  groups along the longitudinal direction (k, s in Fig 2-25). The ring opening structure from our calculation is consistent with previous studies including theoretical calculations using B3LYP/6-31G\* and experimental results from confocal Raman spectroscopy for the cycloaddition of  $\text{CCl}_2$  groups in (6,5)-SWCNTs<sup>82, 83</sup>. Li *et al.* found that the ring opening adduct is more thermodynamically stable in small diameter SWCNTs with higher curvature (distortion) of circumferential C-C bonds (-30 kcal/mol for (6,5)-SWCNT)<sup>82</sup>. They illustrate that only zigzag tubes with smaller curvature can have adducts with three membered-ring structures from cycloaddition. Also, confocal Raman spectroscopy reveals that the orthogonal addition of carbene groups ( $-\text{CCl}_2$ ) on SWCNTs leads C-C bond breakage by resulting in interesting Raman signature of two main G mode peaks, named  $\text{G}^-$  ( $1570 \text{ cm}^{-1}$ ) and  $\text{G}^+$  ( $1590 \text{ cm}^{-1}$ )<sup>83</sup>.

The frontier orbital wavefunctions of the nanotube become localized to a 2 nm region around the defect site (Fig. 2-27). This localization effect is less pronounced for divalent defects, suggesting some degrees of tunability by controlling the bonding structure (Fig. 2-28). In all of these systems, this localization effect is distinctly different from defect-free carbon nanotubes, in which the wavefunction is delocalized and excitons are highly mobile.

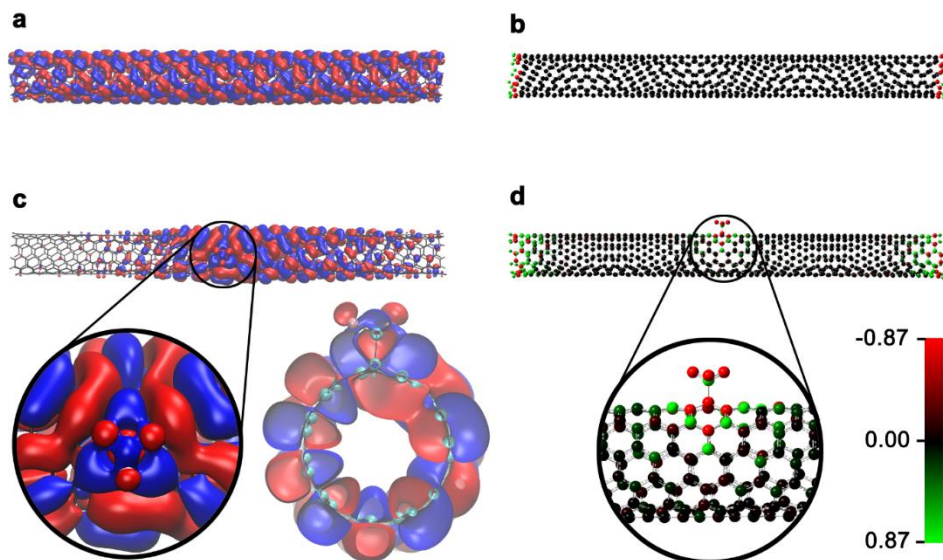


**Figure 2-27.** Localization of charges and frontier orbital wavefunction around a fluorescent quantum defect. **a**, HOMO and **b**, charge distribution in a pristine (6,5)-SWCNT. The nanotube is free of defects other than its ends, which are terminated with hydrogen atoms to preserve the  $sp^2$  hybridization. **c**, HOMO of a (6,5)-SWCNT-CF<sub>3</sub>. Inset shows the HOMO for -CF<sub>3</sub> functionalization on a cut perpendicular to the tube. The orbital is plotted at its iso-surface equal to 0.003. **d**, Positive (green) and negative (red) charges.

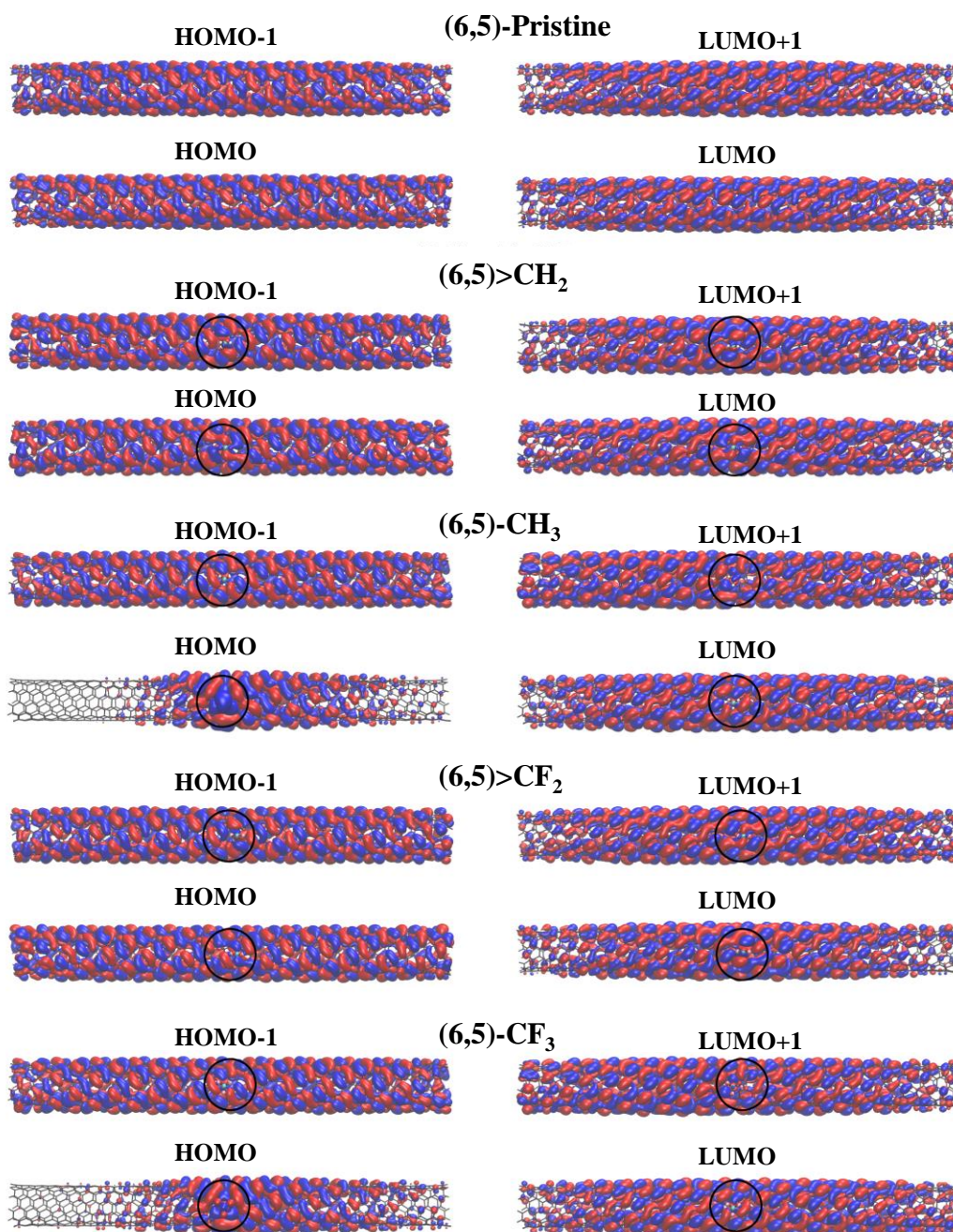


**Figure 2-28.** The HOMO and LUMO of pristine-SWCNTs and (6,5)-SWCNTs with >CH<sub>2</sub>, -CH<sub>3</sub>, >CF<sub>2</sub>, and -CF<sub>3</sub>.

## **2.4. Conclusions**

In this chapter, we show that it is possible to create a new series of quantum systems chemically from semiconducting SWCNTs of the same chirality through molecular engineering of covalently attached functional groups. This new class of synthetic quantum systems shows molecular-specific optical and electronic properties that are distinctly different from existing nanostructures. Molecularly tunable fluorescent quantum defects thus add an entirely new dimension to the development of carbon nanomaterials with specific optical and chemical properties. Given the rich molecular moieties and recent experimental advances in synthesis and sorting of single-chirality SWCNTs<sup>59, 84</sup>, one may anticipate that a large variety of near-infrared quantum emitters can now be rationally designed and chemically created for applications from *in vivo* bioimaging and sensing.

## Chapter 3 . Optical Probing of Local pH and Temperature in Complex Fluid through Semiconducting Carbon Nanotubes

*Adapted from H. Kwon<sup>\*</sup>, M. Kim<sup>\*</sup>, B. Meany, Y. Piao, L. R. Powell, and Y. H. Wang, Journal of Physical Chemistry C, 119, 3933.(2015)*

*\*H.K., M.K. contributed equally to this work. Y.H.W., H.K., and M.K. conceived and designed the experiments. H.K., M.K., Y.P., and L.P. performed pH and temperature experiment and B.M. performed gel chromatography sorting experiment experiments. Y.H.W., H.K., and M.K. wrote the manuscript with inputs from all co-authors.*

### 3.1. Introduction

The concentration of protons in an aqueous solution, measured as pH, and the temperature are critical thermodynamic variables that impact processes ranging from material synthesis to cellular dynamics or tumor cells.<sup>85-87</sup> However, it is challenging to quantify these parameters in complex systems such as nanoscale reaction mixtures and complex fluid, especially when high sensitivity, selectivity, and spatial resolution (sub-micrometers) are simultaneously required for remote measurement.<sup>88-90</sup> For instance, several approaches have been proposed to detect proton concentration or temperature response; among which photoluminescence (PL) of organic dyes and synthetic nanoparticles have emerged as promising solutions to *in vivo* measurement and imaging.<sup>91-94</sup> One issue limiting the applications of these optical sensors is the small biological penetration depth of their visible and first near-infrared window (NIR-I, 0.75-0.9 $\mu$ m) PL. Moreover, when optical sensors based on PL intensity, energy shifts, and emission lifetime

and anisotropy are compared to an external standard, it is difficult to resolve the complex chemical environment of biological systems with high fidelity.

Over a decade, semiconducting single-walled carbon nanotubes (SWCNTs) have attracted considerable research interest in developing innovative biomedical imaging capabilities) owing to their remarkable photostability, NIR-II emission (which penetrates deeply in biological tissues with minimal autoscattering), and availability of a rich library of structures known as  $(n, m)$  chiralities.<sup>15</sup> However, the chemical selectivity of unfunctionalized nanotubes is generally poor,<sup>95,96</sup> which makes it difficult to differentiate specific chemicals such as  $H^+$  in the complex chemical environment of biological systems.

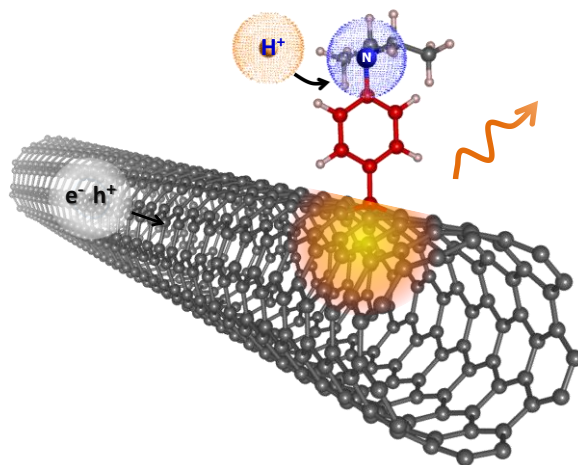


**Figure 3-1.** Sketch of optical probing of pH through defect photoluminescence in a SWCNT.

In Chapter 3, the first pH and temperature bi-functional optical nanoprobe based on a new sensing mechanism will be discussed. It is enabled by infrared defect PL of covalently functionalized semiconducting SWCNTs (*f*-SWCNTs) (Fig. 3-1). Covalently attaching an aminoaryl functional group to a SWCNT introduces an  $sp^3$  defect in the  $sp^2$  carbon lattice, creating an optically allowed defect state from which arises the defect PL ( $E_{11}^-$ ), with a substantial red-shift from the original  $E_{11}$ . Protonation of the amine substituent substantially modifies the energy level of the  $sp^3$  defect state, resulting in an even further red-shifted  $E_{11}^-$  emission. Therefore, this chemical event can be precisely reported as an energy shift in the defect PL, relative to a built-in reference,  $E_{11}$ , whose position stays unchanged with pH ( $< 2$  nm). When the nanotube is optically excited, the mobile excitons can become trapped efficiently at the proton-selective  $sp^3$  defect center and are recombined locally such that the nanotube acts as a light-harvesting antenna that amplifies the chemical information encoded by the defect PL. While our experiments and others consistently suggest that  $E_{11}^-$  PL occurs from the same defect site, this speculation has yet to be experimentally confirmed and warrants further work that may be enabled by single molecule and near-field imaging capabilities. Furthermore, the solution temperature can be simultaneously measured from the  $E_{11}/E_{11}^-$  intensity ratio because in the same chemical environment the relative population of  $E_{11}$  and  $E_{11}^-$  excitons is determined solely by the local temperature and closely follows the van't Hoff equation.

The proposed bi-functional nanoprobe is made possible by an unexpected finding from our team that controlled functionalization of SWCNTs with aryl

functional groups creates a new, ultra-bright defect PL in the NIR-II. Defect PL is also observed in oxygen doped SWCNTs<sup>23</sup> and with alkyl functional groups,<sup>24,25</sup> although in the latter two cases, the PL is not as bright due to distinctly different mechanisms. Notably, the photoluminescence of *f*-SWCNTs responds sensitively to specific chemicals and biomolecules, in stark contrast with unfunctionalized SWCNTs. Our finding opens the possibility of covalent engineering of SWCNTs for optical biosensing applications.

### **3.2. Experimental methods**

#### 3.2.1. Creation of *sp*<sup>3</sup> defect sites on SWCNTs with diazonium chemistry

Aryl diazonium salts were freshly synthesized from anilines (Sigma Aldrich) following a modified literature method<sup>80</sup> except 4-diazo-*N,N*-diethylaniline tetrafluoroborate, which was used as received from MP Biomedicals. The diazonium salts were dissolved and diluted in 1 wt.% SDS/D<sub>2</sub>O to give 10<sup>-2</sup> to 10<sup>-6</sup> M solutions, which were then reacted with the SWCNTs solutions. The reaction mixture was stirred at room temperature and protected from light by covering the reaction vial with aluminum foil. Reaction evolution was monitored *in situ* by UV-Vis-NIR absorption spectroscopy using a Lambda 1050 UV-Vis-NIR spectrophotometer (Perkin Elmer) and by photoluminescence spectroscopy with a NanoLog spectrofluorometer (Horiba Jobin Yvon). The spectrofluorometer was equipped with a 450 W Xenon arc lamp and a liquid-N<sub>2</sub> cooled InGaAs array detector. The slit widths for excitation and emission were 10 nm and 20 nm,

respectively. The reactions completed after 10 days or when stable  $E_{11}^-$  photoluminescence was established.

### 3.2.2. pH-dependent defect photoluminescence

The solution pH was adjusted by adding small aliquots of 0.02 M HCl and NaOH solutions (Sigma Aldrich) and was determined by pH meter (Accumet™ AB15+ Basic and BioBasic pH meters and Accumet™ pH/ATC electrodes, Fisher Scientific). The pH-sensitive PL was obtained when the integrated area of  $E_{11}^-$  was greater than that of  $E_{11}$ .

### 3.2.3. Temperature-dependent defect photoluminescence

The functionalized-SWCNT solution was heated from 15 °C to 85 °C using a circulating water bath, and the photoluminescence was obtained in increments of 5 °C. The solution temperature was measured with the Surface Temperature Sensor and LabQuest 2 (Vernier). The PL peaks of  $E_{11}$  and  $E_{11}^-$  were fitted with Voigt line shapes using Peakfit v4.12 (SeaSolve), and then the integrated peak areas were plotted as a function of temperature. To avoid peak fitting artifacts, we compared different peak fitting parameters and confirm the robustness of fitting which resulted in the same relative potential well depth between the fully protonated (pH 3.77) and the fully de-protonated states (pH 9.01).

#### 3.2.4. Defect photoluminescence as a pH sensor in biological medium

For the biological medium test, 0.3 mL of *N,N*-diethylaminoaryl-*f*-SWCNTs in 1 wt.% SDS-D<sub>2</sub>O (optical density ~0.1 at E<sub>11</sub>, [C, CNT Carbon]/[Dz, Diazonium] = 1:100) was added to 1.2 mL of 10% v/v fetal bovine serum (Sigma-Aldrich) and DMEM media (Invitrogen) with 150 mM sodium chloride salt (EMP chemicals, ACS grade). To determine the influence of salts, 0.2 mL of *f*-SWCNTs in 1 wt.% SDS-D<sub>2</sub>O was added to 1.3 mL sodium chloride solutions of 50, 100, 150, and 300 mM. The emission spectra of the samples were taken at 565 nm excitation with adjusted integration time.

### **3.3. Results and discussion**

#### 3.3.1. The results of pH-sensitive defect photoluminescence

*N,N*-diethyl-4-aminobenzene functional groups are covalently attached to the sidewalls of (6,5)-SWCNTs via diazonium chemistry to create discrete, pH and temperature-sensitive defect centers (Fig. 3-2). The surface density of the functional groups is kept low, approximately one every 20-100 nm, in order to maintain the E<sub>11</sub> PL as an inherent reference while introducing the defect PL (E<sub>11</sub><sup>-</sup>) as a probe. The functional density was confirmed by correlated PL, UV-Vis-NIR absorption, Raman scattering and X-ray Photoelectron Spectroscopy<sup>25</sup>. The functionalized nanotubes, (6,5)-SWCNT-C<sub>6</sub>H<sub>4</sub>N(CH<sub>2</sub>CH<sub>3</sub>)<sub>2</sub>, showed two distinct, near-infrared emission peaks at pH 7.40, including E<sub>11</sub> emission at 979 nm as well

as  $E_{11}^-$  emission at 1120 nm. The  $E_{11}$  peak position is independent of pH and therefore can be used as an internal reference.

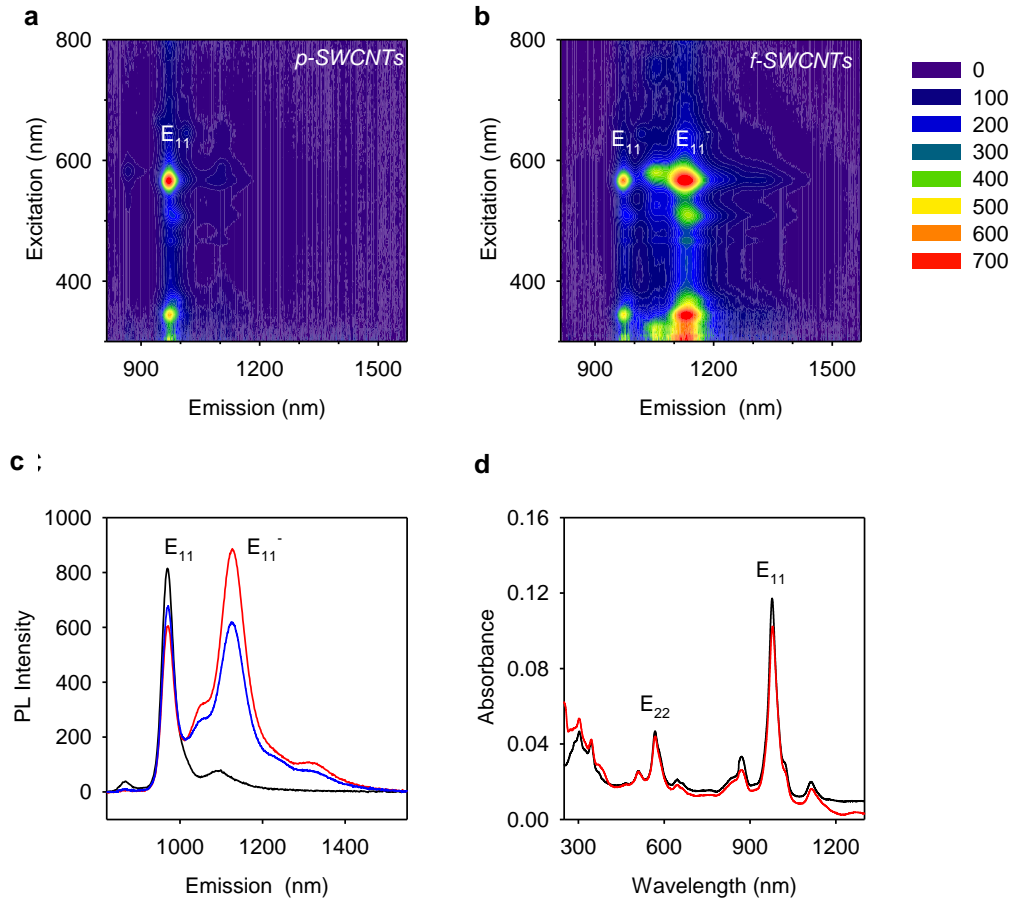


**Figure 3-2.** Defect photoluminescence arises from  $sp^3$  defects. Excitation-emission PL maps of **a**, pristine and **b**,  $N,N$ -diethylaminobenzene functionalized (6,5)-SWCNTs. **c**, Emission spectra at 565 nm excitation of pristine (6,5)-SWCNTs (black) and (6,5)-SWCNT- $C_6H_4N(CH_2CH_3)_2$  when the  $E_{11}/E_{11}^-$  intensity ratio is 1:1 (blue) and 1:2 (red), respectively. The functionalized SWCNTs show 1.3 - 2.4-fold enhancement of the PL. **d**, UV-Vis-NIR absorption spectra of pristine (black) and (6,5)-SWCNT- $C_6H_4N(CH_2CH_3)_2$  with an  $E_{11}/E_{11}^-$  intensity ratio of 1:2 (red).

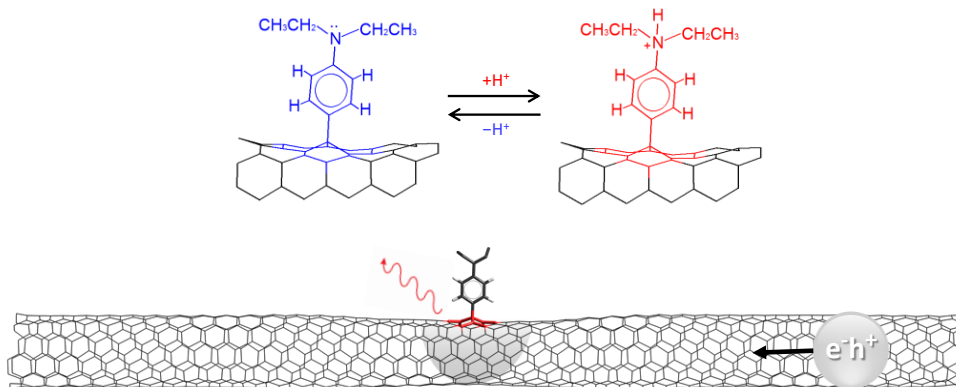


**Figure 3-3.** Schematic illustration of NIR-II pH sensor based on carbon nanotube antenna-amplified defect photoluminescence. Protonation of an aminobenzene functional group covalently attached on a (6,5)-SWCNT modifies the energy level of the  $sp^3$  defect state from which a new photoluminescence arises. The nanotube acts as an optical antenna that efficiently harvests light and channels the generated excitons to the defect site, where the excitons recombine to produce near-infrared photoluminescence encoding the chemical information at the functional groups (red arrow).

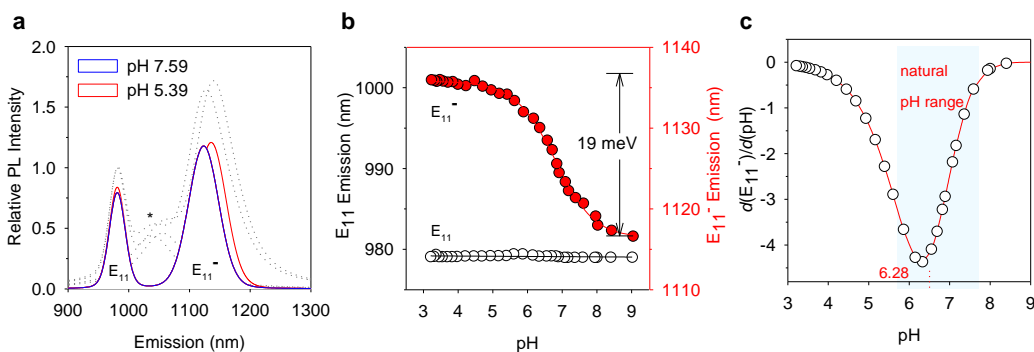
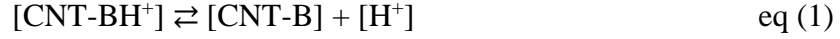


**Figure 3-4.** Defect photoluminescence of (6,5)-SWCNT- $C_6H_4N(CH_2CH_3)_2$  is strongly dependent on pH. **a**, The  $E_{11}^-$  emission of the *N,N*-diethyl-4-aminobenzene functionalized (6,5)-SWCNTs redshifts from 1117 nm to 1136 nm, as the pH changes from 9.02 to 3.97. The  $E_{11}$  and  $E_{11}^-$  emission curves (solid lines) are fitted and plotted on top of the original data (dotted lines). The difference is due to (6,4)-

impurity in the solution, marked with an asterisk (\*). **b**, The  $E_{11}^-$  emission responds sensitively to the pH change whereas  $E_{11}$  remains unchanged. **c**, The first derivative of the relative PL energy shift of  $E_{11}$  and  $E_{11}^-$  as a function of pH determines the  $pK_a$  for the nanoprobe.

On the contrary, defect PL of (6,5)-SWCNT- $C_6H_4N(CH_2CH_3)_2$  demonstrates a strong pH-dependence that closely traces the reproducible titration curve of the aminobenzene group (Fig 3-3 and Fig 3-4). Within the pH window from 4.5 to 8.5,  $E_{11}^-$  responds to pH change by shifting the PL peak position, creating a working window spanning 4 pH units. In particular, this working window completely covers the physiologic pH range for biological fluids (pH 5.5 to 8.0). The defect PL is resolvable to changes of 0.2 pH units within pH 5.5 to 8.0 and 0.3 pH units across pH 4.0 to 8.0. This sensitivity is among the highest reported for nanoprobes. Above pH 8.5 (or below pH 4.5), the emission vs pH curve plateaus as expected for a fully de-protonated (or protonated) state. Taking the first-order derivative (Fig. 3-4c), the  $pK_a$  of the covalently attached aminobenzene group was determined to be 6.28. This value is in good agreement with the  $pK_a$  of *N,N*-dimethylammonium benzene ( $pK_a = 5.2$ ); the slightly basic nature of the nanoprobe can be attributed to the influence of the electron-rich SWCNTs. The positive correlation strongly suggests that the observed pH dependence originates from the covalently attached aminoaryl functional groups on carbon nanotubes.

The pH-dependent response of the defect PL is correlated with the equilibrium between the protonated and deprotonated forms of the amine substituents:



where  $[\text{CNT-BH}^+]$  and  $[\text{CNT-B}]$  are the concentration of CNT-anchored  $\text{C}_6\text{H}_4\text{N}^+(\text{CH}_2\text{CH}_3)_2\text{H}$ ,  $\text{C}_6\text{H}_4\text{N}(\text{CH}_2\text{CH}_3)_2$ , respectively. From the Henderson-Hasselbalch equation,

$$\text{pH} = \text{pKa} + \log\left(\frac{[\text{CNT-B}]}{[\text{CNT-BH}^+]}\right) \quad \text{eq (2)}$$

and the fact that the concentration is directly proportional to the fluorescence intensity in the dilute limit, the pH is determined as

$$\text{pH} = 6.28 + C * \log\left(\frac{I_{\text{E11}^-, \text{B}}}{I_{\text{E11}^-, \text{A}}}\right) \quad \text{eq (3)}$$

where  $I_{\text{E11}^-, \text{B}}$  and  $I_{\text{E11}^-, \text{A}}$  are the integrated area of defect PL from amine and ammonium functional groups, respectively; and  $C$  is a correction factor, which is experimentally determined as  $2.04 \pm 0.03$  for (6,5)-SWCNT- $\text{C}_6\text{H}_4\text{N}(\text{CH}_2\text{CH}_3)_2$  (Fig. 3-5). The correction factor arises from the difference in quantum yields between the protonated and deprotonated states of the defect photoluminescence. This factor may be dependent on the nanotube chirality, as suggested by the chirality-dependent defect photoluminescence. Although we do not have the data points to quantitatively define “ $C$ ” for each chirality other than (6,5)-SWCNTs, this may be an interesting question for follow-up experiments as pure samples become available for other chiralities.

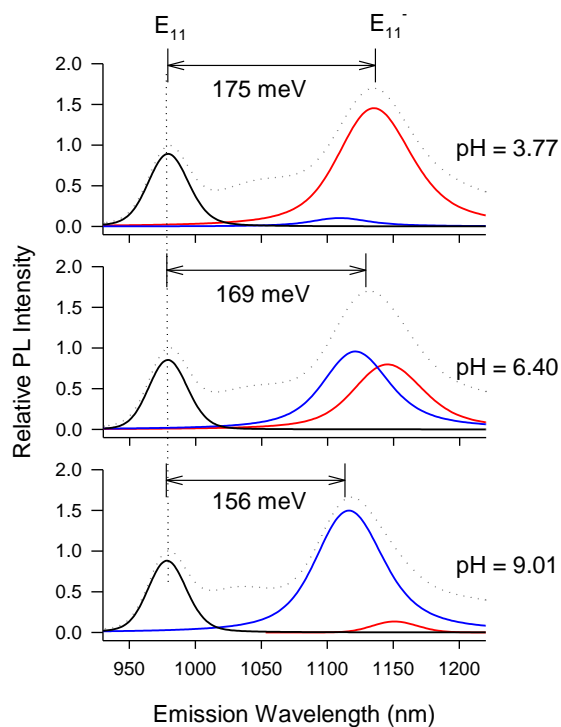


**Figure 3-5.** Defect PL of (6,5)-SWCNT- $C_6H_4N(CH_2CH_3)_2$  at different pH is a convolution of two states: protonated state (red) and deprotonated state (blue). The solid lines are fitted peaks and the dotted lines are the original data.

Control experiments with a series of para-substituted aryl functional groups confirm that only amine moieties show pronounced photoluminescence pH effects (Table 3-1). Identical pH-dependences are observed in both *N,N*-dimethylamino- and *N,N*-diethylaminobenzene functionalized SWCNTs. In contrast, other terminating moieties such as methoxy, bromo, and nitro, did not show pH-responsive  $E_{11}$  or  $E_{11}^-$  emission. This observation can be related to the electronic resonance and inductive effects of a substituent on the benzene ring, which is referred to as the Hammett constant ( $\sigma_p$ ). For the aryl group, the protonation of

amine to ammonium transitions the Hammett constant from -0.66 to +0.82<sup>80</sup>. This significant change in electronic withdrawing capability lowers the energy level of the lowest unoccupied molecular orbital (LUMO) resulting in a further redshifted defect emission peak. In addition, a linear relationship between the energy shift ( $E_{11}^- - E_{11}^+$ ) and the Hammett constant is consistent with our previous work<sup>25</sup>. In the case of SWCNT-C<sub>6</sub>H<sub>4</sub>COOH, no significant pH dependence was observed, which is understood by the much smaller Hammett constant difference of 0.43 between the protonated and de-protonated forms of carboxylic acid compared to ~1.50 in the case of the aminoaryl group.

**Table 3-1.** Defect photoluminescence of (6,5)-SWCNTs with various functional groups -ArX at different pH. The pH dependence is observed only in the aminobenzene functionalized (6,5)-SWCNTs.

(6,5)-ArX	$E_{11}^+$ (nm)	$E_{11}^-$ (nm)		$E_{11}^-$ shift (meV)
		pH 9.0	pH 4.0	
Pristine	971	-	-	-
-N(CH <sub>2</sub> CH <sub>3</sub> ) <sub>2</sub>	975	1116	1134	18
-N(CH <sub>3</sub> ) <sub>2</sub>	975	1116	1134	18
-OCH <sub>3</sub>	973	1116	1116	0
-COOH	976	1124	1124	0
-Br	973	1125	1125	0
-NO <sub>2</sub>	973	1137	1137	0
-3,5-NO <sub>2</sub>	973	1145	1145	0

The pH-responsive defect PL features a strong dependence on the chiral structure of SWCNTs (Fig. 3-6, 3-7 and Table 3-2). The optical response to pH

change (between pH 4.0 and pH 9.0) ranges from 18 to 33 meV for five different SWCNT chiralities with *N,N*-diethylaminobenzene functional groups. In both acidic and basic conditions, the defect PL shift shows a  $1/d^2$  dependence on the nanotube diameter  $d$ . In general, the smaller the diameter, the larger the pH response. Among the investigated species, the aminobenzene functionalized (8,3)-SWCNT has the highest energy shift (33 meV). This diameter dependence is evidence for the dark exciton brightening mechanism, which leads to the enhanced, red-shifted  $E_{11}^-$  photoluminescence.

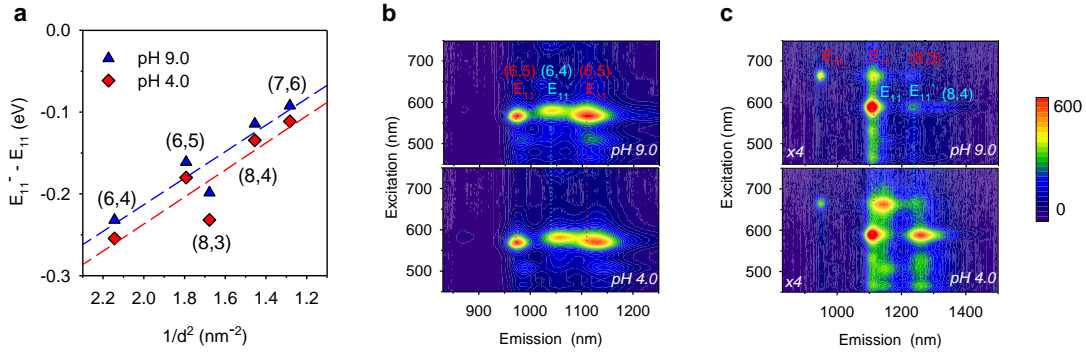


**Figure 3-6.** Chirality dependent pH response of *N,N*-diethylaminobenzene functionalized SWCNTs. **a**, The energy shifts between pH 9.0 and pH 4.0 ( $\Delta E$ ) vary from 18 to 33 meV depending on the nanotube chirality. Defect photoluminescence of **b**, (6,5)/(6,4)-SWCNT- $\text{C}_6\text{H}_4\text{N}(\text{CH}_2\text{CH}_3)_2$  and **c**, (8,3)/(8,4)-SWCNT- $\text{C}_6\text{H}_4\text{N}(\text{CH}_2\text{CH}_3)_2$ .

**Table 3-2.** Chirality-dependent pH response of SWCNT- $C_6H_4N(CH_2CH_3)_2$ .

chirality (n,m)	d (nm)	pH 9.0			pH 4.0			$\Delta E_{11'}$ (meV)
		$E_{11}$ (nm)	$E_{11'}$ (nm)	$E_{11'} - E_{11}$ (eV)	$E_{11}$ (nm)	$E_{11'}$ (nm)	$E_{11'} - E_{11}$ (eV)	
(6,4)	0.683	874	1045	-0.2321	874	1065	-0.2544	22
(6,5)	0.747	975	1117	-0.1620	975	1136	-0.1800	18
(8,3)	0.772	941	1108	-0.1986	941	1142	-0.2319	33
(8,4)	0.829	1107	1233	-0.1144	1107	1258	-0.1344	20
(7,6)	0.883	1126	1229	-0.0923	1124	1249	-0.1104	18

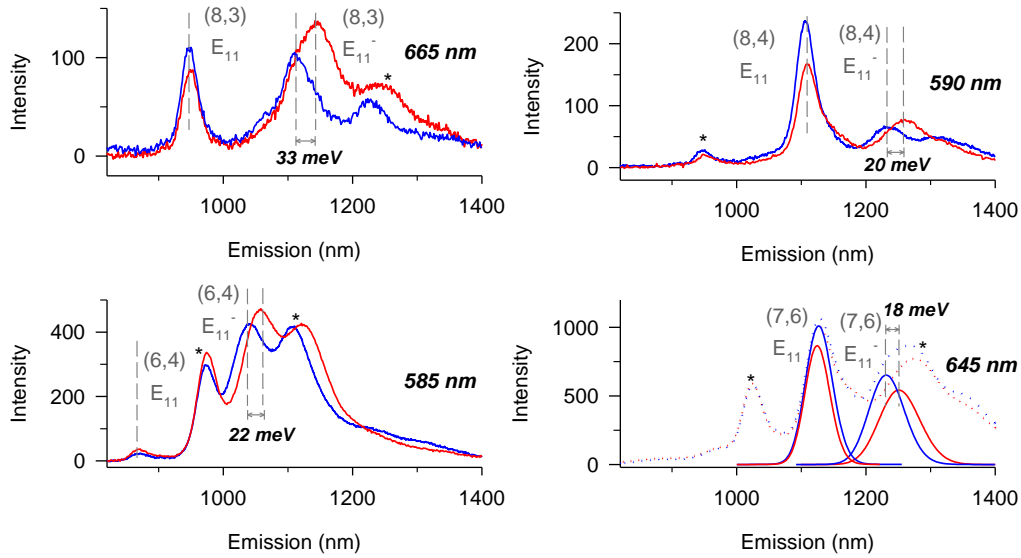


**Figure 3-7.** Chirality dependent pH response of  $N,N$ -diethylaminobenzene functionalized SWCNTs at  $E_{22}$  excitation.

### 3.3.2. Temperature-sensitive defect photoluminescence

Independent of pH-responsive energy shifts, the intensity of the defect PL exhibits a strong dependence on temperature (Fig. 3-8). Within a broad temperature range including the biological environment from 25 to 45 °C, the intensities of  $E_{11}^-$  and  $E_{11}$  are ruled by the statistically determined Boltzmann factor. Due to the finite well depth of the defect state, a trapped exciton can escape with the aid of thermal energy,  $k_B T$ , resulting in redistribution of the  $E_{11}^-$  and  $E_{11}$  exciton populations (Fig. 3-8b). The PL intensity ratio of  $E_{11}^-$  and  $E_{11}$  correlates directly with temperature as described by the van't Hoff equation:

$$\ln\left(\frac{I_{E_{11}}}{I_{E_{11}^-}}\right) = -\frac{\Delta E'}{k_B T} + C' \quad \text{eq (4)}$$

where  $I_{E_{11}}$  and  $I_{E_{11}^-}$  are the integrated PL intensities of the original and defect exciton emissions, respectively;  $\Delta E'$  is the potential well depth of the defect state;  $k_B$  is the Boltzmann constant;  $T$  is temperature; and  $C'$  is a constant.

By monitoring the photoluminescence of (6,5)-SWCNT- $C_6H_4N(CH_2CH_3)_2$  under constant pH while increasing temperature from 15 to 85 °C, we observed the temperature-responsive PL (Fig. 3-8c). We note that a different temperature calibration is required for each pH because the acid-base equilibrium of the amino moiety is temperature dependent. Although the original exciton PL ( $E_{11}$ ) from pristine SWCNTs can be responsive to temperature<sup>97</sup>, it is also susceptible to other environmental fluctuations. In contrast, the NIR  $E_{11}^-/E_{11}$  intensity ratio provides a reliable measurement of local temperature because both the probe ( $E_{11}^-$ ) and internal reference ( $E_{11}$ ) are maintained in the same chemical environment. It is a note that the temperature dependence of defect photoluminescence has been

previously reported by Ghosh *et al.*<sup>33</sup> However, to the best of our knowledge, this is the first report of an optical nanothermometer based on this phenomenon.

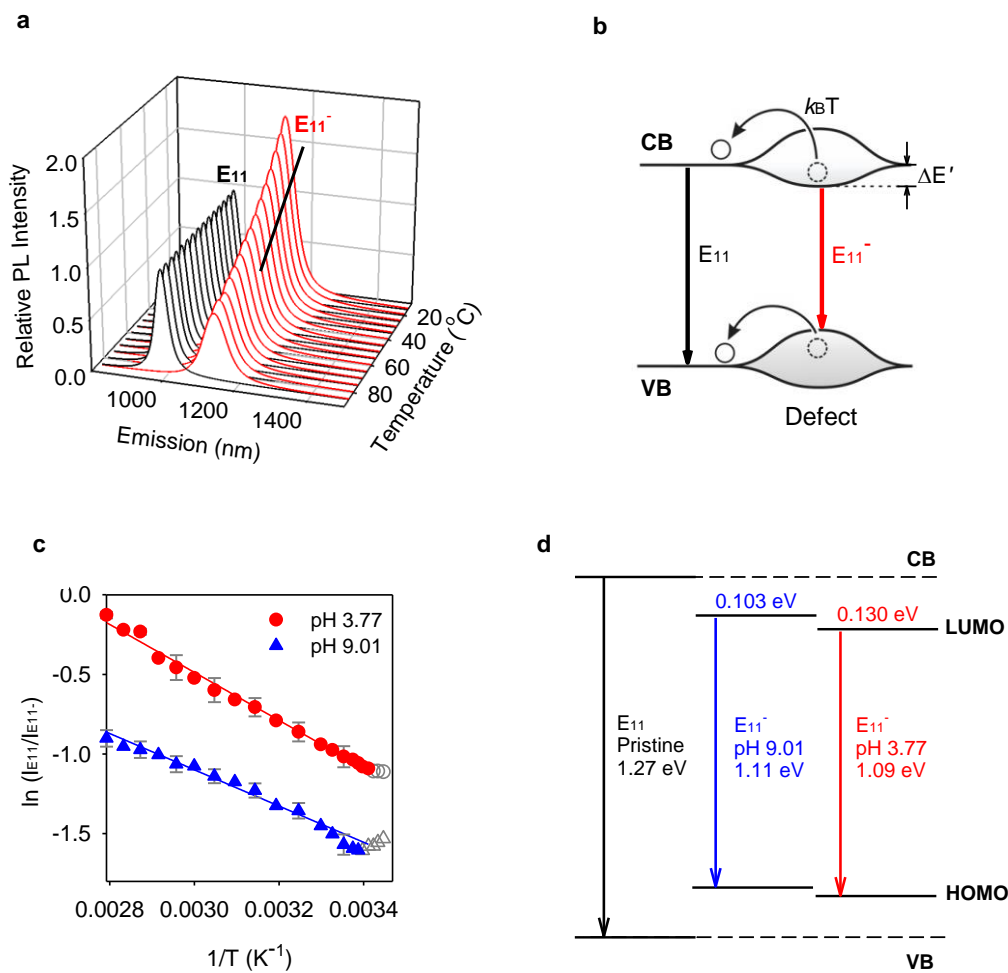


**Figure 3-8.** Temperature-dependent defect photoluminescence of (6,5)-SWCNT-C<sub>6</sub>H<sub>4</sub>N(CH<sub>2</sub>CH<sub>3</sub>)<sub>2</sub>. **a**, Evolution of E<sub>11</sub> and E<sub>11</sub><sup>-</sup> PL from protonated (6,5)-SWCNT-C<sub>6</sub>H<sub>4</sub>N(CH<sub>2</sub>CH<sub>3</sub>)<sub>2</sub> with increasing temperature at pH 3.77. **b**, Schematic illustration of thermal promotion of an exciton from the defect state (E<sub>11</sub><sup>-</sup>) to the higher E<sub>11</sub> state. The relative exciton population is correlated with the relative energy of the defect states. **c**, The van't Hoff plots (the E<sub>11</sub>/E<sub>11</sub><sup>-</sup> integrated intensity ratios as a function of temperature) at pH 3.77 (red) and pH 9.01 (blue). The slope of linear regression is used to determine the relative E<sub>11</sub><sup>-</sup>

energy between the protonated and de-protonated states of the aminobenzene substituents. **d**, Simplified energy diagram of (6,5)-SWCNT-C<sub>6</sub>H<sub>4</sub>N(CH<sub>2</sub>CH<sub>3</sub>)<sub>2</sub> at pH 3.77 and pH 9.01.

Furthermore, from the evolving intensity ratio of E<sub>11</sub>/E<sub>11</sub><sup>-</sup> over temperature, we have constructed the van't Hoff plots (Fig. 3-8d) to extract the potential well depth ( $\Delta E'$ ) of the defect state, as described previously by Ghosh *et al.*<sup>33</sup> This well depth is directly related to the energy difference between the LUMOs of E<sub>11</sub> and E<sub>11</sub><sup>-</sup>. From the van't Hoff plots of aminoaryl (6,5)-SWCNTs, we derived a well depth of 103 meV for the de-protonated form and 130 meV for the protonated form. The difference, 27 meV, is 9 meV larger than the corresponding PL emission shift. This difference may be attributed to an asymmetric effect of protonation on the energy levels of LUMO and HOMO, as illustrated in Fig. 3-8d. Importantly, the ammonium groups (HR<sub>2</sub>N<sup>+</sup>), with a Hammett constant of  $\sim +0.82$ , have a deep potential well of 130 meV, which is comparable to our experiments with nitro groups ( $\sigma_p \sim 0.778$ ,  $\Delta E' \approx 138$  meV). This result confirms that the pH dependence arises from energy modulation of the defect state through changes in the local environment of covalently attached aminoaryl groups.

### 3.3.3. Properties of defect photoluminescence toward biological applications

To illustrate the practical prospect of the observed phenomenon as optical pH sensors, we measured the pH of 10% v/v fetal bovine serum in Dulbecco's Modified Eagle's medium using *N,N*-diethylaminobenzene-(6,5)-SWCNTs (Fig. 3-

9). We found that the optically measured pH values are in good agreement with readings from a pH meter. Previous works by Dai *et al.*<sup>98</sup>, Strano *et al.*<sup>99</sup> and others<sup>100</sup> suggest that SDS can be replaced with a bio-friendly molecule such as phospholipid-polyethylene glycol (PL-PEG) and Pluronic F68 (PF68). Conveniently, this defect PL probe can be excited by both visible (though  $E_{22}$  excitation) or the near-IR (through  $E_{11}$  excitation), as we have shown previously,<sup>34</sup> to yield  $E_{11}^-$  PL in NIR-II that reduces auto-fluorescence and photo damage.

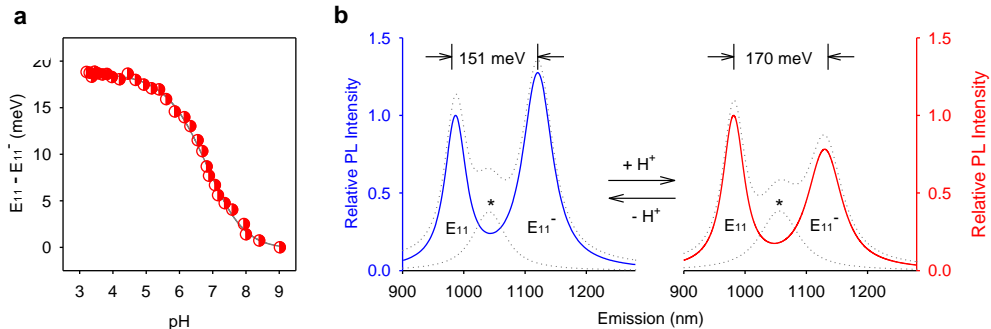


**Figure 3-9.** pH measurement in biological media through defect photoluminescence. **a**, The relative PL energy shift of  $E_{11}$  and  $E_{11}^-$  as a function of pH. **b**, The pH of 10% v/v fetal bovine serum in DMEM is measured optically with (6,5)-SWCNT- $C_6H_4N(CH_2CH_3)_2$ . The PL shift between pH 3.7 (blue) and 9.0 (red) in the biological media is identical to that obtained from aqueous solutions. The excitation wavelength is 565 nm.

Importantly, our bi-functional nanosensor measures pH by the energy difference between the probe ( $E_{11}^-$ ) and an internal reference ( $E_{11}$ ) (Fig. 3-10). This sensing mechanism is distinctly different from all previous nanotube-based optical sensors, which is based on photoluminescence quenching of  $E_{11}$ . From a previous

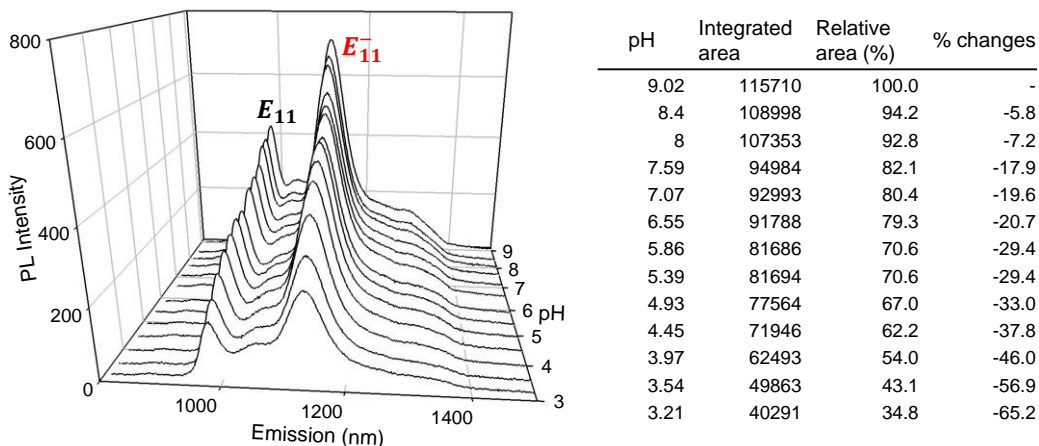


**Figure 3-10.** The PL intensity of (6,5)-SWCNT- $C_6H_4N(CH_2CH_3)_2$  as a function of pH. All emission spectra were taken at 565 nm under identical spectral conditions. Integrated area is the sum of both  $E_{11}$  and  $E_{11}^-$ . The full width at half maximum barely changed across the pH 3-9 range, with a FWHM of  $40.6 \pm 3$  nm for  $E_{11}$  and  $82.9 \pm 3$  nm for  $E_{11}^-$ , respectively.

work by Strano *et al.*,<sup>101</sup> the  $E_{11}$  absorption and photoluminescence becomes diminishing at low pH. We note that in the case of aminoaryl-SWCNTs, the PL intensity dropped by 33% when the pH decreased from 9.02 to 4.93, as shown in Fig. 3-10. However, the PL intensity is adequately strong for the proposed sensing applications and can even more stable over a wide pH range by replacing SDS with other surfactants as suggested by Duque *et al.*<sup>101</sup> The photoluminescence intensity of  $E_{11}$  can also be influenced by the surrounding environment such as salts and surfactants<sup>102-106</sup>. Salts can modify surfactant wrapping resulting in change in  $E_{11}$  PL intensity, as previously reported by Ziegler *et al.*<sup>103</sup>. and Doorn *et al.*<sup>104</sup> The PL intensity of  $E_{11}$  tends to decrease at high salt concentrations ( $> 450$  mM). However, this salt influence becomes intrinsically irrelevant here, again, because the pH is

measured from the energy difference between  $E_{11}$  and  $E_{11}^-$ , not the intensity. The photoluminescence intensity becomes a concern only when the signal is too weak. For aminoaryl-(6,5), only when the salt concentration exceeds 300 mM, the drop in PL intensity becomes more substantial (by 55% at pH 5.5 and ~67% at pH 9.0). However, even under the salt level of serum (135 - 145 mEq/L), the pH-dependent energy shift from the fluorescent nanoprobe agrees well with the pH meter (Fig. 3-11).

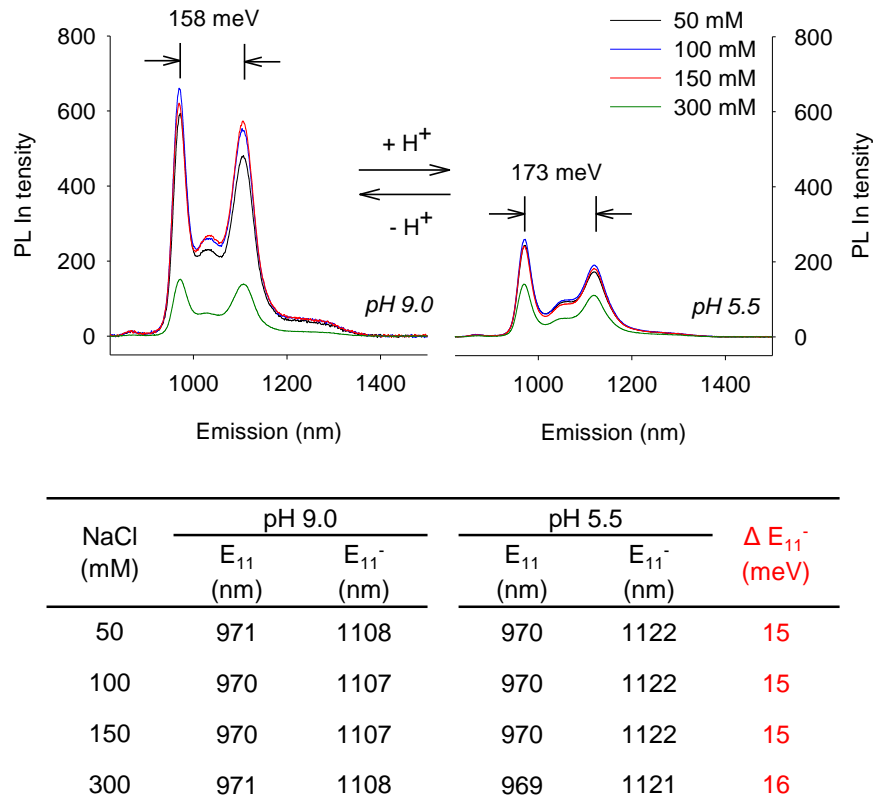


**Figure 3-11.** Salt effects on pH response of defect photoluminescence with (6,5)-SWCNT- $C_6H_4N(CH_2CH_3)_2$ . All emission spectra were taken at 565 nm under identical spectral conditions.

### **3.4. Conclusions**

In Chapter 3, we show that protonation of covalently attached aminoaryl groups on semiconducting carbon nanotubes can be probed by pH-dependent defect photoluminescence. Switching between the protonated and de-protonated states of the amino moiety significantly modifies the defect state of the covalently functionalized SWCNTs, producing energy shifts as large as 33 meV. This novel defect sensor responds sensitively and selectively to pH changes as small as 0.2 pH units over a wide working window (pH 4.5 to 8.5) that fully covers the pH range of typical biological fluids. Compared to ultra-pH-sensitive nanoparticles, which are based on pH-responsive self-assembly of fluorescent and quenching building blocks, our nanoprobe does not require a library of nanoparticles to cover the biologically relevant range of pH, which may be advantageous for high resolution imaging. Our experiments further uncover a strong temperature dependence of the defect photoluminescence that correlates the relative  $E_{11}^-/E_{11}$  population with temperature by the van't Hoff equation as a tool for optical probing. Based on these findings, the first bi-functional optical nanoprobe is proposed to offer simultaneous pH and temperature sensing capabilities with a built-in reference. Featuring a unique combination of high photostability, high sensitivity, high selectivity, wide working window, nanoscale size, and inherently low background of NIR-II photoluminescence, this novel nanoprobe may find applications in chemical imaging, biosensing and chemo-photothermal therapy at the cellular and even molecular levels.

# Chapter 4 . Brightening of Carbon Nanotube Trion through Fluorescent Quantum Defects

## 4.1. Introduction

Trions play a critical role in semiconducting materials not only in understanding of their optical and electrical properties including dark exciton states and many-body correlations, but also for future nanoscale optoelectronic applications such as solar cells and single photon emitting sources<sup>38, 39, 50, 51</sup>. A trion is composed of two electrons and a hole (e-h-e) or two holes and an electron (h-e-h), which is conceptually analogous to the hydrogen ions ( $H^-$  and  $H_2^+$ ). The concept of trion was theoretically suggested by Lampert in 1958<sup>42</sup>, but had not been experimentally identified for several decades due to the negligible binding energies of the three particles in bulk materials. With the development of nanomaterials including quantum wells (QW), and quantum dots (QD), trions have been experimentally observed under sufficiently low temperatures (4 - 5 K), high magnetic fields (40 -500 mT) and high excitation densities ( $\sim 20 \text{ mW/cm}^2$ )<sup>43, 53, 107, 108</sup>.

In the case of semiconducting single-walled carbon nanotubes (SWCNTs), the significantly enhanced exciton binding energies in quasi one-dimensional (1D) structure makes trions detectable at room temperature<sup>44-46</sup>. Carbon nanotube trions are generated by hole doping, high power laser excitation, or under electrically activated conditions<sup>44-46, 57, 109, 110</sup>. A variety of spectroscopic techniques have been used to identify trions including photoluminescence (PL), electroluminescence

(EL), transient absorption (TA), and time-resolved PL spectroscopy. Unfortunately, the trion PL is far weaker than that of nanotube excitons. Interestingly, Brozena *et al.* has previously reported an efficient method for formation of defect-bounded trions in SWCNTs<sup>57</sup>. Observed trion PL is as bright as the native E<sub>11</sub> emission because the trion is bound by alkyl defects. However, the Billups-Birch reduction that is used for the defect introduction occurs in liquid ammonia at -78 °C, which hampers *in situ* monitoring of PL evolution, and the PL quantum yield of these trions remains low.

Here, we report defect-induced trion PL brightening in semiconducting SWCNTs that are chemically tailored with a series of molecularly tunable fluorescent alkyl quantum defects. Our novel alkylation chemistry occurs in aqueous solution, making it possible to monitor *in situ* the evolution of trion photoluminescence. The trion PL is ultra-bright even at room temperature, affording a collective quantum yield 18-fold higher than the native exciton PL from unfunctionalized SWCNTs. The fluorescent quantum defects in (6,5)-SWCNTs-C<sub>6</sub>H<sub>13</sub> produce two new redshifted peaks at 135 meV and 258 meV from the parent nanotube PL (E<sub>11</sub>). The first peak originates from defect bound excitonic states (E<sub>11</sub><sup>-</sup>), as previously reported by our team (see Chapter 2) and the second peak is identified as PL from a defect-bound trion (E<sub>T</sub>). The defect-bound trions exhibit 24 meV tunability in the second near-infrared window and the band depends linearly on defect density. Furthermore, the E<sub>T</sub> PL shows a weaker temperature dependence when compared to E<sub>11</sub><sup>-</sup>, suggesting the localized nature of defect-bound trions. This

study marks a significant step in the creation and photophysics of defect-bound trions.

## **4.2. Experimental methods**

### 4.2.1. Preparation of SWCNT solutions for trion photoluminescence

HiPco SWCNTs (Rice University, batch # 194.3) were stabilized by 1 wt.% sodium dodecyl sulfate (Sigma Aldrich,  $\geq 98.5$  %) in D<sub>2</sub>O (Cambridge Isotope Laboratories, Inc., 99.8%) by tip ultrasonication (Misonix) at 35 W, 10 °C in a stainless steel beaker for 2 hours, followed by ultracentrifugation with an Optima LE-80K Ultracentrifuge (Beckman Coulter) at 170,499g for 4 hours. The top three fourths of the supernatant was carefully transferred and used for subsequent reactions. Chirality-enriched SWCNT samples were prepared by gel chromatography using Sephacryl™ S-200 high resolution chromatography resin (GE Healthcare)<sup>60</sup>. The concentration of chirality-enriched solutions was calculated based on the extinction coefficient previously determined by Zheng *et al.*<sup>74</sup>.

In general, sodium bicarbonate (EMP chemicals, ACS grade, 4 mol. eq. to SWCNT carbon atoms), acetonitrile (TCL, 99.8%, 0.1 mol. eq.) and various alkyl/aryl halides (Sigma Aldrich, 4 mol. eq.) were added sequentially to each SWCNT solution, which was kept in a capped glass vial covered by aluminum foil to avoid light. Acetonitrile was used as a co-solvent for alkyl halide. Sodium dithionite (Sigma Aldrich, 85%, 4 mol. eq.) was then added to the mixture and stirred with a magnetic stirring rod at room temperature. To increase the degree of

functionalization, the amounts of reagents were increased proportionally to the concentration of SWCNTs.

#### 4.2.2. Optical probing of pH- and temperature-response in trion PL

To monitor the temperature response of trions, the functionalized-SWCNT solution was heated from 15 °C to 85 °C using a circulating water bath while the photoluminescence spectra were obtained at 5 °C increments. The solution temperature was measured with the Surface Temperature Sensor and LabQuest 2 software (Vernier). The PL peaks of E<sub>11</sub> and E<sub>11</sub><sup>-</sup> were fit with Voigt line shapes using Peakfit v4.12 (SeaSolve) software, and then the integrated peak areas were plotted as a function of temperature.

The solution pH was adjusted by adding small aliquots of 0.02 M HCl or NaHCO<sub>3</sub> solutions (Sigma Aldrich) in the range from 3.0 to 8.5. The pH was determined using a pH meter (Accumet™ AB15+ Basic and BioBasic pH meters and Accumet™ pH/ATC electrodes, Fisher Scientific).

#### 4.2.3. Calculation of defect photoluminescence brightening

The relative PL quantum yield of E<sub>11</sub> was calculated using the following equations:

$$\Phi_{CNT,E11^-} = \frac{I_{E11^-}}{I_{E11}} \frac{Abs_{E22}}{Abs^*_{E22}}$$

$$\Phi_{CNT,ET} = \frac{I_{ET}}{I_{E11}} \frac{Abs_{E22}}{Abs^*_{E22}}$$

$\Phi_{\text{CNT}}$ : relative quantum yield of SWCNTs in 1 wt.% SDS/D<sub>2</sub>O solution  
 $I_{\text{E}_{11}^-}$ : integrated emission intensity of *f*-SWCNT solution after reaction for E<sub>11</sub><sup>-</sup>.  
 $I_{\text{E}_{\text{T}}}$ : integrated emission intensity of *f*-SWCNT solution after reaction for E<sub>T</sub>.  
 $I_{\text{E}_{11}}$ : integrated emission intensity of pristine SWCNT solution.  
 $Ab_{\text{S}^* \text{E}_{22}}$ : absorbance of *f*-SWCNT solution at the excitation wavelength.  
 $Ab_{\text{S} \text{E}_{22}}$ : absorbance of pristine SWCNT solution at the excitation wavelength.

Absorption and photoluminescence were fitted with Voigt functions using PeakFit software v4.12. No baseline correction was applied during the fitting for PL while a linear background correction was used for the E<sub>22</sub> absorption.

### **4.3. Results and discussion**

#### 4.3.1. Trion photoluminescence through alkyl defects

Individual (6,5)-SWCNTs stabilized in D<sub>2</sub>O by 1 wt.% sodium dodecyl sulfate were functionalized with hexyl iodide (C<sub>6</sub>H<sub>13</sub>I) in the presence of sodium dithionite (Na<sub>2</sub>S<sub>2</sub>O<sub>4</sub>), sodium bicarbonate (NaHCO<sub>3</sub>), and acetonitrile (CH<sub>3</sub>CN) (Fig. 4-1), as described in Chapter 2. The hexyl group-attached SWCNTs create a new defect PL (E<sub>11</sub><sup>-</sup>) at 1095 nm, redshifted by 135 meV from the original excitonic transition (E<sub>11</sub>, 980 nm). In addition, a new redshifted peak (E<sub>T</sub>) appears at 1226 nm (redshifted by 258 meV). Surprisingly, E<sub>11</sub><sup>-</sup> PL is 8-fold brighter than E<sub>11</sub>, while E<sub>T</sub> is 10-fold brighter.

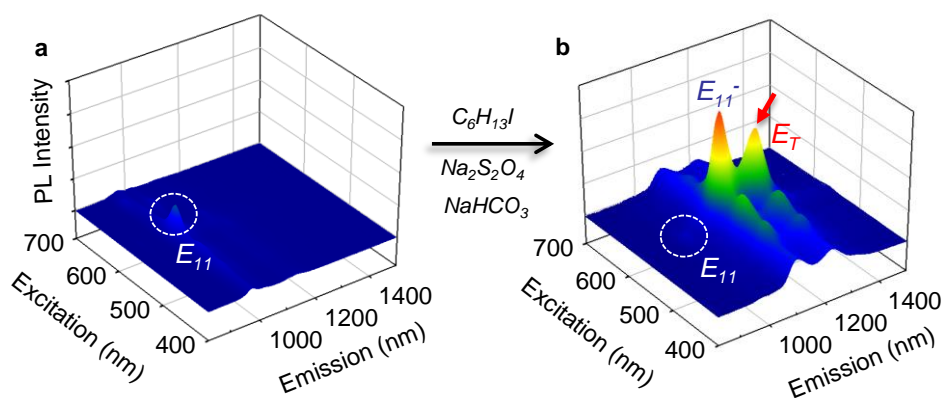


**Figure 4-1.** Defect-bound triions developed by the new alkylation method. The 3D PL maps of **a**, pristine (6,5)-SWCNTs and **b**, the hexyl functionalized (6,5)-SWCNTs. The new PL features at 1095 nm and 1225 nm are assigned to  $E_{11}^-$  and  $E_T$ , respectively. The defect PL shows a collective quantum yield 18-fold higher than that of the unfunctionalized SWCNTs.

In the absence of defects, a carbon nanotube exciton can diffuse along the tubular axis until recombination as shown in Fig. 4-2a. The extremely low quantum yield (QY, 0.1 – 7 %) <sup>28</sup> of SWCNTs is closely related to low lying dark states. In stark contrast to triions in pristine SWCNTs, our aqueous alkyl-functionalized SWCNTs show the surprisingly bright PL from both  $E_{11}^-$  and triion PL ( $E_T$ ). It is hypothesized that trapping of an exciton and an electron to the same defect site to produce a triion (Fig. 4-2b). The large redshift of triion PL suggests the energy level of the defect-bound triion is located below the dark excitons.

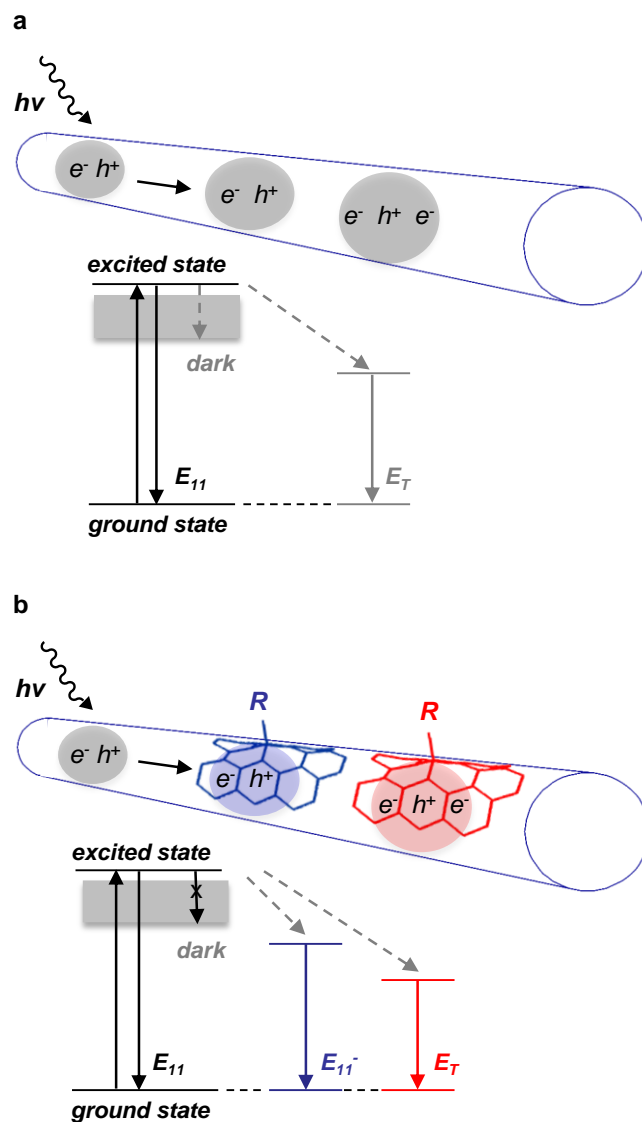


**Figure 4-2.** Schematic energy diagram of exciton and trions in a semiconducting SWCNT. **a**, An exciton diffuses along a unfunctionalized SWCNT followed by non-radiative (dark) and radiative ( $E_{11}$ ) or trion ( $E_T$ ) pathway. **b**, In a functionalized SWCNT, the  $sp^3$  defect centers act as an exciton trap to harvest dark excitons resulting in brightening of both  $E_{11}'$  and  $E_T$ .

The evolution of PL features  $E_{11}$ ,  $E_{11}'$  and  $E_T$  are monitored *in situ* upon excitation of (6,5)-SWCNTs at  $E_{22}$ . A hexyl functional group is chosen as a

fluorescent quantum defect because it has the brightest  $E_T$  emission among all other functional groups measured in this study. In Fig. 4-3, we illustrate the effect of incorporated defects by changing the molar ratio of carbon to hexyl iodide, ([C]:[RX]) from 0.06 to 4.00 while all the other reagents are kept identical. The  $E_{11}$  emission peak decreased with increasing defect density. For the  $E_{11}^-$ , it is enhanced and maximized when the molar ratio of reactants, [C]:[RX] is 1:0.1. More importantly, the relative intensity of  $E_T$  steadily increased with the defect density (Fig. 4-3d and 4-4e).

We further evaluate the dependence of defect density with correlated PL, UV-Vis-NIR absorption, and Raman spectra (Fig. 4-4). The decrease in  $E_{11}$  absorption is correlated with increased Raman D mode at  $1305\text{ cm}^{-1}$ , which consistently supports the covalent attachment of hexyl groups (Fig. 4-4c and 4-4d). Notably, the relative intensity of trion PL (scaled by  $E_{11}$  PL intensity) exponentially increases with the Raman D/G ratio (Fig. 4-5).

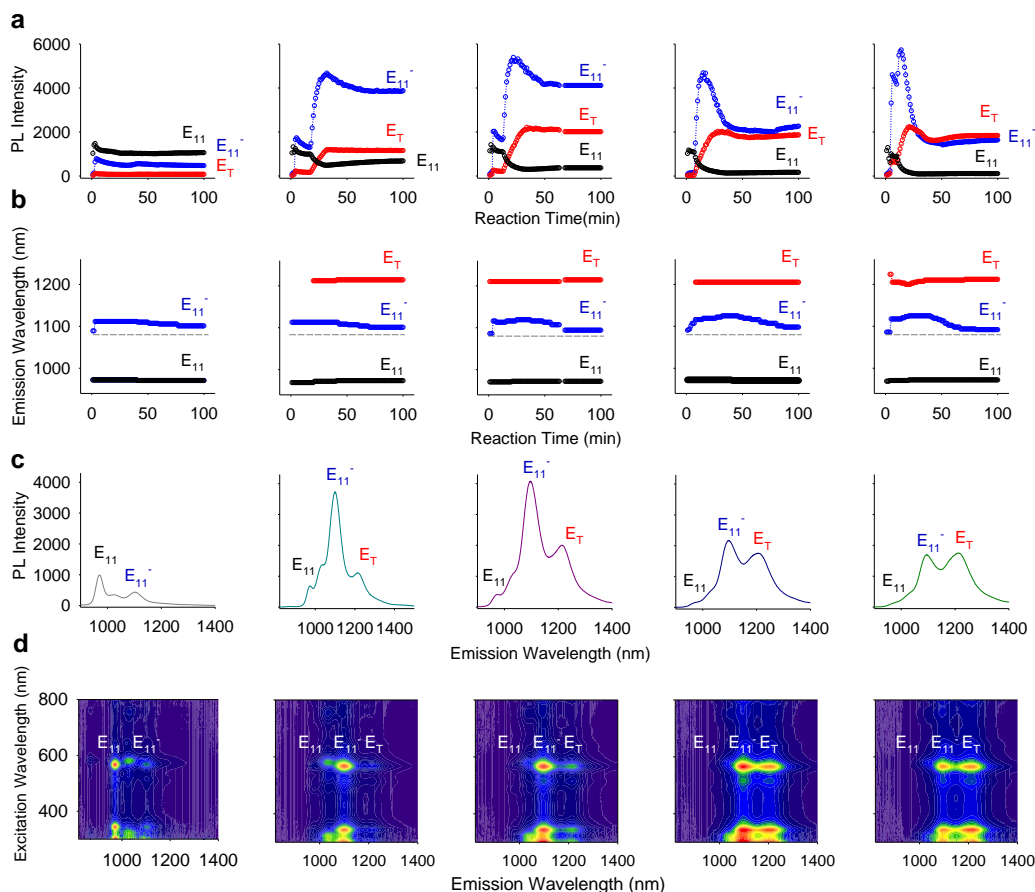


**Figure 4-3.** Evolution of defect PL monitored with *in situ* photoluminescence spectroscopy. **a**, The PL intensity of  $E_{11}$ ,  $E_{11}^-$  and  $E_T$  as a function of reaction time. The emission spectra of (6,5)-SWCNT are obtained with 565 nm single excitation. The intensity of trion photoluminescence increases with the relative RX concentration while the intensity of  $E_{11}^-$  PL reached the maxima at [C]:[C<sub>6</sub>H<sub>13</sub>I] = 1:0.10. **b**, The  $E_{11}$ ,  $E_{11}^-$  and  $E_T$  emission wavelength as a function of reaction time. **c**, The emission spectra when excited at 565 nm and **d**, 3D PL maps after 2 hours. The concentration of [C]:[C<sub>6</sub>H<sub>13</sub>I] is 0.06, 0.07, 0.10, 0.70, and 4.00 from left to right.

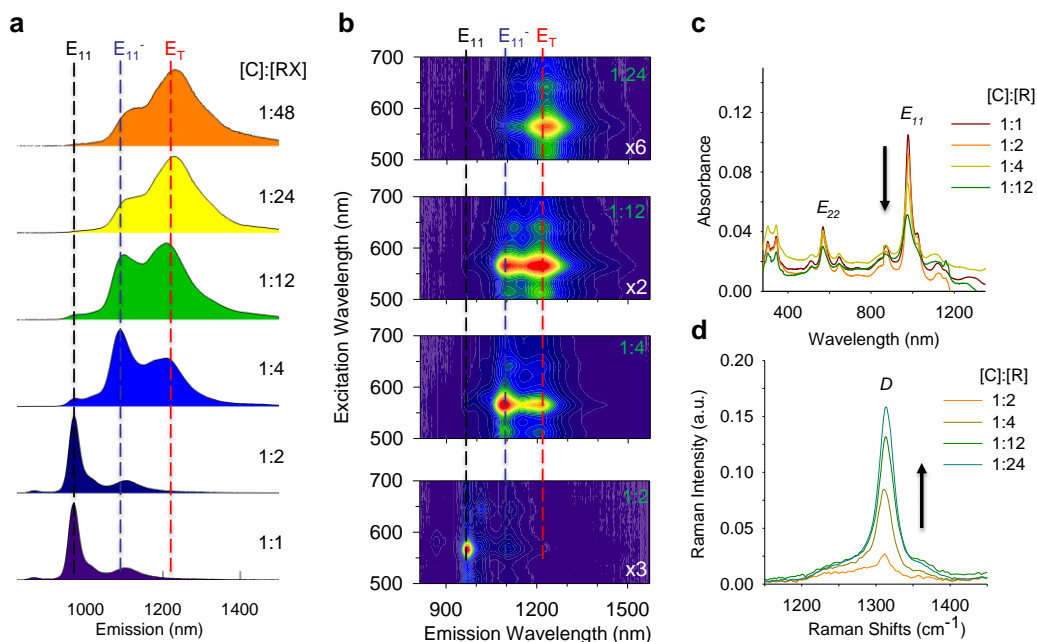


**Figure 4-4.** Covalent functionalization of (6,5)-SWCNTs- $C_6H_{13}$  produce controlled defect photoluminescence. **a**, 565 nm emission spectra, **b**, 3D excitation-emission contour maps **c**, UV-Vis-NIR absorption spectra, and **d**, Raman spectra at 532 nm excitation laser of (6,5)-enriched SWCNTs functionalized with  $C_6H_{13}$  at different concentrations, where [C]:[RX] is 1, 2, 4, 12, 24, and 48.

We note that brightening of defect photoluminescence does not originate from a reducing agent (sodium dithionite) itself. As reported by Lee *et al.*<sup>31</sup>, a reducing agent can increase the  $E_{11}$  PL quantum yield of unfunctionalized carbon nanotubes. However, this brightening effect is transient (a few minutes) and more importantly it does not create new defect PL features as observed in our fluorescent quantum defect systems (see Fig. 2-3 in Chapter 2).

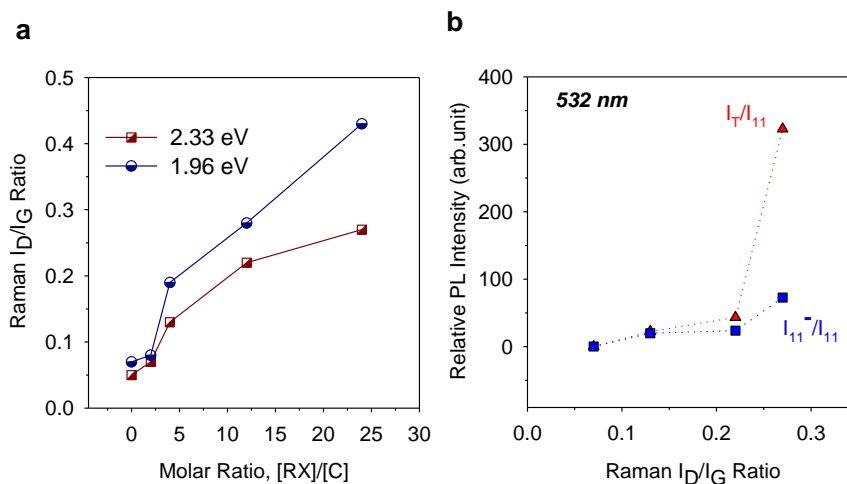


**Figure 4-5.** Trion formation in (6,5)-SWCNT- $C_6H_{13}$  strongly depends on defect density. **a**, Raman  $I_D/I_G$  ratio as a function of molar ratio of  $[RX]/[C]$ . As the concentration of reagents increase, the D mode in Raman is enhanced for both 2.33 eV and 1.96 eV excitation laser. **b**, Relative PL intensity over Raman  $I_D/I_G$  ratio.

The trion PL shows a strong dependence on nanotube diameter, which is indicative of a correlation with dark excitons (Fig. 4-6 and Table 4-1). The defect PL peaks including  $E_{11}^-$  and  $E_T$  follows similar trends of diameter-dependence with respect to dark excitons in pristine SWCNTs predicted by Louie *et al*<sup>78</sup> (Fig. 4-6a). Moreover, the  $(2n + m)$  family pattern shown in Fig. 4-6b matches those of free trions in unfunctionalized SWCNTs, although their emission energies are 23-100 meV smaller than our defect bound trions. The trion energy shifts as a function of nanotube diameter. Particularly, (6,4)-SWCNTs- $C_6H_{13}$  features an energy shift of 321 meV, which is the largest ever reported<sup>78</sup>. The diameter dependence follows that  $\Delta E^- = A * 1/d + B * 1/d^2$ , where  $\Delta E^- = E_{11}^- - E_T$ , A is related to the trion binding energy, and B is related to the exciton exchange term. In general, the exchange

energy ( $B$ ) can be regarded as the energy separation between triplet exciton states and singlet states and is typically in the range of 48-70 meV. However, for our trions,  $B$  is  $170 \text{ meV nm}^2$ , much larger than those from unfunctionalized SWCNTs<sup>42-44</sup>. This is understood as a result of large splitting between bright singlet and defect states, and thus larger energy shifts for both defect-bound excitons ( $E_{11}^-$ ) and trions ( $E_T$ ).

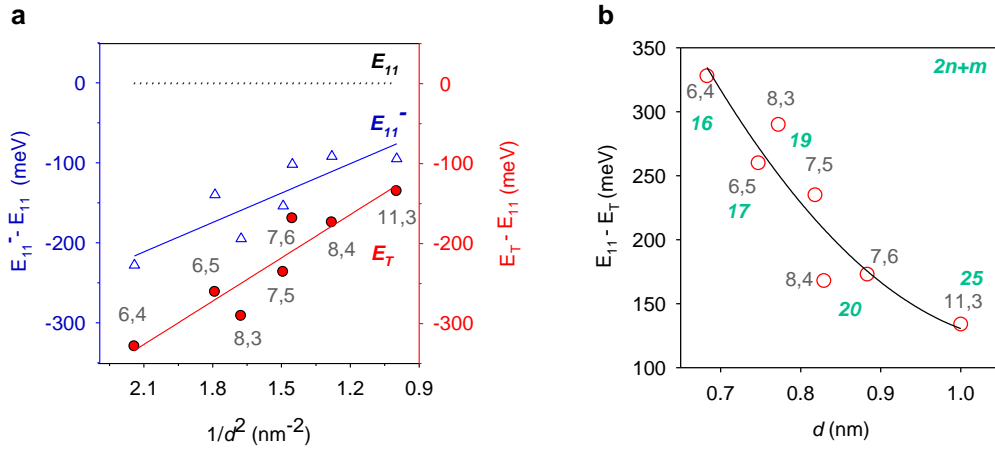


**Figure 4-6.** Chirality dependence of  $E_{11}^-$  and  $E_T$  with hexyl-functionalized SWCNTs. **a**, Both  $E_{11}^-$  (blue triangle) and  $E_T$  (red circle) energy shifts show a strong chirality dependence with respect to dark exciton brightening. **b**,  $E_T$  energy shift as a function of diameter. This further supports  $(2n + m)$  family pattern which is consistent with previously reported trions in unfunctionalized SWCNTs.

**Table 4-1.** PL results of trions from chirality-enriched SWCNTs, functionalized with C<sub>6</sub>H<sub>13</sub>I. Both E<sub>11</sub><sup>-</sup> and E<sub>T</sub> energy shifts are clearly resolved in each PL peak.

(n,m)	d (nm)	E <sub>11</sub> (nm)	E <sub>11</sub> <sup>-</sup> (nm)	E <sub>T</sub> (nm)	E <sub>11</sub> - E <sub>11</sub> <sup>-</sup> (meV)	E <sub>11</sub> - E <sub>T</sub> (meV)
(6,4)	0.683	879	1044	1138	223	321
(6,5)	0.747	982	1102	1229	138	254
(8,3)	0.772	960	1126	1231	190	284
(7,5)	0.818	1027	1174	1270	151	231
(8,4)	0.829	1117	1228	1316	100	168
(7,6)	0.883	1128	1228	1332	90	168
(11,3)	1.000	1207	1326	1386	92	133

To elucidate the nature of trions at defects, we analyzed the trion energy separation with different fluorescent quantum defects (Fig. 4-7 and Table 4-2). We observed functional group-dependent trion PL for (6,5)-SWCNTs-R, which is slightly tunable (24 meV), but less than one third of the E<sub>11</sub><sup>-</sup> tunability (61 meV). The strong electronic inductive effects of alkyl groups can push down the energy level of E<sub>11</sub><sup>-</sup>, resulting in a large energy separation for defect-bound trions (E<sub>T</sub>). This is in contrast to the defect-bound trions created through the Billups Birch reduction<sup>57</sup>, where trion PL is independent of the alkyl functional groups. The discrepancy can be explained by the similar electronic effects of alkyl groups used in that study (-C<sub>5</sub>H<sub>10</sub>-CH<sub>3</sub>, -C<sub>5</sub>H<sub>10</sub>COOH, and -C<sub>5</sub>H<sub>10</sub>NH<sub>2</sub>), which make negligible inductive effect differences resulting in similar defect PL. In addition to energy separation, we observed that the intensity of trion PL also depends on fluorescent quantum defects. Even though perfluorinated hexyl groups induce high energy

separation for trions (277 meV for (6,5)-SWCNTs), the  $E_T$  intensity is less bright compared to non-fluorinated hexyl-(6,5)-SWCNTs.

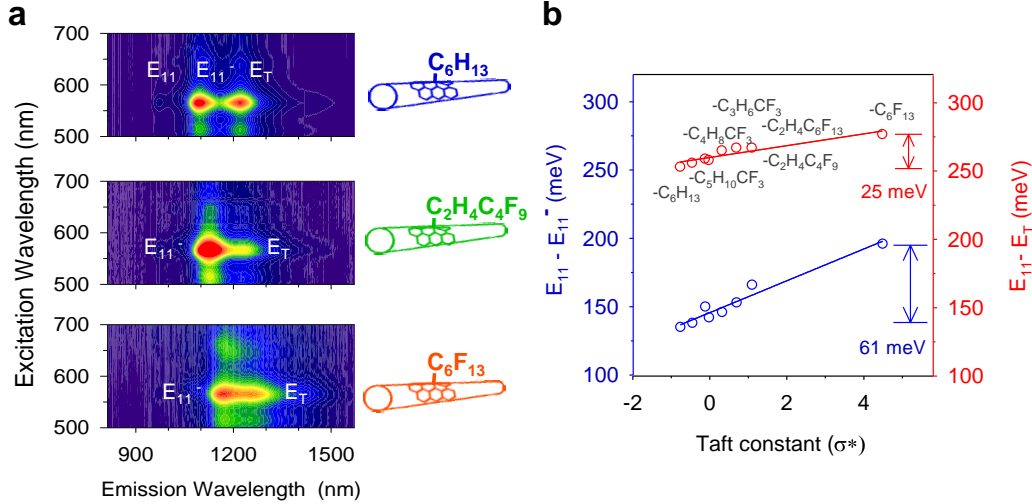


**Figure 4-7.** Functional group dependence of  $E_{11}^-$  and  $E_T$  in (6,5)-SWCNTs. **a**, PL maps of (6,5)-SWCNTs with non- ( $-C_6H_{13}$ ), partially- ( $-C_2H_4C_4F_9$ ), and perfluorinated hexyl ( $-C_6F_{13}$ ) groups. **b**,  $E_{11}^-$  and  $E_T$  energy shifts Vs Taft constant( $\sigma^*$ ). Both defect PLs are clearly related to the Taft constants while  $E_T$  shows less dependence on electronic effects compared to  $E_{11}^-$ .

**Table 4-2.** PL results of (6,5)-SWCNT-trions with various functional groups.

(6,5)-SWCNT-R	$\sigma_{\text{calc}}$	$E_{11}$ (nm)	$E_{11}^-$ (nm)	$E_T$ (nm)	$E_{11}^- - E_{11}$ (meV)	$E_{11}^- - E_T$ (meV)	$E_{11}^- - E_T$ (meV)
$-(CF_2)_2(CF_2)_3CF_3$	4.4766	986	1168	1265	196	277	81
$-(CH_2)_2(CF_2)_3CF_3$	1.0858	984	1133	1248	166	267	101
$-(CH_2)_2CF_2CF_3$	0.6855	978	1112	1239	153	267	114
$-(CH_2)_4CF_2CF_3$	-0.127	980	1112	1232	150	259	109
$-(CH_2)_2CF_3$	0.310	980	1108	1240	146	265	119
$-(CH_2)_2CH_2CF_3$	-0.034	980	1104	1231	142	258	116
$-(CH_2)_2(CH_2)_3CF_3$	-0.462	980	1100	1229	138	256	118
$-(CH_2)_2(CH_2)_3CH_3$	-0.774	981	1098	1227	135	253	119

### 4.3.2. Temperature response of trion PL

Exciton characteristics at trap states are investigated by monitoring PL of (6,5)-SWCNT-C<sub>6</sub>H<sub>13</sub> as a function of temperature from 15 to 85 °C at 5 °C increments (Fig. 4-8). The overall PL intensity is decreased by 79 % as temperature increased to 85 °C due to thermal energy enhanced non-radiative pathways (Fig. 4-8a and 4-8b). We construct van't Hoff plots with the integrated PL intensity of E<sub>11</sub>, E<sub>11</sub><sup>-</sup> and E<sub>T</sub> (Fig. 4-8c and 4-8d). The potential well depth (or de-trapping energy ΔE) is estimated by the slope in the van't Hoff plot (Fig. 4-8c), which is 79.7 meV from integrated area ratio of E<sub>11</sub>/E<sub>11</sub><sup>-</sup>. By the aid of thermal energy (*kT*), the population of exciton is changed between defect bound exciton (E<sub>11</sub><sup>-</sup>) and delocalized exciton (E<sub>11</sub>). The trap depth measurement between two energy states, E<sub>11</sub> and E<sub>11</sub><sup>-</sup>, agree well with those of aryl defects reported in Chapter 3 and is consistent with previously reported alkyl functionalized SWCNTs by Billups Birch reduction<sup>57</sup>. However, the slope of E<sub>11</sub><sup>-</sup>/E<sub>T</sub> shows a positive value even though E<sub>T</sub> is supposed to be located below E<sub>11</sub><sup>-</sup>. This temperature response can be understood as the characteristic of strongly localized trions at defects where the dimensionality is reduced to nearly zero.

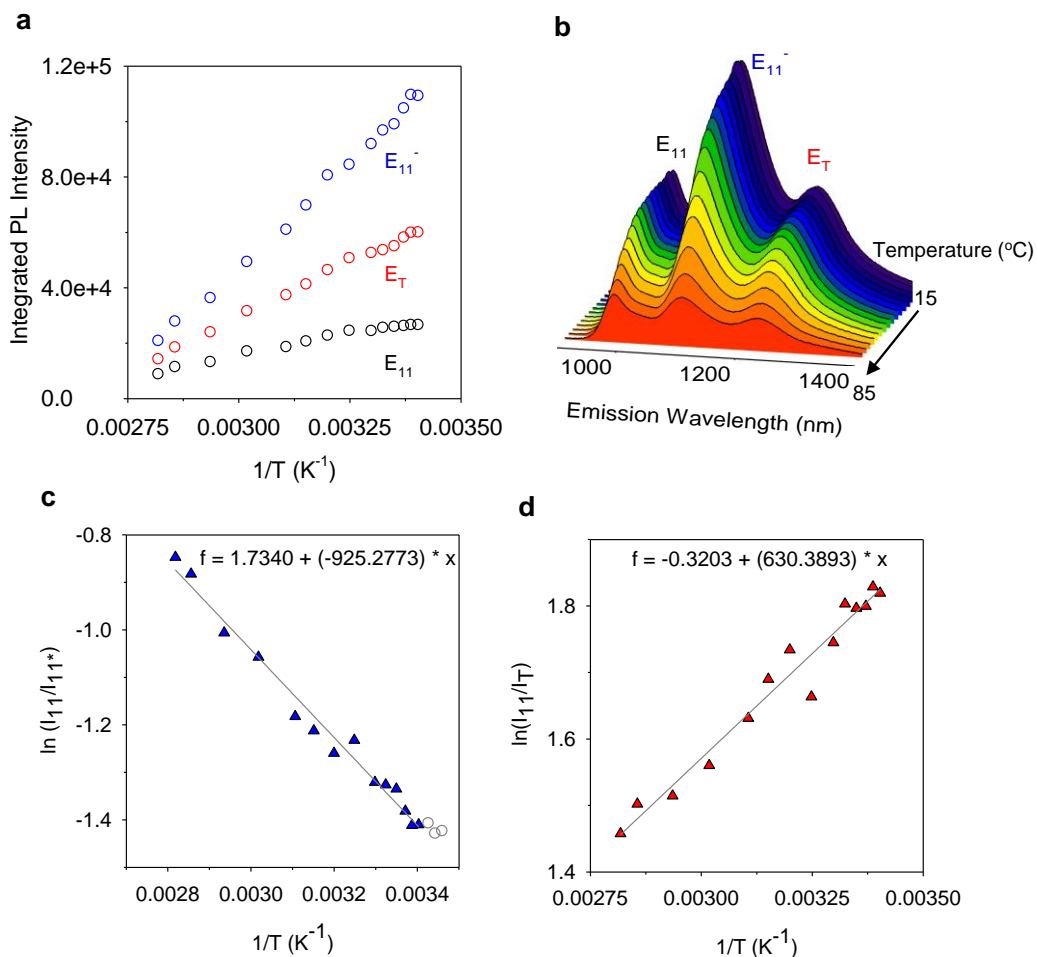


**Figure 4-8.** Temperature-dependence of  $E_{11^-}$  and  $E_T$  for (6,5)-SWCNTs-C<sub>6</sub>H<sub>13</sub>. **a**, Integrated PL intensity and **b**, 565 nm emission spectra as a function of temperature. The van't Hoff plots are constructed from integrated PL intensity of **c**,  $E_{11}/E_{11^-}$  and **d**,  $E_{11^-}/E_T$ .

#### 4.3.3. pH-dependence of trion photoluminescence

Notably, the relative intensity of  $E_T$  is more sensitively dependent on pH compared to  $E_{11}$  and  $E_{11^-}$  (Fig. 4-9). Since sodium dithionite is a mild reducing agent, we assume it forms a negative trion. Addition of hydrochloric acid (at aliquots of 0.02 M HCl) to the hexyl-functionalized SWCNT solution causes hole

doping of the nanotube and reduce the population of negative trions. The pH response of defect PL is reproducible and highly reversible.

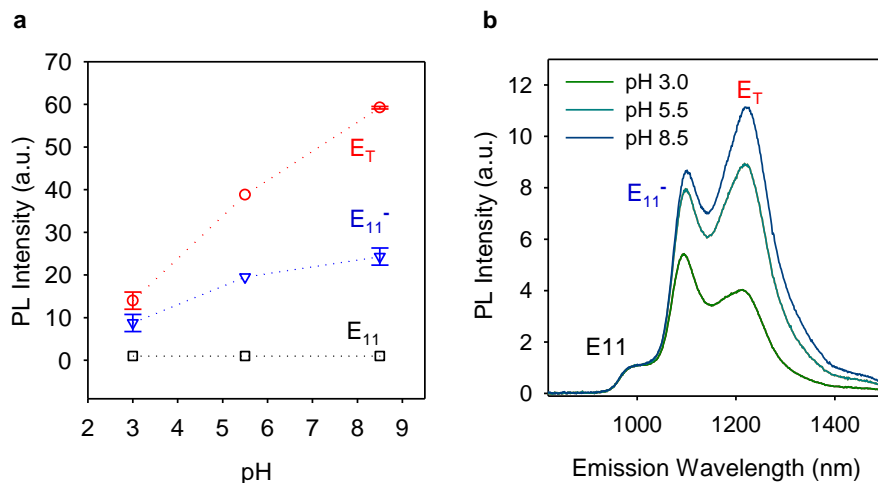


**Figure 4-9.** Trion intensity of (6,5)-SWCNT-C<sub>6</sub>H<sub>13</sub> strongly depends on solution pH. **a**, Integrated PL intensity as a function of pH. **b**, 565nm emission spectra under different pH. pH dependence is reproducible and reversible from acidic to basic, or vice versa.

#### 4.4. Conclusions

We demonstrated ultrabright trion photoluminescence in SWCNTs in the presence of alkyl fluorescent quantum defects introduced through alkyl halide precursors. PL from the defect-bound trion is more than an order of magnitude brighter than the native exciton in the parent nanotubes. The trion PL is redshifted by as much as 321 meV from that of native excitons and is strongly dependent on both nanotube chirality and the chemical nature of defects. The observed brightening and chirality dependence are suggestive of defect-bound trions and the

harvesting of dark excitons. Temperature-dependence studies indicate the localization of trions at a deep potential trap.

## Chapter 5. Summary and Outlook

### 5.1. Summary

This thesis demonstrates exciton engineering through tunable fluorescent quantum defects in low-dimensional materials, focusing particularly on single-walled carbon nanotubes. This new class of synthetic systems leads us to successfully synthesize more than 30 different types of tunable fluorescent quantum defects, including alkyl/aryl monovalent and divalent defects, from the same semiconducting carbon nanotube structure. By manipulating fluorescent quantum defects, we were able to tune the excitonic states of carbon nanotubes and thus their photoluminescence over 63 meV in the second near-infrared window.

Utilizing electronic effects on excitons and defects, we demonstrate the optical probing of pH and temperature with aminoaryl-functionalized SWCNTs. Switching between the protonated and de-protonated states of the amino moiety significantly modifies the defect state of the covalently functionalized SWCNTs, producing energy shifts as large as 33 meV. This novel defect sensor responds sensitively and selectively to pH changes as small as 0.2 pH units over a wide working window (pH 4.5 to 8.5) that fully covers the pH range of typical biological fluids. The pH sensitive defect photoluminescence also correlates the relative defect PL and pristine PL population with temperature by the van't Hoff equation as a tool for optical probing. Based on these findings, the first bi-functional optical nanoprobe is proposed to offer simultaneous pH and temperature sensing capabilities with a built-in reference.

Last, ultra-bright trion photoluminescence from chirality enriched SWCNTs is created by fluorescence quantum defects. Trion photoluminescence is 10-fold as bright as that from native excitons in unfunctionalized SWCNTs. Defect-bound trions show sensitive response to functional groups and temperature.

## **5.2. Outlook**

We demonstrate the first divalent fluorescent quantum defects with SWCNTs in Chapter 2. Our unique strategy to synthesize divalent defect groups is highly advantageous, but the molecular structures of these divalent defects are still not experimentally established. DFT calculations by our collaborators suggest that the thermodynamically stable structure of divalent aryl defects may assume a broken C-C bond configuration. This may be experimentally verified by using single nanotube Raman spectroscopy, which can differentiate carbene-like structures on the basis of C-C vibrational modes. In addition, the suggested propagative reaction mode with our new chemistry can be experimentally confirmed using single particle fluorescence microscopy. For trion PL, further experiments can be conducted using single particle imaging and lifetime measurement. The defect-bound trion states may be further revealed by transient absorption spectroscopy and upconversion spectroscopy techniques.

Last, we expect that the new exciton engineering method with alkyl/aryl halides can be used as a platform for many potential applications; the versatile functional groups for anchoring of chemical functional groups toward conjugated complexes such as metal-ion nanoprobe, DNA sensors, in vivo bioimaging or drug

delivery for therapeutic study; and the functionalization with aryl halides for nano-device fabrication. Therefore, exciton engineering with tunable fluorescent quantum defects can add an entirely new dimension to the development of carbon nanomaterials and materials engineering.

## Bibliography

1. Koch, S.W., Kira, M., Khitrova, G. & Gibbs, H.M. Semiconductor excitons in new light. *Nat. Mater.* **5**, 523-531 (2006).
2. Spanhel, L., Haase, M., Weller, H. & Henglein, A. *Semiconductor Optics* | Claus F. Klingshirn, Springer (2012)
3. Wannier, G.H. The Structure of Electronic Excitation Levels in Insulating Crystals. *Phys. Rev.* **52**, 191-197 (1937).
4. Frenkel, J. On the Transformation of light into Heat in Solids. I. *Phys. Rev.* **37**, 17-44 (1931).
5. Pope, M., Swenberg, C. E., *Electronic Processes in Organic Crystals and Polymers*. Oxford University Express (1999)
6. Wang, F., Dukovic, G., Brus, L.E. & Heinz, T.F. The Optical Resonances in Carbon Nanotubes Arise from Excitons. *Science* **308**, 838-841 (2005).
7. Yu, P.Y. & Cardona, M. Effect of Quantum Confinement on Electrons and Phonons in Semiconductors in *Fundamentals of Semiconductors: Physics and Materials Properties*, Springer, (2005).
8. Donega, C.d.M. Synthesis and properties of colloidal heteronanocrystals. *Chem. Soc. Rev.* **40**, 1512-1546 (2011).
9. Shen, C., Brozena, A.H. & Wang, Y. Double-walled carbon nanotubes: Challenges and opportunities. *Nanoscale* **3**, 503-518 (2011).
10. Tsyboulski, D.A. *et al.* Do Inner Shells of Double-Walled Carbon Nanotubes Fluoresce? *Nano Lett.* **9**, 3282-3289 (2009).
11. Yang, S., Parks, A.N., Saba, S.A., Ferguson, P.L. & Liu, J. Photoluminescence from Inner Walls in Double-Walled Carbon Nanotubes: Some Do, Some Do Not. *Nano Lett.* **11**, 4405-4410 (2011).
12. Galano, A. Carbon nanotubes: promising agents against free radicals. *Nanoscale* **2**, 373-380 (2010).
13. Bachilo, S.M. Structure-Assigned Optical Spectra of Single-Walled Carbon Nanotubes. *Science* **298**, 2361-2366 (2002).
14. Dresselhaus, M.S., Dresselhaus, G., Saito, R. & Jorio, A. Exciton Photophysics of Carbon Nanotubes. *Annu. Rev. Phys. Chem.* **58**, 719-747 (2007).

15. O'Connell, M.J. Band Gap Fluorescence from Individual Single-Walled Carbon Nanotubes. *Science* **297**, 593-596 (2002).
16. Kane, C.L. & Mele, E.J. Ratio Problem in Single Carbon Nanotube Fluorescence Spectroscopy. *Phys. Rev. Lett.* **90**, 207401 (2003).
17. Mortimer, I.B. & Nicholas, R.J. Role of Bright and Dark Excitons in the Temperature-Dependent Photoluminescence of Carbon Nanotubes. *Phys. Rev. Lett.* **98**, 027404 (2007).
18. Kiowski, O., Arnold, K., Lebedkin, S., Hennrich, F. & Kappes, M.M. Direct Observation of Deep Excitonic States in the Photoluminescence Spectra of Single-Walled Carbon Nanotubes. *Phys. Rev. Lett.* **99**, 237402 (2007).
19. Torrens, O.N., Zheng, M. & Kikkawa, J.M. Energy of K-Momentum Dark Excitons in Carbon Nanotubes by Optical Spectroscopy. *Phys. Rev. Lett.* **101** (2008).
20. Citrin, D.S. Long intrinsic radiative lifetimes of excitons in quantum wires. *Phys. Rev. Lett.* **69**, 3393-3396 (1992).
21. Perebeinos, V., Tersoff, J. & Avouris, P. Effect of Exciton-Phonon Coupling in the Calculated Optical Absorption of Carbon Nanotubes. *Phys. Rev. Lett.* **94**, 027402 (2005).
22. Scholes, G.D. *et al.* Low-Lying Exciton States Determine the Photophysics of Semiconducting Single Wall Carbon Nanotubes. *J. Phys. Chem. C* **111**, 11139-11149 (2007).
23. Mohite, A.D., Santos, T.S., Moodera, J.S. & Alphenaar, B.W. Observation of the triplet exciton in EuS-coated single-walled nanotubes. *Nat. Nanotech.* **4**, 425-429 (2009).
24. Stich, D. *et al.* Triplet-triplet exciton dynamics in single-walled carbon nanotubes. *Nat. Photonics* **8**, 139-144 (2014).
25. Piao, Y. *et al.* Brightening of carbon nanotube photoluminescence through the incorporation of sp<sup>3</sup> defects. *Nat. Chem.* **5**, 840-845 (2013).
26. Nish, A., Hwang, J.-Y., Doig, J. & Nicholas, R.J. Highly selective dispersion of single-walled carbon nanotubes using aromatic polymers. *Nat. Nanotechnol.* **2**, 640-646 (2007).
27. Lefebvre, J., Austing, D.G., Bond, J. & Finnie, P. Photoluminescence Imaging of Suspended Single-Walled Carbon Nanotubes. *Nano Lett.* **6**, 1603-1608 (2006).

28. Carlson, L.J., Maccagnano, S.E., Zheng, M., Silcox, J. & Krauss, T.D. Fluorescence Efficiency of Individual Carbon Nanotubes. *Nano Lett.* **7**, 3698-3703 (2007).
29. Jones, M. *et al.* Analysis of photoluminescence from solubilized single-walled carbon nanotubes. *Phys. Rev. B* **71**, 115426 (2005).
30. Wang, F., Dukovic, G., Brus, L.E. & Heinz, T.F. Time-Resolved Fluorescence of Carbon Nanotubes and Its Implication for Radiative Lifetimes. *Phys. Rev. Lett.* **92**, 177401 (2004).
31. Lee, A.J. *et al.* Bright Fluorescence from Individual Single-Walled Carbon Nanotubes. *Nano Lett.* **11**, 1636-1640 (2011).
32. Nagatsu, K., Chiashi, S., Konabe, S. & Homma, Y. Brightening of Triplet Dark Excitons by Atomic Hydrogen Adsorption in Single-Walled Carbon Nanotubes Observed by Photoluminescence Spectroscopy. *Phys. Rev. Lett.* **105** (2010).
33. Ghosh, S., Bachilo, S.M., Simonette, R.A., Beckingham, K.M. & Weisman, R.B. Oxygen doping modifies near-infrared band gaps in fluorescent single-walled carbon nanotubes. *Science* **330**, 1656-1659 (2010).
34. Zhang, Y. *et al.* Propagative Sidewall Alkylcarboxylation that Induces Red-Shifted Near-IR Photoluminescence in Single-Walled Carbon Nanotubes. *J. Phys. Chem. Lett.* **4**, 826-830 (2013).
35. Ma, X. *et al.* Electronic Structure and Chemical Nature of Oxygen Dopant States in Carbon Nanotubes. *ACS Nano* **8**, 10782-10789 (2014).
36. Deng, S. *et al.* Confined propagation of covalent chemical reactions on single-walled carbon nanotubes. *Nat. Commun.* **2** (2011).
37. Zhang, Y. & Wang, Y. Gold-Substrate-Enhanced Scanning Electron Microscopy of Functionalized Single-Wall Carbon Nanotubes. *J. Phys. Chem. Lett.* **2**, 885-888 (2011).
38. Finkelstein, G., Shtrikman, H. & Bar-Joseph, I. Optical Spectroscopy of a Two-Dimensional Electron Gas near the Metal-Insulator Transition. *Phys. Rev. Lett.* **74**, 976-979 (1995).
39. Warburton, R.J. *et al.* Charged Excitons in Self-Assembled Semiconductor Quantum Dots. *Phys. Rev. Lett.* **79**, 5282-5285 (1997).
40. Solovyev, V.V. & Kukushkin, I.V. Measurement of binding energy of negatively charged excitons in quantum wells. *Phys. Rev. B* **79**, 233306 (2009).

41. Kanemitsu, Y., Okano, M., Nishihara, T. & Yamada, Y. Introducing new optical functions to semiconducting carbon nanotubes. *SPIE Newsroom* (2009)
42. Lampert, M.A. Mobile and Immobile Effective-Mass-Particle Complexes in Nonmetallic Solids. *Phys. Rev. Lett.* **1**, 450-453 (1958).
43. Kheng, K. *et al.* Observation of negatively charged excitons in semiconductor quantum wells. *Phys. Rev. Lett.* **71**, 1752-1755 (1993).
44. Matsunaga, R., Matsuda, K. & Kanemitsu, Y. Observation of Charged Excitons in Hole-Doped Carbon Nanotubes Using Photoluminescence and Absorption Spectroscopy. *Phys. Rev. Lett.* **106** (2011).
45. Santos, S.M. *et al.* All-Optical Trion Generation in Single-Walled Carbon Nanotubes. *Phys. Rev. Lett.* **107** (2011).
46. Park, J.S. *et al.* Observation of Negative and Positive Trions in the Electrochemically Carrier-Doped Single-Walled Carbon Nanotubes. *J. Am. Chem. Soc.* **134**, 14461-14466 (2012).
47. De Greve, K. *et al.* Quantum-dot spin-photon entanglement via frequency downconversion to telecom wavelength. *Nature* **491**, 421-425 (2012).
48. Xia, F., Steiner, M., Lin, Y.-m. & Avouris, P. A microcavity-controlled, current-driven, on-chip nanotube emitter at infrared wavelengths. *Nat. Nanotechnol.* **3**, 609-613 (2008).
49. Song, J.Y., Stingelin, N., Drew, A.J., Kreouzis, T. & Gillin, W.P. Effect of excited states and applied magnetic fields on the measured hole mobility in an organic semiconductor. *Phys. Rev. B* **82**, 085205 (2010).
50. Tayo, B.O. & Rotkin, S.V. Charge impurity as a localization center for singlet excitons in single-wall nanotubes. *Phys. Rev. B* **86**, 125431 (2012).
51. Wen, X. *et al.* Defect trapping states and charge carrier recombination in organic-inorganic halide perovskites. *J. Mater. Chem. C* **4**, 793-800 (2016).
52. Mouri, S., Miyauchi, Y., Iwamura, M. & Matsuda, K. Temperature dependence of photoluminescence spectra in hole-doped single-walled carbon nanotubes: Implications of trion localization. *Phys. Rev. B* **87**, 045408 (2013).
53. Brinkmann, D. *et al.* Trion and exciton dephasing measurements in modulation-doped quantum wells: A probe for trion and carrier localization. *Phys. Rev. B* **60**, 4474-4477 (1999).

54. Cox, M., Janssen, P., Zhu, F. & Koopmans, B. Traps and trions as origin of magnetoresistance in organic semiconductors. *Phys. Rev. B* **88**, 035202 (2013).
55. Nishihara, T., Yamada, Y., Okano, M. & Kanemitsu, Y. Trion formation and recombination dynamics in hole-doped single-walled carbon nanotubes. *Appl. Phys. Lett.* **103**, 023101 (2013).
56. Jakubka, F., Grimm, S.B., Zakharko, Y., Gannott, F. & Zaumseil, J. Trion Electroluminescence from Semiconducting Carbon Nanotubes. *ACS Nano* **8**, 8477-8486 (2014).
57. Brozena, A.H., Leeds, J.D., Zhang, Y., Fourkas, J.T. & Wang, Y. Controlled defects in semiconducting carbon nanotubes promote efficient generation and luminescence of trions. *ACS Nano* **8**, 4239-4247 (2014).
58. Watanabe, K. & Asano, K. Trions in semiconducting single-walled carbon nanotubes. *Phys. Rev. B* **85**, 035416 (2012).
59. Tu, X., Manohar, S., Jagota, A. & Zheng, M. DNA sequence motifs for structure-specific recognition and separation of carbon nanotubes. *Nature* **460**, 250-253 (2009).
60. Liu, H., Nishide, D., Tanaka, T. & Kataura, H. Large-scale single-chirality separation of single-wall carbon nanotubes by simple gel chromatography. *Nat. Commun.* **2** (2011).
61. Ao, G., Khripin, C.Y. & Zheng, M. DNA-Controlled Partition of Carbon Nanotubes in Polymer Aqueous Two-Phase Systems. *J. Am. Chem. Soc.* **136**, 10383-10392 (2014).
62. Khripin, C.Y., Fagan, J.A. & Zheng, M. Spontaneous Partition of Carbon Nanotubes in Polymer-Modified Aqueous Phases. *J. Am. Chem. Soc.* **135**, 6822-6825 (2013).
63. Hong, G. *et al.* Multifunctional in vivo vascular imaging using near-infrared II fluorescence. *Nat. Med.* **18**, 1841-1846 (2012).
64. Chan, W.C.W. & Nie, S. Quantum dot bioconjugates for ultrasensitive nonisotopic detection. *Science* **281**, 2016-2018 (1998).
65. Heller, D.A. *et al.* Optical Detection of DNA Conformational Polymorphism on Single-Walled Carbon Nanotubes. *Science* **311**, 508-511 (2006).
66. Kamat, P.V. Quantum dot solar cells. Semiconductor nanocrystals as light harvesters. *J. Phys. Chem. C* **112**, 18737-18753 (2008).

67. Shirasaki, Y., Supran, G.J., Bawendi, M.G. & Bulović, V. Emergence of colloidal quantum-dot light-emitting technologies. *Nat. Photonics* **7**, 13-23 (2013).
68. Rossetti, R., Nakahara, S. & Brus, L.E. Quantum size effects in the redox potentials, resonance Raman spectra, and electronic spectra of cadmium sulfide crystallites in aqueous solution. *J. Chem. Phys.* **79**, 1086-1088 (1983).
69. Alivisatos, A.P. Semiconductor clusters, nanocrystals, and quantum dots. *Science* **271**, 933-937 (1996).
70. Yin, Y. & Alivisatos, A.P. Colloidal nanocrystal synthesis and the organic-inorganic interface. *Nature* **437**, 664-670 (2005).
71. Gruber, A. *et al.* Scanning confocal optical microscopy and magnetic resonance on single defect centers. *Science* **276**, 2012-2014 (1997).
72. Erwin, S.C. *et al.* Doping semiconductor nanocrystals. *Nature* **436**, 91-94 (2005).
73. Akizuki, N., Aota, S., Mouri, S., Matsuda, K. & Miyauchi, Y. Efficient near-infrared up-conversion photoluminescence in carbon nanotubes. *Nat. Commun* **6** (2015).
74. Zheng, M. & Diner, B.A. Solution Redox Chemistry of Carbon Nanotubes. *J. Am. Chem. Soc.* **126**, 15490-15494 (2004).
75. Artem, R.C., Vladimir, I.G. & Rafael, A.C. The problem of the quantitative evaluation of the inductive effect: correlation analysis. *Russ. Chem. Rev.* **65**, 641 (1996).
76. Zhang, C.-P., Chen, Q.-Y., Guo, Y., Xiao, J.-C. & Gu, Y.-C. Progress in fluoroalkylation of organic compounds via sulfonatodehalogenation initiation system. *Chem Soc Rev* **41**, 4536-4559 (2012).
77. Xiao, Z., Hu, H., Ma, J., Chen, Q. & Guo, Y. Radical Addition of Perfluoroalkyl Iodides to Alkenes and Alkynes Initiated by Sodium Dithionite in an Aqueous Solution in the Presence of a Novel Fluorosurfactant. *Chin. J. Chem.* **31**, 939-944 (2013).
78. Capaz, R.B., Spataru, C.D., Ismail-Beigi, S. & Louie, S.G. Diameter and chirality dependence of exciton properties in carbon nanotubes. *Phys. Rev. B* **74**, 121401 (2006).
79. Dresselhaus, M.S., Dresselhaus, G. & Jorio, A. Raman Spectroscopy of Carbon Nanotubes in 1997 and 2007. *J. Phys. Chem. C* **111**, 17887-17893 (2007).

80. Hansch, C., Leo, A. & Taft, R.W. A survey of Hammett substituent constants and resonance and field parameters. *Chem. Rev.* **91**, 165-195 (1991).
81. Kropp, P.J. Photobehavior of alkyl halides in solution: radical, carbocation, and carbene intermediates. *Acc. Chem. Res.* **17**, 131-137 (1984).
82. Li, J., Jia, G., Zhang, Y. & Chen, Y. Bond-Curvature Effect of Sidewall [2+1] Cycloadditions of Single-Walled Carbon Nanotubes: A New Criterion To the Adduct Structures. *Chem. Mater.* **18**, 3579-3584 (2006).
83. Zhang, K. & Zhang, Q. Raman Signatures of Broken C–C Bonds in Single-Walled Carbon Nanotubes upon [2 + 1] Cycloaddition. *J. Phys. Chem. C* **119**, 18753-18761 (2015).
84. Sanchez-Valencia, J.R. *et al.* Controlled synthesis of single-chirality carbon nanotubes. *Nature* **512**, 61-64 (2014).
85. Lagadic-Gossmann, D., Huc, L. & Lecureur, V. Alterations of intracellular pH homeostasis in apoptosis: origins and roles. *Cell. Death. Differ.* **11**, 953-961 (2004).
86. Webb, B.A., Chimenti, M., Jacobson, M.P. & Barber, D.L. Dysregulated pH: a perfect storm for cancer progression. *Nat. Rev. Cancer.* **11**, 671-677 (2011).
87. Wijesinghe, D., Arachchige, M.C.M., Lu, A., Reshetnyak, Y.K. & Andreev, O.A. pH dependent transfer of nano-pores into membrane of cancer cells to induce apoptosis. *Sci. Rep.* **3**, 3560 (2013).
88. Ma, X. *et al.* Ultra-pH-Sensitive Nanoprobe Library with Broad pH Tunability and Fluorescence Emissions. *J. Am. Chem. Soc.* **131**, 11085-11092 (2014).
89. Korzeniowska, B. *et al.* Intracellular pH-Sensing Using Core/Shell Silica Nanoparticles. *J. Biomed. Nanotech.* **10**, 1336-1345 (2014).
90. Brites, C.D.S. *et al.* Thermometry at the nanoscale. *Nanoscale* **4**, 4799-4829 (2012).
91. Ozawa, T., Yoshimura, H. & Kim, S.B. Advances in Fluorescence and Bioluminescence Imaging. *Anal. Chem.* **85**, 590-609 (2013).
92. Lee, J. & Kotov, N.A. Thermometer design at the nanoscale. *Nano Today* **2**, 48-51 (2007).
93. Tang, R., Lee, H. & Achilefu, S. Induction of pH Sensitivity on the Fluorescence Lifetime of Quantum Dots by NIR Fluorescent Dyes. *J. Am. Chem. Soc.* **134**, 4545-4548 (2012).

94. Aigner, D., Borisov, S.M., Petritsch, P. & Klimant, I. Novel near infra-red fluorescent pH sensors based on 1-aminoperylene bisimides covalently grafted onto poly(acryloylmorpholine). *Chem. Commun.* **49**, 2139-2141 (2013).
95. Huang, J. *et al.* Covalently Functionalized Double-Walled Carbon Nanotubes Combine High Sensitivity and Selectivity in the Electrical Detection of Small Molecules. *J. Am. Chem. Soc.* **135**, 2306-2312 (2013).
96. Kam, N.W.S., O'Connell, M., Wisdom, J.A. & Dai, H. Carbon nanotubes as multifunctional biological transporters and near-infrared agents for selective cancer cell destruction. *Proc. Natl. Acad. Sci.* **102**, 11600-11605 (2005).
97. Berger, S. *et al.* Temperature Dependence of Exciton Recombination in Semiconducting Single-Wall Carbon Nanotubes. *Nano Lett.* **7**, 398-402 (2007).
98. Diao, S. *et al.* Chirality Enriched (12,1) and (11,3) Single-Walled Carbon Nanotubes for Biological Imaging. *J. Am. Chem. Soc.* **134**, 16971-16974 (2012).
99. Singh, R.P., Jain, S. & Ramarao, P. Surfactant-assisted dispersion of carbon nanotubes: mechanism of stabilization and biocompatibility of the surfactant. *J. Nanopart. Res.* **15**, 1-19 (2013).
100. Iverson, N.M. *et al.* In vivo biosensing via tissue-localizable near-infrared-fluorescent single-walled carbon nanotubes. *Nat. Nanotechnol.* **8**, 873-880 (2013).
101. Duque, J.G. *et al.* Stable Luminescence from Individual Carbon Nanotubes in Acidic, Basic, and Biological Environments. *J. Am. Chem. Soc.* **130**, 2626-2633 (2008).
102. Miyauchi, Y. *et al.* Dependence of exciton transition energy of single-walled carbon nanotubes on surrounding dielectric materials. *Chem. Phys. Lett.* **442**, 394-399 (2007).
103. Silvera-Batista, C.A., Scott, D.C., McLeod, S.M. & Ziegler, K.J. A Mechanistic Study of the Selective Retention of SDS-Suspended Single-Wall Carbon Nanotubes on Agarose Gels. *J. Phys. Chem. C* **115**, 9361-9369 (2011).
104. Niyogi, S. *et al.* Selective Aggregation of Single-Walled Carbon Nanotubes via Salt Addition. *J. Am. Chem. Soc.* **129**, 1898-1899 (2007).

105. Niyogi, S., Densmore, C.G. & Doorn, S.K. Electrolyte Tuning of Surfactant Interfacial Behavior for Enhanced Density-Based Separations of Single-Walled Carbon Nanotubes. *J. Am. Chem. Soc.* **131**, 1144-1153 (2009).
106. Duque, J.G., Densmore, C.G. & Doorn, S.K. Saturation of Surfactant Structure at the Single-Walled Carbon Nanotube Surface. *J. Am. Chem. Soc.* **132**, 16165-16175 (2010).
107. Baker, D.R. & Kamat, P.V. Tuning the Emission of CdSe Quantum Dots by Controlled Trap Enhancement. *Langmuir* **26**, 11272-11276 (2010).
108. Park, Y.-S., Bae, W.K., Pietryga, J.M. & Klimov, V.I. Auger Recombination of Biexcitons and Negative and Positive Trions in Individual Quantum Dots. *ACS Nano* **8**, 7288-7296 (2014).
109. Rønnow, T.F., Pedersen, T.G. & Cornean, H.D. Correlation and dimensional effects of trions in carbon nanotubes. *Phys. Rev. B* **81**, 205446 (2010).
110. Yuma, B. *et al.* Biexciton, single carrier, and trion generation dynamics in single-walled carbon nanotubes. *Phys. Rev. B* **87**, 205412 (2013).